

Fall 11-15-2017

# The Inverse Kinetics Method and Its Application to the Annular Core Research Reactor

Thomas A. Ball

Follow this and additional works at: [https://digitalrepository.unm.edu/ne\\_etds](https://digitalrepository.unm.edu/ne_etds)



Part of the [Nuclear Engineering Commons](#)

---

## Recommended Citation

Ball, Thomas A.. "The Inverse Kinetics Method and Its Application to the Annular Core Research Reactor." (2017).  
[https://digitalrepository.unm.edu/ne\\_etds/66](https://digitalrepository.unm.edu/ne_etds/66)

This Thesis is brought to you for free and open access by the Engineering ETDs at UNM Digital Repository. It has been accepted for inclusion in Nuclear Engineering ETDs by an authorized administrator of UNM Digital Repository. For more information, please contact [disc@unm.edu](mailto:disc@unm.edu).

Thomas Ball

*Candidate*

Nuclear Engineering

*Department*

This thesis is approved, and it is acceptable in quality and form for publication:

*Approved by the Thesis Committee:*

Dr. Robert Busch, Chairperson

Dr. Adam Hecht

Dr. Cassiano de Oliveira

Dr. Edward Parma

**The Inverse Kinetics Method and Its Application to the Annular Core  
Research Reactor**

by

Thomas Ball

B.S., Nuclear Engineering, University of New Mexico, 2016

THESIS

*Submitted in partial fulfillment of the  
requirements for the degree of*

Master of Science

Nuclear Engineering

The University of New Mexico  
Albuquerque, New Mexico

December, 2017

## **Acknowledgements**

I would like to greatly thank my mentor, Ed Parma, for the opportunity to work on this project. I am also thankful for the large amounts time, expert advice, and support he has provided me. I would like to thank my advisor, Bob Busch, for the resources he provided for this project and the vast amounts of knowledge he has shared with me throughout my academic career. I would also like to thank my professors and committee members, Adam Hecht and Cassiano de Oliveira, for their guidance and support during my journey through college. In addition, I am very grateful for the assistance provided by Elliott Pelfrey, Billy Martin, and Darren Talley in various areas of this project.

# **The Inverse Kinetics Method and Its Application to the Annular Core Research Reactor**

by

Thomas Ball

B.S., Nuclear Engineering, University of New Mexico, 2016

M.S., Nuclear Engineering, University of New Mexico, 2017

## **Abstract**

The inverse kinetics method, is a method to calculate a reactor's reactivity profile from its power profile. In this thesis, the reactivity profile corresponding to pulse operations of the Annular Core Research Reactor (ACRR) was sought. Of specific interest was the shutdown reactivity of the reactor following the pulse. This required accounting for delayed beryllium photoneutrons that are present in the ACRR in addition to U-235 delayed neutron precursors. The power profiles of the pulses were experimentally measured using a diamond photoconductive detector (PCD). Using the inverse kinetics equation, a computer code was written to numerically calculate the reactivity corresponding to the PCD signal. It was found that the PCD's signal was only proportional to the reactor power before and during a pulse. Following a pulse, the PCD lost this proportionality because its response became dominated by fission product and activation gamma rays. Attempts were made to subtract the unwanted gamma ray contribution from the PCD signal. This allowed the reactivity to be roughly determined for tens of seconds following the pulse before the signal strength became too low.

The reactivity before and during a pulse could accurately be calculated without the need to correct the PCD signal. This thesis also provides a detailed derivation of the point kinetics equations and inverse kinetics equation, and explores the behavior of the inverse kinetics equation in detail.

## Table of Contents

List of Figures .....	viii
List of Tables .....	xi
1. Introduction .....	1
1.1 ACRR .....	2
2. Nuclear Reactor Kinetics .....	6
2.1 Delayed Neutron Precursors.....	6
2.2 Reactivity .....	11
2.3 Derivation of the Point Kinetics Equations.....	14
3. The Inverse Kinetics Method.....	23
3.1 Derivation of the Inverse Kinetics Equation .....	23
3.2 Understanding the Inverse Kinetics Equation Solution .....	28
3.3 External Source Considerations .....	39
4. Numerical Solutions to the Inverse Kinetics Equation .....	41
4.1 Numerical Solution .....	41
4.2 Code Validation.....	46
4.2.1 Point Kinetics Code.....	47
4.2.2 Razorback Comparison .....	49
5. Experimental Data Collection and Preparation.....	52
5.1 Detectors Used .....	53
5.1.1 Photoconductive Detector (PCD) .....	53
5.1.2 Self-Powered Neutron Detector (SPND) .....	56
5.2 Experimental Data Preparation .....	58
5.2.1 Smoothing .....	58
5.2.2 Linearizing.....	60
5.2.3 Merging .....	61
5.3 Activation and Fission Product Gamma Ray Subtraction.....	63
5.3.1 U-235 Fission Product and Activated Aluminum Subtraction.....	66
5.3.2 Razorback and PCD Difference .....	72
6. Results .....	82
6.1 Source Identification and Subtraction .....	82
6.1.1 56 MJ Free-Field Pulse.....	83
6.1.2 140 MJ Free-Field Pulse.....	85
6.1.3 127 MJ Lead-Boron Pulse.....	87
6.1.4 270 MJ Lead-Boron Pulse.....	89
6.1.5 Comparison of Identified Half-Lives .....	91

7. Conclusion .....	93
7.1 Future Work .....	94
Appendix A – Inverse Kinetics Code Flow Chart for Fortran 95 .....	96
References .....	97



## List of Figures

Figure 1.1: The view inside of the ACRR tank during a pulse with FREC-II in the decoupled position.....	3
Figure 1.2: Diagram showing the rods that can be manipulated in the ACRR [Knief, 2015]..	5
Figure 3.1: Simulated power profile and corresponding reactivity profile, generated using the point kinetics equations. This example will be used to study the inverse kinetics equation. The right plot is zoomed in, in time, to better show the pulse. ....	30
Figure 3.2: The coefficient of the inverse kinetics equation at the time of the pulse. ....	30
Figure 3.3: Prompt term and the product of the prompt term and the coefficient. The data point shows the small effect that the coefficient has at its point of largest deviation from unity....	32
Figure 3.4: The derivative of the power profile, normalized to $P(t)$ .....	32
Figure 3.5: Delayed neutron kernel generated using the ACRR's 17 delayed neutron groups. ....	33
Figure 3.6: Integral values of the delayed term. These values are proportional to the delayed neutron emission rate and the precursor concentration in the reactor. ....	35
Figure 3.7: The delayed term of the inverse kinetics equation and the product of it with the coefficient. The data point shows the small effect that the coefficient has at its point of largest deviation from unity.....	35
Figure 3.8: The left plot shows the errors that occur if the initial condition isn't accounted for and the right plot shows the correct reactivity obtained by accounting for the initial condition. ....	37
Figure 3.9: Plot showing the product of the prompt term with the coefficient, the product of the delayed term with the coefficient, and the calculated reactivity which is the sum of those two profiles. ....	38
Figure 3.10: Plots showing the reactivity calculated using the inverse kinetics equation, compared to the reactivity inputted into the point kinetics equations. The plot on the right is zoomed in, in time.....	38
Figure 3.11: ACRR reactivity profile calculated using experimental data and not accounting for a source. Following the pulse, the reactivity should drop to about $-\$10$ and remain there; however, it was found to only drop to a few dollars negative and then approached zero because of detection of fission product and activation gamma rays. ....	40
Figure 4.1: Example showing how the delayed neutron kernel and the power profile would overlap when evaluating the convolution integral for $t = 1$ . A coarse time step is shown so that it can be seen that the delayed neutron kernel must be evaluated at times corresponding to the power data points previous to $t$ . ....	43
Figure 4.2: Plot showing the reactivity calculated using the inverse kinetics equation compared to the true reactivity. As can be seen, the actual reactivity is closely obtained; however, the inverse kinetics reactivity begins to deviate from the true reactivity as the negative reactivity is linearly inserted. A time step of $10\mu s$ was used. ....	48

Figure 4.3: Using a power profile from Razorback, good agreement was found between the calculated reactivity and the Razorback reactivity. ....	50
Figure 5.1: Cutaway of a PCD showing the 1 x 1 x 1 mm diamond semiconductor between the two gold ohmic contacts. ....	54
Figure 5.2: Comparison of a PCD and SPND signal from an ACRR pulse. The SPND signal quickly goes flat following the pulse because of its low sensitivity.....	57
Figure 5.3: Plots showing the raw log-amp PCD signals, before and after smoothing. The signals are inverted as a byproduct of the log-amp.....	59
Figure 5.4: The short and long linear PCD signals, shown with linear and logarithmic y-axis scales. ....	61
Figure 5.5: Plot showing the overlap of the short and the long PCD signals. The smaller sampling interval of the short signal provides greater resolution of the pulse. ....	62
Figure 5.6: Processed PCD profile from a 56 MJ FF pulse, ready for input into the inverse kinetics code.....	63
Figure 5.7: Reactivity profile corresponding to the PCD power profile in Figure 5.6, calculated using the inverse kinetics code. The reactivity is correct before and during the pulse, but following the pulse it does not drop to and remain at the expected value of about - $\beta$ . ....	64
Figure 5.8: Delayed fission product and 6061-T6 aluminum activation, gamma decay curves. The aluminum decay is slower because of the longer-lived impurities, such as Mn-56. The relative contribution from these two sources to the PCD signal, is not known. ....	68
Figure 5.9: Experimentally measured PCD power profile compared to a corresponding computer-generated Razorback power profile. As expected the signals closely match during the pulse but the PCD diverges following the pulse. ....	70
Figure 5.10: Three different combinations of the fission product and activated aluminum decay curves. Assuming the delayed gammas were due 100% to the fission products gave the best “corrected” PCD profile.....	71
Figure 5.11: By subtracting off fission product gammas the calculated reactivity agreed better with Razorback; however, other sources still need to be accounted for. ....	72
Figure 5.12: Plot showing the difference between the PCD and Razorback profiles during the tail of the 56 MJ FF pulse. ....	74
Figure 5.13: The seven linear regions that were identified using the difference profile from Figure 5.12. For each plot, the source contributions from all longer-lived sources were subtracted from the difference profile.....	76
Figure 5.14: The decay curve created from the seven identified sources, compared with the activated aluminum and fission product decay curves. ....	77
Figure 5.15: The results of convoluting the decay curve, created with the seven identified sources, with the original PCD signal. The corrected profile gives better agreement with Razorback than was achieved with the fission product and activated aluminum decay curves. ....	78

Figure 5.16: Assuming that the delayed gammas are only responsible for 97.5% of the signal at 1800 s rather than 99.78%. This reduces the noise in the “corrected” profile, but also gives it poorer agreement with Razorback. ....	79
Figure 5.17: The reactivity profile shown here is the best that could be achieved using the methods described in this chapter. It most closely gives the expected shutdown reactivity. .	80
Figure 5.18: By assuming the delayed gammas contribute less than 99.78%, the reactivity doesn’t drop quite as low as expected, but the noise is lower and it is still better than what was achieved with the fission product and activated aluminum decay curves. ....	80
Figure 6.1: The results of correcting the 56 MJ FF PCD signal using the seven identified sources, and the reactivity calculated using the inverse kinetics code. ....	84
Figure 6.2: The results of correcting the 140 MJ FF PCD signal using the five identified sources, and the reactivity calculated using the inverse kinetics code. ....	86
Figure 6.3: The results of correcting the 127 MJ LB44 PCD signal using the six identified sources, and the reactivity calculated using the inverse kinetics code. ....	88
Figure 6.4: The results of correcting the 270 MJ LB44 PCD signal using the seven identified sources, and the reactivity calculated using the inverse kinetics code. ....	90

## List of Tables

Table 2.1: Eight-group Campbell and Spriggs delayed neutron data for thermal fission of U-235. [Campbell, Spriggs, & Vladimir, 2002].....	7
Table 2.2: Nine-group delayed beryllium photoneutron data from Keepin for thermal fission of U-235 [Keepin, 1965].....	9
Table 2.3: Important reactivity values in dollars. ....	13
Table 5.1: Average ionizing dose deposited in carbon (diamond) per fission, in the central cavity of the ACRR. [Parma et al., 2015] and [Parma et al., 2013].....	55
Table 5.2: The data used to generate the 6061-T6 Al activation decay curve. The element weight percents were obtained from the ACRR MCNP model [Parma et al., 2015]. The decay and cross-section data was obtained from the National Nuclear Data Center (NNDC) [2017]..	67
Table 5.3: The seven identified sources from the 1800 s long difference profile from the 56 MJ free-field pulse. ....	75
Table 6.1: The identified sources responsible for the excess contribution to the PCD signal during the tail of the pulse. The same number of sources were not identified for each pulse, which needs to be considered when comparing relative abundances. ....	92

## 1. Introduction

The purpose of this thesis was to explore the application of the inverse kinetics method to the Annular Core Research Reactor (ACRR). This was done in an effort to calculate the reactivity profile during a pulse and multiple hours afterwards, using experimentally gathered data. The inverse kinetics method is the method of “inverting” the point reactor kinetics equations such that they are solved to give the reactivity at a given time assuming the reactor power is known for all previous times. This is of interest for reactor diagnostics because power is something that can be experimentally measured, and through the use of the inverse kinetics equation this can be converted to reactivity, which is not an easily measured quantity.

To measure the power profile needed to calculate the reactivity, radiation detectors are placed in the core of the ACRR. These detectors need to be able to capture the large changes in signal strength experienced between the peak and the tail of the pulse. Capturing this wide range of signal strengths requires special consideration, which will be discussed in Chapter 5. Another challenge is encountered when the power of the reactor decreases after a pulse. As this happens, activation and fission product gamma rays begin to contribute a non-negligible amount to the detector signal. This causes the signal to lose its proportionality to the true power profile. This requires that the unwanted contribution be identified and subtracted from the experimental data before it can be used to calculate the reactivity. When using the inverse kinetics method to calculate the shutdown reactivity long after a pulse, it is also important to account for all delayed neutron precursors and for any “external” neutron sources. In the case of the ACRR, delayed photoneutron precursors, due to the beryllium in the fuel, need to be accounted for in addition to the typical U-235 delayed neutron precursors. If an “external” neutron source is present and it is not accounted for when the reactor is at low powers, it can

cause the calculated reactivity to approach zero (critical), even if the reactor is very subcritical. In the case of the ACRR, the magnitude of the contribution from activation and fission product gamma rays and the effective neutron source strength were not known, which made it difficult to calculate the reactivity when the power signal was low. It was found that the presence of an “external” neutron source could be neglected; however, it is necessary to account for the contribution from activation and fission product gamma rays.

Reactivity is a very useful quantity for understanding and operating a nuclear reactor. It gives a quantitative value to the amount of deviation of a reactor core from criticality. Obtaining the reactivity profile corresponding to a pulse provides information regarding the physical changes that happen in the reactor core, such as the movement of control rods, reactivity feedback effects, and much more. By obtaining these profiles using experimental data, the behavior of the reactor during specific operations can be known. These reactivity profiles could potentially be used check the accuracy of reactivity calculations from computer simulations. Studying the behavior of the experimentally calculated reactivity profiles also gives insight into how accurately a detector captures the reactor’s power profile, and hence the time dependent neutron population. As will be seen, the largest challenge faced during this project was obtaining a detector signal that was proportional to the reactor power following a pulse.

## **1.1 ACRR**

The Annular Core Research Reactor (ACRR) at Sandia National Laboratories gets its name from the annular arrangement of the fuel rods in its core. The core is located in an open pool filled with water which acts as a neutron moderator and radiation shield and allows the core to cool by natural convection. The fuel rods circle an approximately 9” internal diameter

dry irradiation cavity where a variety of different experiments can be exposed to a high neutron fluence. This neutron fluence can be achieved by operating the ACRR in either a pulse or steady state mode. Figure 1.1 shows the ACRR during a pulse with the associated blue Cherenkov radiation. In the figure, the fueled ring external cavity-II (FREC-II) and the 20" dry external cavity can also be seen in the decoupled position. FREC-II is a subcritical multiplier that can be moved towards the ACRR core so that they become coupled. FREC-II uses uranium/zirconium-hydride (U-ZrH) TRIGA fuel [Parma et al., 2015] and provides a larger test volume than the ACRR central cavity. All the data used in this project is from pulses with FREC-II in the decoupled position.

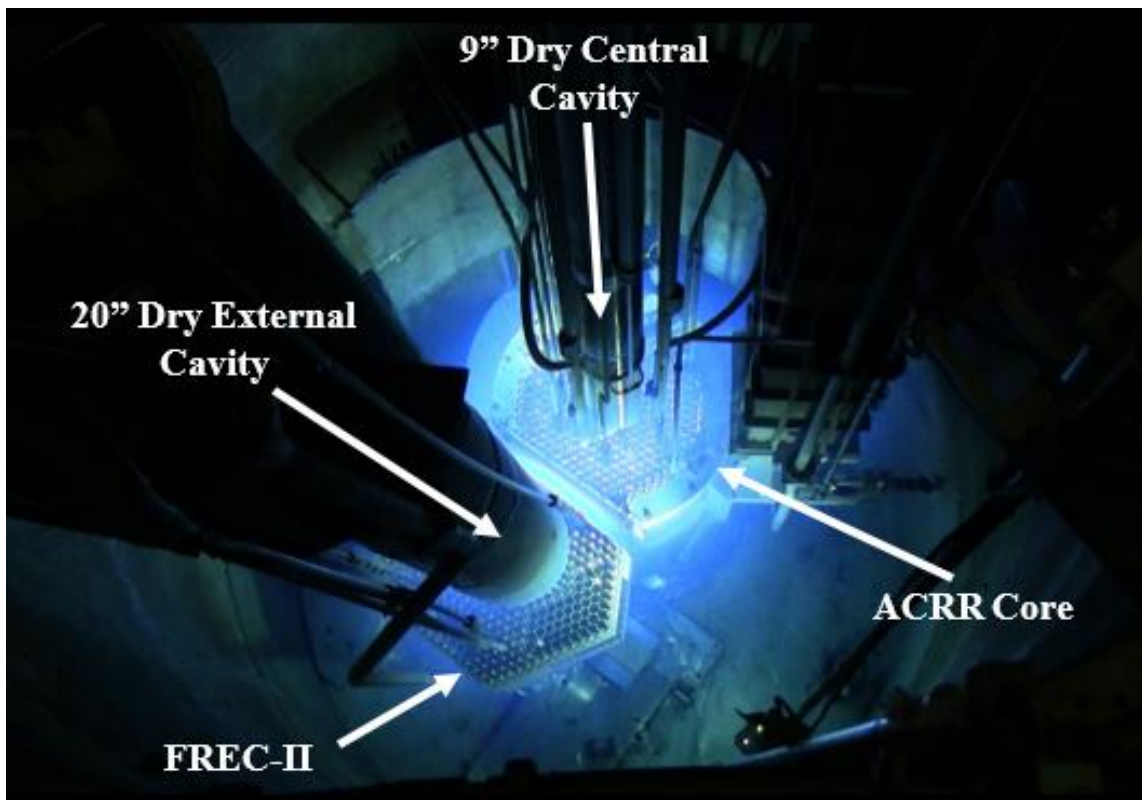


Figure 1.1: The view inside of the ACRR tank during a pulse with FREC-II in the decoupled position.

The ACRR is purposely under-moderated, which gives the neutron spectrum of the core and central cavity a large epithermal component. Through the use of “buckets” composed of different materials, the radiation environment in the central cavity can be tailored to some degree to meet the needs of an experiment. For example, a bucket composed of a moderator such as polyethylene, could be placed in the central cavity to produce a softer neutron spectrum, or a bucket containing a thermal neutron absorber such as boron, could be used to create a harder spectrum. In addition, these buckets can also contain a high atomic number materials such as lead, which reduce the gamma radiation in the central cavity. For this thesis, data was gathered for pulses with no bucket in the central cavity (free-field) and with a lead-boron bucket in the central cavity. The lead-boron bucket is referred to as LB44 (it is 44 inches tall), and it is designed to filter out gamma rays and thermal neutrons from the internal experimental volume, producing an epithermal neutron environment with a high neutron-to-gamma ray ratio [Parma et al., 2013].

A unique and important design characteristic of the ACRR is its fuel. The fuel is a homogeneous mix of uranium enriched to 35 weight percent U-235, with 21.5 weight percent uranium oxide ( $\text{UO}_2$ ) and 78.5 weight percent beryllium oxide ( $\text{BeO}$ ) [Parma et al., 2015]. The pellets are segmented to allow the ceramic fuel to tolerate the radial and tangential stresses experienced during a pulse. The beryllium oxide in the fuel increases its heat capacity and aids in allowing the ACRR to achieve large pulses up to 35,000  $\text{MW}_{\text{th}}$ . The beryllium in the fuel also has the effect of producing neutrons through  $(\gamma, n)$ ,  $(n, 2n)$ , and  $(\alpha, n)$  reactions. It will be shown in Chapter 2 that due to time dependent behavior, special consideration of the photoneutrons is needed for calculating the late time reactivity of the ACRR.



To operate the ACRR, there are 11 movable rods in the core that can be adjusted to produce a desired power profile. There are six control rods, two safety rods, and three transient rods. As can be seen in Figure 1.2, the control rods and safety rods consist of boron carbide ( $B_4C$ ) absorbers followed by fuel, and the transient rods are boron carbide followed by void. To pulse the ACRR, the safety rods are fully withdrawn and the control rods are adjusted to bring the reactor to a steady state power level. Then from a specified location, the transient rods are removed from the core using pressurized nitrogen, which results in the insertion of a large amount of positive reactivity. The transient rods are then held in the full out position for a specified time, after which all 11 of the movable rods are dropped into the core to fully shut the reactor down. Typical pulses at the ACRR have reactivity insertions of \$1 to \$3 and yields up to 300MJ.

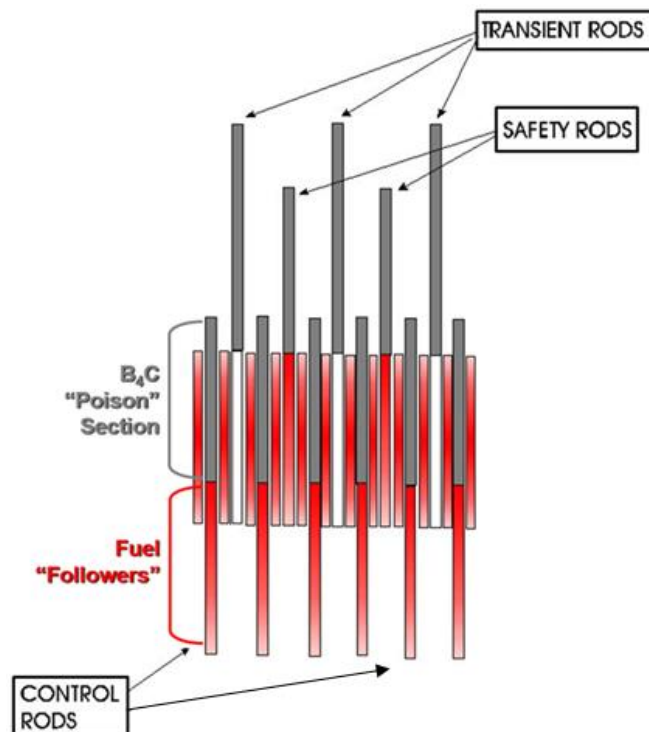


Figure 1.2: Diagram showing the rods that can be manipulated in the ACRR [Knief, 2015].

## **2. Nuclear Reactor Kinetics**

Nuclear reactor kinetics is concerned with predicting the time behavior of a reactor's power due to reactivity/multiplication changes in its core. Exploring this topic will provide some background information relevant to the derivation of the inverse kinetics equation and its application to the ACRR. Delayed neutrons and the precursor data used for this project will be discussed in Section 2.1. A description of reactivity will then be given in Section 2.2. In Section 2.3 the point reactor kinetics equations will be derived, which will be used to derive the inverse kinetics equation in Chapter 3.

### **2.1 Delayed Neutron Precursors**

As a result of the fission of a fissile isotope, such as uranium-235, an average number of neutrons (typically 2 to 3) will be released. Of these neutrons, some will be released promptly and some will have a delayed release. The delayed neutrons usually account for less than 1% of all neutrons resulting from fission in a nuclear reactor; however, they are essential for the safe operation of a reactor, and they dictate how quickly the neutron population will decrease after the reactor is shut down. In most reactors, the only source of delayed neutrons is from fission fragments that occasionally beta decay to a daughter product in a highly excited state, which then quickly decays by neutron emission to a stable state. These fission fragments are known as delayed neutron precursors, and they are grouped according to similarities in their half-lives. Table 2.1 shows the Campbell and Spriggs [2002] eight-group delayed neutron data for thermal fission of U-235. This data is derived from the six-group Keepin [1957] data while preserving its important characteristics, but takes advantage of improved modern understanding of delayed neutron precursors. The Campbell and Spriggs data uses standardized half-life values that are independent of isotope or neutron energy, which

simplifies kinetics calculations involving mixed fuel systems and increases the ease of comparison of delayed neutron data. This standardization means only the relative group abundances change from isotope to isotope.

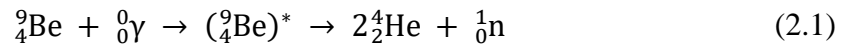
Table 2.1: Eight-group Campbell and Spriggs delayed neutron data for thermal fission of U-235. [Campbell, Spriggs, & Vladimir, 2002]

Group Number	Half-Life	$\lambda_i$ (s <sup>-1</sup> )	$\alpha_i$	$\beta_i$ for ACRR
1	55.6 s	1.25E-2	0.033	0.23859E-3
2	24.5 s	2.83E-2	0.154	1.11342E-3
3	16.3 s	4.25E-2	0.091	0.65793E-3
4	5.21 s	1.33E-1	0.197	1.42431E-3
5	2.37 s	2.92E-1	0.331	2.39313E-3
6	1.04 s	6.66E-1	0.090	0.6507E-3
7	0.424 s	1.63E-0	0.081	0.58563E-3
8	0.195 s	3.55E-0	0.023	0.16629E-3
total	--	--	1.000	7.230E-3

In Table 2.1,  $\lambda_i$  is the decay constant of the  $i^{\text{th}}$  precursor group,  $\alpha_i$  is the relative group abundance, and  $\beta_i$  is the delayed neutron fraction per fission of the  $i^{\text{th}}$  precursor group. The  $\alpha_i$  values are specific to thermal fission of U-235; however, the  $\beta_i$  values are specific to the reactor under consideration. The  $\beta_i$  values in the table were calculated using the total effective delayed neutron fraction,  $\beta_{\text{eff}}$ , for the ACRR. By multiplying the  $\alpha_i$  values by  $\beta_{\text{eff}}$  the corresponding  $\beta_i$  values can be determined. The historically used  $\beta_{\text{eff}}$  valued for the ACRR is 0.0073 +/- 0.0003 [Pickard & Odom, 1982]. To check this value a MCNP model of the ACRR (as described in [Parma et al., 2015]) was run by Ed Parma using 10 million particles and 2000 cycles, and through the use of the kopts card, a  $\beta_{\text{eff}}$  value of 0.00723 +/- 0.00001 was obtained. The

effective delayed neutron fraction accounts for the variation in effectiveness that the delayed neutrons have in different reactors due to their lower average energy than prompt neutrons. Also, through MCNP calculations, it is known that almost all the fissions that occur in the ACRR are from thermal fission of U-235. This allows the delayed neutron behavior of the ACRR to be closely approximated by the data in Table 2.1 without the need to account for the small amount of precursors created by fast fission of U-235 and U-238.

In addition to delayed neutrons from the neutron decay of fission fragments, delayed neutrons are also produced by photoneutron reactions with the beryllium in the fuel of the ACRR. This reaction is shown in Eq. (2.1).



The reaction has a gamma ray threshold energy of 1.67 MeV [Mobley & Laubenstein, 1950]. Prompt and delayed gamma rays that exceed this threshold exist in the ACRR. Of interest to the time behavior of the reactor are the photoneutrons produced by the delayed gamma rays, which come from the decay of fission fragments. Those fission fragments that produced gamma rays with energies greater than 1.67 MeV are described by Keepin [1965] using nine precursor groups shown in Table 2.2. We are able to treat these photoneutron groups as additional delayed neutron precursors groups because their source is fundamentally the same as the eight regular delayed neutron groups, in that they are both created by the decay of fission fragments.

Table 2.2: Nine-group delayed beryllium photoneutron data from Keepin for thermal fission of U-235 [Keepin, 1965].

Group Number	Half-Life	$\lambda_i$ (s <sup>-1</sup> )	$\beta_i$
1	12.8 d	6.24E-7	0.057E-5
2	77.7 h	2.48E-6	0.038E-5
3	12.1 h	1.59E-5	0.260E-5
4	3.11 h	6.20E-5	3.20E-5
5	43.2 m	2.67E-4	0.36E-5
6	15.5 m	7.42E-4	3.68E-5
7	3.2 m	3.60E-3	1.85E-5
8	1.3 m	8.85E-3	3.66E-5
9	30.6 s	2.26E-2	2.07E-5
total	--	--	15.175E-5

Most of the time the delayed beryllium photoneutrons can be ignored in calculations because as can be seen in Table 2.2, they only contribute 0.015% of the total neutron population, which is only 2% of the delayed neutron population. However, it is also important to note that for the most part, the half-lives of the delayed photoneutron groups are much longer than those of the delayed neutron groups. Because of this, after the reactor is shut down, the delayed photoneutron groups will begin to dominate as the delayed groups decay away. In Table 2.1 the longest-lived group has a half-life of about one minute, so after about 10 minutes the delayed neutron groups will contribute almost no neutrons to the system and the delayed photoneutrons will dominate. This means to calculate the reactivity multiple hours after a pulse, the delayed photoneutrons need to be accounted for.

To account for the effects that the delayed photoneutrons will have on the ACRR, the nine groups in Table 2.2 can be combined with the eight groups in Table 2.1, such that 17 total delayed neutrons groups are used for kinetics calculations. However, it needs to be recognized that the MCNP and historical  $\beta_{\text{eff}}$  values do not include the contribution from the delayed photoneutrons. By adding the total delayed photoneutron fraction from Table 2.2 to the MCNP value of 0.00723 we can approximate the total effective delayed neutron fraction with photoneutrons for the ACRR to be 0.00738. This approximation assumes that the effective photoneutron group fractions of the ACRR are the same as the  $\beta_i$  values in Table 2.2. The values in Table 2.2 were obtained by surrounding irradiated U-235 samples with 9 in. diameter beryllium spheres [Bernstein et al., 1956], which would represent the highest fraction of photoneutron production per fission. In the ACRR, attenuation and leakage of fission product gamma rays before interacting with beryllium would reduce the photoneutron fractions; however, due to the lower average energy of beryllium photoneutrons, they have increased effectiveness, which would increase the effective photoneutron fractions. Keepin [1965] discusses a process to determine the average photoneutron effectiveness from precise rod-drop experiments. And non-trivial MCNP calculation could be performed to obtain more accurate values of the delayed photoneutron fractions for the ACRR. However, determining the effective photoneutron fractions is outside the scope of this thesis, and it is believed that the values in Table 2.2 are close enough of an approximation to allow the application of the inverse method to experimental data from the ACRR to be adequately investigated.

Even though delayed neutrons only represent a small amount of the total neutron population, they are very important to the time behavior of the reactor. As will be seen in later sections, they are an essential component of the point kinetics equations and the inverse

kinetics equation. Despite not knowing the effective delayed photoneutron fractions for the ACRR, the values mentioned in this section should allow the delayed neutrons to be adequately accounted for. Future work could be done using MCNP and experiments to try to determine the true effective delayed photoneutron groups of the ACRR.

## 2.2 Reactivity

As already mentioned, this thesis is interested in the use of the inverse method to calculate the reactivity profile of ACRR pulses. In this section, reactivity and its units will be discussed to allow a better understanding of the inverse kinetics equations and the results from its application to the ACRR, which will be discussed in later chapters. In words, reactivity is a fractional measurement of the amount of deviation of a reactor's core from critical ( $k_{\text{eff}} = 1$ ), which is described by Eq. 2.2.

$$\rho = \frac{k_{\text{eff}} - 1}{k_{\text{eff}}} \quad (2.2)$$

$k_{\text{eff}}$  is the effective multiplication factor, which relates the number of neutrons in one neutron generation to the number in the next. A  $k_{\text{eff}}$  of 1 corresponds to a reactivity of 0 which means there is no deviation from criticality and that the neutron population in the reactor is constant from one neutron generation to the next. Let's assume the neutron population in a reactor is increasing by 1% each neutron generation. This would correspond to a  $k_{\text{eff}}$  of 1.01 and a reactivity of  $\sim 0.0099$ . As can be seen, reactivity is simply a unit-less decimal value as defined in Eq. 2.2. A negative decimal corresponds to a decreasing neutron population, zero corresponds to a steady state neutron population, and a positive decimal corresponds to an increasing neutron population. Simply expressing reactivity as a decimal isn't commonly used. For research reactors, it is often more useful to express reactivity in terms of the effective

delayed neutron fraction ( $\beta_{\text{eff}}$ ) as shown in Eq. 2.3. When reactivity is divided by  $\beta_{\text{eff}}$ , it is given units of dollars (\$) and cents where  $\rho = \beta_{\text{eff}}$  is referred to as \$1 of reactivity.

$$\frac{\rho}{\beta_{\text{eff}}} [\text{\$}] = \frac{k_{\text{eff}} - 1}{\beta_{\text{eff}} k_{\text{eff}}} \quad (2.3)$$

Expressing reactivity normalized to  $\beta_{\text{eff}}$  provides a convenient way to know how a reactor will respond at different reactivities. In the previous section it was described that the neutron population in a reactor consists of a combination of prompt and delayed neutrons. The presence of the delayed neutrons has the effect of slowing down the response of a reactor to changes in its reactivity. Over the interval of  $\$0 < \rho < \$1$  delayed neutrons slow down how quickly the neutron population can increase and for  $\rho < \$0$  they limit the rate at which the neutron population can decrease. Because of the sluggishness introduced by the delayed neutrons, it makes it easier and safer to operate a reactor at a critical state than if only prompt neutrons were present. If only prompt neutrons were present, changes in a reactor would occur on a time scale similar to the prompt neutron lifetime, which for the ACRR is 24  $\mu\text{s}$  (with FREC decoupled). This type of behavior is seen when reactivities greater than \$1 are inserted into a reactor. At that point, the prompt neutrons alone are enough to make the reactor critical, and they dominate the time behavior of the reactor. The important reactivity values and their influences on a reactor are summarized in Table 2.3.



Table 2.3: Important reactivity values in dollars.

Reactivity	Criticality Status	Description	Neutron Population Behavior with No External Source
$\rho < \$0$	Subcritical	The combination of prompt and delayed neutrons can't make the reactor critical	The neutron population will decay away according to the half-lives of the delayed neutron precursors.
$\rho = \$0$	Delayed Critical	The combination of prompt and delayed neutrons is just enough to make the reactor critical.	The neutron population will remain constant and if any minor fluctuations in reactivity occur, the response will be slow.
$\$0 < \rho < \$1$	Delayed Supercritical	Prompt neutrons alone aren't enough to make the reactor critical; however, with delayed neutrons the reactor is supercritical.	In this reactivity range the neutron population will increase exponentially at a rate limited by the delayed neutrons.
$\rho = \$1$	Prompt Critical	Prompt neutrons alone would make the reactor critical but with the presence of the delayed neutrons the reactor is supercritical.	The delayed neutrons are no longer required to make the reactor critical so the prompt neutron lifetime begins to dictate the exponential growth of the neutron population.
$\rho > \$1$	Prompt Supercritical	Prompt neutrons alone would make the reactor supercritical and the delayed neutrons add to the supercriticality.	Delayed neutrons have almost no effect and the neutron population will increase rapidly according to the prompt neutron lifetime.

The ACRR is routinely pulsed by quickly inserting reactivity greater than \$1 into the core. This makes the reactor prompt supercritical and causes its power to increase very rapidly. To safely operate in a prompt supercritical state, the reactor must be specially designed to avoid

damage. As mentioned in Section 1.2, the ACRR utilizes beryllium in the fuel and segmented fuel pellets to withstand the rapid increases in temperature experienced by the fuel. In addition, the ACRR is designed to stop the supercritical excursion through the use of negative temperature feedback. Without the use of a feedback mechanism, it would be impossible to mechanically insert control rods fast enough to shut the reactor down before it damaged itself. The ACRR's negative feedback relies on the Doppler broadening of U-238 and on beryllium upscatter. Both of these feedback mechanisms contribute to a decreased number of U-235 fissions as the fuel temperature increases, which effectively reduces the reactivity of the core from prompt supercritical. As the fuel cools, the negative reactivity from these effects will diminish; however, they provide ample time to insert the safety and control rods to fully shut the reactor down.

### **2.3 Derivation of the Point Kinetics Equations**

The point-reactor kinetics equations give insight into the time dependent behavior of nuclear reactors by accounting for the effects of prompt and delayed neutrons. The equations are usually solved to give the power behavior of a reactor corresponding to an inputted reactivity profile. In this section, the point-reactor kinetics equations will be derived, which will provide the starting point for the derivation of the inverse kinetics equation in Chapter 3.

The point-reactor kinetics equations can be derived from the one energy group, time- and space-dependent neutron diffusion equation shown in Eq. (2.4), where it is assumed  $D$  and  $\Sigma_a$  do not depend on position. Eq. (2.4) is simply an equation that balances the production and losses of neutrons to give the change in neutron density with time. This can be easily seen by subtracting the loss terms from the source term (the leakage term will be subtracted as the Laplacian of the flux will be negative).

$$\frac{1}{v} \frac{\partial \phi}{\partial t} + (-D \nabla^2 \phi) + \Sigma_a \phi(\mathbf{r}, t) = S_{\text{fission}}(\mathbf{r}, t) \quad (2.4)$$

$$\begin{bmatrix} \text{change in} \\ \text{neutron density} \\ \text{with time} \end{bmatrix} + \begin{bmatrix} \text{neutron} \\ \text{leakage} \\ \text{losses} \end{bmatrix} + \begin{bmatrix} \text{neutron} \\ \text{absorption} \\ \text{losses} \end{bmatrix} = \begin{bmatrix} \text{neutron} \\ \text{source} \\ \text{term} \end{bmatrix}$$

Where:

$v \rightarrow$  one-group neutron velocity [cm/s]

$\phi(\mathbf{r}, t) \rightarrow$  one-group position and time dependent neutron flux [neutrons/cm<sup>2</sup>/s]

$t \rightarrow$  time [s]

$D \rightarrow$  one-group diffusion coefficient [cm]

$\nabla^2 \rightarrow$  Laplace operator

$\Sigma_a \rightarrow$  one-group macroscopic absorption cross-section for a homogeneous mix of core materials [1/cm]

$S_{\text{fission}}(\mathbf{r}, t) \rightarrow$  fission neutron source term [neutrons/cm<sup>3</sup>/s]

Knowing that neutrons resulting from fission are a combination of prompt and delayed neutrons, the fission neutron source term can be written as shown in Eq. (2.5).

$$S_{\text{fission}}(\mathbf{r}, t) = (1 - \beta) v \Sigma_f \phi(\mathbf{r}, t) + \sum_{i=1} \lambda_i C_i(\mathbf{r}, t) \quad (2.5)$$

$$\begin{bmatrix} \text{fission} \\ \text{neutron} \\ \text{source} \end{bmatrix} = \begin{bmatrix} \text{prompt} \\ \text{neutrons} \end{bmatrix} + \begin{bmatrix} \text{delayed} \\ \text{neutrons} \end{bmatrix}$$

Where:

$\beta = \beta_{\text{eff}} \rightarrow$  effective delayed neutron fraction,  $\beta_{\text{eff}} = \sum_i \beta_i$

$(1 - \beta) \rightarrow$  fraction of neutrons emitted promptly

$v \rightarrow$  average number of neutrons released per fission (prompt + delayed)

$\Sigma_f \rightarrow$  one-group macroscopic fission cross-section [cm<sup>-1</sup>]

$\lambda_i \rightarrow$  decay constant of the  $i^{\text{th}}$  neutron precursor group [seconds<sup>-1</sup>]

$C_i(\mathbf{r}, t) \rightarrow$  concentration of the  $i^{\text{th}}$  delayed neutron precursor group at a time,  $t$ , and a point,  $\mathbf{r}$ , [number/cm<sup>3</sup>]

The prompt neutron term is expressed as a fission reaction rate weighted by  $\nu$  and the prompt neutron fraction. The delayed neutron term is expressed as a sum of the decay rates of each of the precursor groups. Including the delayed neutrons in the fission source term is essential because of the important role they play in the time behavior of a reactor. For the delayed neutron term of the fission source to be of practical use, an equation is needed to describe the time behavior of the precursor concentration. We know that in a reactor, the delayed neutron precursors are produced through fission and are then lost through radioactive decay. Knowing this, we can write Eq. (2.6) to describe the time rate of change of the  $i^{\text{th}}$  precursor group concentration.

$$\frac{\partial C_i}{\partial t} = \beta_i \nu \Sigma_f \phi(\mathbf{r}, t) - \lambda_i C_i(\mathbf{r}, t) \quad (2.6)$$

$$\left[ \begin{array}{c} \text{change of precursor} \\ \text{concentration} \\ \text{with time} \end{array} \right] = \left[ \begin{array}{c} \text{precursor} \\ \text{production} \\ \text{rate} \end{array} \right] - \left[ \begin{array}{c} \text{precursor} \\ \text{decay} \\ \text{rate} \end{array} \right]$$

Now that we have the fission source fully defined we can substitute Eq. (2.5) into Eq. (2.4) which gives us Eq. (2.7).

$$\frac{1}{\nu} \frac{\partial \phi}{\partial t} - D \nabla^2 \phi + \Sigma_a \phi(\mathbf{r}, t) = (1 - \beta) \nu \Sigma_f \phi(\mathbf{r}, t) + \sum_{i=1} \lambda_i C_i(\mathbf{r}, t) \quad (2.7)$$

To derive the point kinetics equations, the spatial dependence of Eq. (2.6) and Eq. (2.7) are eliminated so that the reactor only varies in time, such that it is essentially treated as a point, hence the name. This simplification greatly increases the ease at which the time dependence of a reactor can be studied. The spatial dependence is eliminated by assuming the neutron flux

in the core takes the shape of the fundamental mode for all time and only varies in magnitude. Because the production of the delayed neutron precursors is dependent on the flux, we know that the concentration of the neutron precursors will also take the shape of the fundamental mode for solid fuel. This allows us to separate the time and space dependence of the neutron flux and precursor concentration as follows.

$$\phi(\mathbf{r}, t) = v n(t) \psi_1(\mathbf{r}) \quad (2.8)$$

$$C_i(\mathbf{r}, t) = C_i(t) \psi_1(\mathbf{r}) \quad (2.9)$$

Where  $v n(t) = \phi(t)$  and  $n(t)$  is the neutron density [neutrons/cm<sup>3</sup>] as a function of time. And where  $\psi_1(\mathbf{r})$  is the fundamental mode solution ( $n=1$ ) to the criticality equation:

$$\nabla^2 \psi_n(\mathbf{r}) = -B_g^2 \psi_n(\mathbf{r}) \quad (2.10)$$

Substituting Eq. (2.8) and Eq. (2.9) into Eq. (2.7) and Eq. (2.6) gives Eq. (2.11) and Eq. (2.12) shown below.

$$\frac{v}{v} \frac{dn(t)}{dt} \psi_1(\mathbf{r}) - D \nabla^2 \psi_1(\mathbf{r}) v n(t) + \Sigma_a v n(t) \psi_1(\mathbf{r}) \quad (2.11)$$

$$= (1 - \beta) v \Sigma_f v n(t) \psi_1(\mathbf{r}) + \sum_{i=1}^n \lambda_i C_i(t) \psi_1(\mathbf{r})$$

$$\frac{dC_i(t)}{dt} \psi_1(\mathbf{r}) = \beta_i v \Sigma_f v n(t) \psi_1(\mathbf{r}) - \lambda_i C_i(t) \psi_1(\mathbf{r}) \quad i = 1, 2, \dots, n \quad (2.12)$$

Then by substituting Eq. (2.10) into Eq. (2.11) and canceling out the spatial dependence given by  $\psi_1(\mathbf{r})$ , from Eq. (2.11) and Eq. (2.12), we arrive at Eq. (2.13) and Eq. (2.14) which are only dependent on time.

$$\frac{dn(t)}{dt} + DB_g^2 vn(t) + \Sigma_a vn(t) = (1 - \beta) v \Sigma_f vn(t) + \sum_{i=1}^n \lambda_i C_i(t) \quad (2.13)$$

$$\frac{dC_i(t)}{dt} = \beta_i v \Sigma_f vn(t) - \lambda_i C_i(t) \quad i = 1, 2, \dots, n \quad (2.14)$$

Now all that needs to be done, is to rewrite Eq. (2.13) and Eq. (2.14) in terms of more applicable parameters, so that a more useful form of the point kinetics equations is obtained. We will begin by moving all the non-differential terms of Eq. (2.13) to the right-hand side, and factoring out  $\Sigma_a vn(t)$  to give Eq. (2.15).

$$\frac{dn(t)}{dt} = \Sigma_a vn(t) \left( -\frac{DB_g^2}{\Sigma_a} - 1 + \frac{(1 - \beta) v \Sigma_f}{\Sigma_a} \right) + \sum_{i=1}^n \lambda_i C_i(t) \quad (2.15)$$

Substituting  $k_\infty = v \Sigma_f / \Sigma_a$  and  $L^2 = D / \Sigma_a$  into Eq. (2.15) gives Eq. (2.16).

$$\frac{dn(t)}{dt} = \Sigma_a vn(t) (-B_g^2 L^2 - 1 + (1 - \beta) k_\infty) + \sum_{i=1}^n \lambda_i C_i(t) \quad (2.16)$$

Now factoring out  $(B_g^2 L^2 + 1)$  and substituting  $1/l = v \Sigma_a (B_g^2 L^2 + 1)$  gives Eq. (2.17).

$$\frac{dn(t)}{dt} = \frac{n(t)}{l} \left( -1 + \frac{(1 - \beta) k_\infty}{B_g^2 L^2 + 1} \right) + \sum_{i=1}^n \lambda_i C_i(t) \quad (2.17)$$

Substituting  $k_{\text{eff}} = k = k_\infty / (B_g^2 L^2 + 1)$  gives Eq. (2.18).

$$\frac{dn(t)}{dt} = \frac{n(t)}{l} ((1 - \beta) k - 1) + \sum_{i=1}^n \lambda_i C_i(t) \quad (2.18)$$

Now to rewrite the precursor balance equation (Eq. (2.14)) in the same parameters as Eq. (2.18)

we can substitute  $v \Sigma_f v = k_\infty \Sigma_a v = k v \Sigma_a (B_g^2 L^2 + 1) = k/l$  which gives Eq. (2.19).

$$\frac{dC_i(t)}{dt} = \frac{\beta_i k}{l} n(t) - \lambda_i C_i(t) \quad i = 1, 2, \dots, n \quad (2.19)$$

Equations (2.18) and (2.19) represent one way that the point kinetics equations can be written. They are a set of  $n+1$  coupled ordinary differential equations that describe the time-dependence of the neutron population in the reactor, where  $n$  is the total number of delayed neutron groups. The point kinetics equations are also commonly written in terms of reactivity, as defined earlier in Eq. (2.2), and the mean generation time as defined below.

$$\text{reactivity} \rightarrow \rho \equiv \frac{k - 1}{k} \quad (2.20)$$

$$\text{mean generation time} \rightarrow \Lambda \equiv \frac{l}{k} \quad (2.21)$$

Solving Eq. (2.20) for  $k$  and substituting it along with Eq. (2.21), into Eq. (2.18) and Eq. (2.19), gives the following form of the point kinetics equations:

$$\frac{dn(t)}{dt} = \frac{\rho - \beta}{\Lambda} n(t) + \sum_{i=1} \lambda_i C_i(t) \quad (2.22)$$

$$\frac{dC_i(t)}{dt} = \frac{\beta_i}{\Lambda} n(t) - \lambda_i C_i(t) \quad i = 1, 2, \dots, n \quad (2.23)$$

It is often much more useful to write Eq. (2.22) and Eq. (2.23) in terms of power rather than the neutron density. Since the neutron density is assumed to have a fixed spatial distribution, it can be regarded as any volume-averaged property that is proportional to the instantaneous neutron density at some point in the reactor, such as total number of neutrons, fission rate, power, or average power density [Hetrick, 1971]. This means we can replace the

neutron density,  $n(t)$ , with power,  $P(t)$ , as long as  $C_i$  also has units of power. Doing this gives equations (2.24) and (2.25), where each term has units of watts/s (or another proportional unit of choice).

$$\frac{dP(t)}{dt} = \frac{\rho - \beta}{\Lambda} P(t) + \sum_{i=1} \lambda_i C_i(t) \quad (2.24)$$

$$\left[ \begin{array}{c} \text{Change in} \\ \text{power with} \\ \text{time} \end{array} \right] = \left[ \begin{array}{c} \text{Prompt} \\ \text{neutron} \\ \text{contribution} \end{array} \right] + \left[ \begin{array}{c} \text{Delayed} \\ \text{neutron} \\ \text{contribution} \end{array} \right]$$

$$\frac{dC_i(t)}{dt} = \frac{\beta_i}{\Lambda} P(t) - \lambda_i C_i(t) \quad i = 1, 2, \dots, n$$

$$\left[ \begin{array}{c} \text{Change in} \\ \text{precursor} \\ \text{concentration} \\ \text{with time} \end{array} \right] = \left[ \begin{array}{c} \text{Production} \\ \text{of neutron} \\ \text{precursors} \end{array} \right] - \left[ \begin{array}{c} \text{Decay of} \\ \text{neutron} \\ \text{precursors} \end{array} \right] \quad (2.25)$$

Equations (2.24) and (2.25) are one of the most common ways to see the point reactor kinetics equations written; however, they can be written more thoroughly by expressing  $\Lambda$  in terms of  $\rho$ . By expressing  $\Lambda$  in terms of  $\rho$ , as shown in Eq. (2.26), it allows the variations in  $\Lambda$  that would occur due to changes in  $k_{\text{eff}}$ , such as those encountered during a reactor pulse, to be accounted for. In addition, expressing  $\Lambda$  in terms of  $\rho$  allows the reactivity to be explicitly solved for in the inverse kinetics equation as will be seen in the next chapter.

$$\rho \equiv \frac{k_{\text{eff}} - 1}{k_{\text{eff}}} = 1 - \frac{1}{k_{\text{eff}}} \xrightarrow{\text{Solving for } k_{\text{eff}}} k_{\text{eff}} = \frac{1}{1 - \rho} \quad (2.26)$$

$$\Lambda \equiv \frac{l}{k_{\text{eff}}} = l(1 - \rho)$$



Substituting the equation for  $\Lambda$  in terms of reactivity into the equations (2.24) and (2.25) gives the following form of the point kinetics equations.

$$\frac{dP(t)}{dt} = \frac{\rho - \beta}{l(1 - \rho)} P(t) + \sum_{i=1} \lambda_i C_i(t) \quad (2.27)$$

$$\frac{dC_i(t)}{dt} = \frac{\beta_i}{l(1 - \rho)} P(t) - \lambda_i C_i(t) \quad i = 1, 2, \dots, n \quad (2.28)$$

By substituting the definition of reactivity into equations (2.27) and (2.28) the point kinetics equations can also be expressed in terms of  $k_{\text{eff}}$ , as shown in equations (2.29) and (2.30).

$$\frac{dP(t)}{dt} = \frac{k_{\text{eff}}(1 - \beta) - 1}{l} P(t) + \sum_{i=1} \lambda_i C_i(t) \quad (2.29)$$

$$\frac{dC_i(t)}{dt} = \frac{\beta_i k_{\text{eff}}}{l} P(t) - \lambda_i C_i(t) \quad i = 1, 2, \dots, n \quad (2.30)$$

If an external neutron source is present, it can be accounted for as an additional term on the  $dP/dt$  equation, as long as it is properly normalized and expressed in the same units as  $dP/dt$ . Below, the point reactor kinetics equations in terms of reactivity are shown with a source term.

$$\frac{dP(t)}{dt} = \frac{\rho - \beta}{l(1 - \rho)} P(t) + \sum_{i=1} \lambda_i C_i(t) + S(t) \quad (2.31)$$

$$\frac{dC_i(t)}{dt} = \frac{\beta_i}{l(1 - \rho)} P(t) - \lambda_i C_i(t) \quad i = 1, 2, \dots, n \quad (2.32)$$

The point kinetics equations derived in this section provide the starting point for the derivation of the inverse kinetics equation in the next chapter. The point kinetics equations can be numerically solved using the Euler Method, as will be discussed in Chapter 4. It is important

to note that when using the point kinetics equations to model reactor behavior, feedback effects caused by changes in temperature and other phenomena need to be accounted for in the reactivity variable, which can be expressed as a function of time. To solve the  $n+1$  coupled ordinary differential equations,  $n+1$  initial conditions will be needed. It is common to choose that the reactor is initially operating at steady state,  $dP(t_0)/dt=0$ , and that all the precursor groups are in equilibrium,  $dC_i(t_0)/dt=0$ .

### 3. The Inverse Kinetics Method

In this chapter, the process known as the inverse kinetics method will be used to “invert” the point kinetics equations, such that they are solved to give the reactivity profile corresponding to a known power profile. The equation resulting from this process will be referred to as the inverse kinetics equation, and its behavior will be described in Section 3.2. The purpose of this thesis was to investigate the ability of the inverse kinetics equation to calculate reactivity profiles using experimentally gathered power profiles obtained during pulses at the ACRR. It will be seen that the inverse kinetics equation only requires that the relative power be known. As long as the signals from the radiation detectors are proportional to the power, they can be used in the inverse equation without having to be scaled; however, the detector signals still require preparation before being entered into the inverse kinetics equation, which will be described in Chapter 5.

#### 3.1 Derivation of the Inverse Kinetics Equation

The following form of the point reactor kinetics equations, given by Eq. (3.1) and Eq. (3.2), will be used to begin the inverse method derivation. As shown in Section 2.3, the mean neutron generation time,  $\Lambda$ , will be written in terms of reactivity later in the derivation.

$$\frac{dP(t)}{dt} = \frac{\rho(t) - \beta}{\Lambda} P(t) + \sum_i \lambda_i C_i(t) + S(t) \quad (3.1)$$

$$\frac{dC_i(t)}{dt} = \frac{\beta_i}{\Lambda} P(t) - \lambda_i C_i(t) \quad (3.2)$$

Where:

$P(t) \rightarrow$  power as a function of time [Watts or proportional unit]

$\rho(t) \rightarrow$  reactivity as a function of time, not in dollars or cents,  $\rho(t) = \frac{k_{\text{eff}} - 1}{k_{\text{eff}}}$

$\beta_i \rightarrow$  delayed neutron fraction of the  $i^{\text{th}}$  delayed group

$\beta = \beta_{\text{eff}} \rightarrow$  effective delayed neutron fraction,  $\beta_{\text{eff}} = \sum_i \beta_i$

$\Lambda \rightarrow$  mean neutron generation time,  $\Lambda = \frac{l}{k_{\text{eff}}}$  where,  $l$ , is the prompt neutron lifetime [seconds]

$\lambda_i \rightarrow$  decay constant of the  $i^{\text{th}}$  neutron precursor group [seconds<sup>-1</sup>]

$C_i(t) \rightarrow$  concentration of the  $i^{\text{th}}$  delayed neutron precursor group at a time,  $t$ , [number/cm<sup>3</sup>]

$S(t) \rightarrow$  Neutron source term (if one is present) [same units as  $dP/dt$ , e.g. n/s/s]

We begin by solving Eq. (3.2) for  $C_i(t)$  in terms of  $P(t)$ . Rearranging Eq. (3.2) we get:

$$\frac{dC_i(t)}{dt} + \lambda_i C_i(t) = \frac{\beta_i}{\Lambda} P(t) \quad (3.3)$$

Eq. (3.3) is an ordinary differential equation that can be solved using an integrating factor.

$$\text{integrating factor} \rightarrow \mu(t) = e^{\int_{t_0}^t \lambda_i dt} = e^{\lambda_i(t-t_0)} \quad (3.4)$$

Multiplying both sides of Eq. (3.3) by the integrating factor gives Eq. (3.5).

$$\frac{dC_i(t)}{dt} (e^{\lambda_i(t-t_0)}) + \lambda_i C_i(t) (e^{\lambda_i(t-t_0)}) = \frac{\beta_i}{\Lambda} P(t) (e^{\lambda_i(t-t_0)}) \quad (3.5)$$

Recognizing that the left-hand side of Eq. (3.5) is the derivative of a product of two functions of time, it can be rewritten as shown in Eq. (3.6).

$$\frac{d}{dt} (C_i(t) e^{\lambda_i(t-t_0)}) = \frac{\beta_i}{\Lambda} P(t) (e^{\lambda_i(t-t_0)}) \quad (3.6)$$

Integrating both sides of Eq. (3.6) with respect to time, from the initial time,  $t_0$ , to some later time,  $t$ , where  $t'$  is the integration variable, gives Eq. (3.8).

$$\int_{t_0}^t \frac{d}{dt'} (C_i(t') e^{\lambda_i(t'-t_0)}) dt' = \int_{t_0}^t \frac{\beta_i}{\Lambda} P(t') (e^{\lambda_i(t'-t_0)}) dt' \quad (3.7)$$

$$C_i(t) e^{\lambda_i(t-t_0)} - C_i(t_0) = \int_{t_0}^t \frac{\beta_i}{\Lambda} P(t') (e^{\lambda_i(t'-t_0)}) dt' \quad (3.8)$$

Solving Eq. (3.8) for  $C_i(t)$  gives Eq. (3.9).

$$C_i(t) = e^{-\lambda_i(t-t_0)} \left( C_i(t_0) + \int_{t_0}^t \frac{\beta_i}{\Lambda} P(t') (e^{\lambda_i(t'-t_0)}) dt' \right) \quad (3.9)$$

Rewriting the exponential terms and distributing into the brackets gives Eq. (3.10).

$$C_i(t) = e^{-\lambda_i t} e^{\lambda_i t_0} C_i(t_0) + e^{-\lambda_i t} e^{\lambda_i t_0} \int_{t_0}^t \frac{\beta_i}{\Lambda} P(t') (e^{\lambda_i t'} e^{-\lambda_i t_0}) dt' \quad (3.10)$$

Because the exponential terms outside the integral are constant relative to the integration variable, they can be moved inside the integral and after simplifying we arrive at Eq. (3.11).

$$C_i(t) = e^{-\lambda_i t} e^{\lambda_i t_0} C_i(t_0) + \int_{t_0}^t \frac{\beta_i}{\Lambda} P(t') (e^{-\lambda_i(t-t')}) dt' \quad (3.11)$$

For any physical system, we can assume that the initial precursor concentration,  $C_i(t_0)$ , goes to zero as the initial time,  $t_0$ , goes to  $-\infty$ . Applying this assumption to Eq. (3.11) gives Eq. (3.12).

$$C_i(t) = \int_{-\infty}^t \frac{\beta_i}{\Lambda} P(t') (e^{-\lambda_i(t-t')}) dt' \quad (3.12)$$

If we make the u-substitution that,  $u = t - t'$ , then  $dt' = -du$  and the limits of integration become  $\infty$  to 0, which is shown in Eq. (3.13).

$$C_i(t) = - \int_{\infty}^0 \frac{\beta_i}{\Lambda} P(t - u) (e^{-\lambda_i u}) du \quad (3.13)$$

By flipping the limits of integration and eliminating the negative sign we arrive at Eq. (3.14).

$$C_i(t) = \int_0^{\infty} \frac{\beta_i}{\Lambda} P(t - u) e^{-\lambda_i u} du \quad (3.14)$$

Substituting Eq. (3.14) into Eq. (3.1) gives Eq. (3.15).

$$\frac{dP(t)}{dt} = \frac{\rho(t) - \beta}{\Lambda} P(t) + \int_0^{\infty} \frac{P(t - u)}{\Lambda} \sum_i \lambda_i \beta_i e^{-\lambda_i u} du + S(t) \quad (3.15)$$

Defining the delayed neutron kernel as follows

$$\text{Delayed neutron kernel} \rightarrow D(u) \equiv \sum_i \frac{\lambda_i \beta_i}{\beta} e^{-\lambda_i u} \quad (3.16)$$

and substituting it into Eq. (3.15) we arrive at Eq. (3.17), which is an integro-differential (contains integrals and derivatives) form of the point reactor kinetics equations.

$$\frac{dP(t)}{dt} = \frac{\rho(t) - \beta}{\Lambda} P(t) + \frac{\beta}{\Lambda} \int_0^{\infty} D(u) P(t - u) du + S(t) \quad (3.17)$$

We can now solve Eq. (3.17) for reactivity as a function of time for a given power profile.

Multiplying both sides by  $\Lambda$  and dividing by  $P(t)$  gives Eq. (3.18).

$$\frac{dP}{dt} \left( \frac{1}{P(t)} \right) \Lambda = \rho(t) - \beta + \frac{\beta}{P(t)} \int_0^{\infty} D(u) P(t - u) du + \left( \frac{\Lambda}{P(t)} \right) S(t) \quad (3.18)$$

Solving for  $\rho(t)$  gives Eq. (3.19).

$$\rho(t) = \beta + \frac{dP}{dt} \left( \frac{1}{P(t)} \right) \Lambda - \frac{\beta}{P(t)} \int_0^{\infty} D(u) P(t - u) du - \left( \frac{\Lambda}{P(t)} \right) S(t) \quad (3.19)$$

As mentioned in Section 2.3,  $\Lambda$  is dependent on the reactivity, which means reactivity can be more explicitly solved for in Eq. (3.19). To do this we can substitute Eq. (2.26) into Eq. (3.19) to get Eq. (3.20).

$$\Lambda = \frac{l}{k_{\text{eff}}} = l - l\rho(t) \quad (2.26)$$

$$\rho(t) = \beta + \frac{dP}{dt} \left( \frac{1}{P(t)} \right) (l - l\rho(t)) - \frac{\beta}{P(t)} \int_0^{\infty} D(u) P(t - u) du - \left( \frac{S(t)}{P(t)} \right) (l - l\rho(t)) \quad (3.20)$$

Solving Eq. (3.20) for  $\rho(t)$  gives Eq. (3.21) which is very similar to Eq. (3.19); however, it accounts for the slight variations in  $\Lambda$  due to changes in  $k_{\text{eff}}$  that occur during a pulse.

$$\rho(t) = \frac{1}{1 + l \frac{dP}{dt} \left( \frac{1}{P(t)} \right) - l \frac{S(t)}{P(t)}} \left[ \beta + l \frac{dP}{dt} \left( \frac{1}{P(t)} \right) - \frac{\beta}{P(t)} \int_0^{\infty} D(u) P(t-u) du - l \frac{S(t)}{P(t)} \right] \quad (3.21)$$

To have the outputted reactivity in units of dollars [\$] we can express  $\rho$  in terms of  $\beta$  as described in Section 2.2. This is done by dividing both sides of Eq. (3.21) by  $\beta$  giving Eq. (3.22).

$$\frac{\rho(t)}{\beta} [\text{\$}] = \frac{1}{1 + l \frac{dP}{dt} \left( \frac{1}{P(t)} \right) - l \frac{S(t)}{P(t)}} \left[ 1 + \frac{l}{\beta} \frac{dP}{dt} \left( \frac{1}{P(t)} \right) - \frac{1}{P(t)} \int_0^{\infty} D(u) P(t-u) du - \frac{l}{\beta} \frac{S(t)}{P(t)} \right] \quad (3.22)$$

Eq. (3.22) is the form of the inverse kinetics equation that will be used for the calculations in this thesis. As can be seen in Eq. (3.16), the delayed neutron kernel,  $D(u)$ , is a known function because the delayed neutron data is known. The prompt neutron lifetime,  $l$ , is also a known quantity for the ACRR, and has been obtained through MCNP calculations. It will be assumed that  $l$  is constant over the duration of a pulse; however, it does change slightly depending on the position of the control, safety, and transient rods. The source is written as a function of time in Eq. (3.22) but frequently the source is a constant or nonexistent. The ACRR does not use an external neutron source for startup because there are sufficient background neutrons from  $(\alpha, n)$  and  $(\gamma, n)$  reactions with the beryllium in the fuel. These background neutrons were found to be negligible for the pulse sizes and time durations investigated in this thesis, which will be further discussed in Section 3.3.

### 3.2 Understanding the Inverse Kinetics Equation Solution

To develop an understanding of the inverse kinetics equation, we will consider it to be made up of four components, each of which will be studied separately. These four components



will be referred to as the coefficient, the prompt term, the integral term, and the source term as shown below. To assist in understanding the contribution of each component, a pulse power profile, generated by numerically solving the point kinetics equations, will be used to provide data for  $P(t)$  so that the behavior of each component can be visualized. To generate the power profile, the prompt neutron lifetime and the delayed neutron data for the ACRR were used along with a made-up reactivity profile. In this section, it will be assumed that there is no source; in Section 3.3 the effects of a source will be considered.

$$\frac{\rho(t)}{\beta} [\$] = \underbrace{\frac{1}{1 + l \frac{dP}{dt} \left( \frac{1}{P(t)} \right) - l \frac{S(t)}{P(t)}}}_{\text{Coefficient}} \left[ \underbrace{l \frac{dP}{dt} \left( \frac{1}{P(t)} \right)}_{\text{Prompt}} + 1 - \underbrace{\frac{1}{P(t)} \int_0^\infty D(u) P(t-u) du}_{\text{Delayed}} - \underbrace{\frac{l S(t)}{\beta P(t)}}_{\text{Source}} \right]$$

Figure 3.1 shows the simulated pulse power profile that will be used to study the behavior of the components of the inverse kinetics equation. The figure also shows the corresponding reactivity profile that was used to create the power profile. The reactor was chosen to be at constant power for the first 2 s and then reactivity was inserted at a constant rate between 2 s and 2.05 s such that \$3 of total reactivity would be inserted. After this, negative reactivity feedback was simulated by reducing the reactivity at a rate proportional to the change in energy released. Once the pulse released the specified amount of energy, negative reactivity was inserted at a constant rate such that the reactor would be -\$5 subcritical after 0.2 s. The reactivity was then held at -\$5. This pulse does not represent the exact same behavior that we would expect to see from the ACRR, but it provides a noise-free pulse power profile that will allow us to study the inverse kinetics equation.

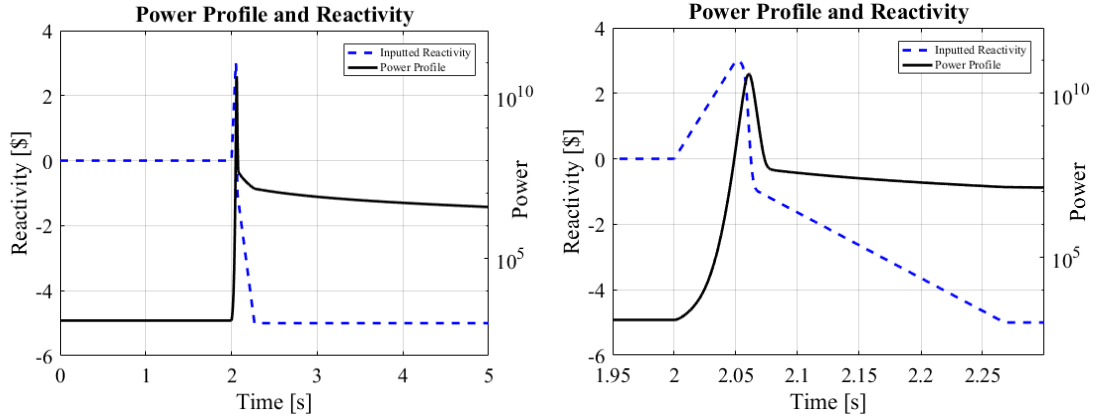


Figure 3.1: Simulated power profile and corresponding reactivity profile, generated using the point kinetics equations. This example will be used to study the inverse kinetics equation. The right plot is zoomed in, in time, to better show the pulse.

First, we will consider the coefficient (without a source) whose values are shown in Figure 3.2. The coefficient results from substituting Eq. (2.26) into Eq. (3.19) to account for the variations in  $\Lambda$  experienced during large changes in reactivity. The coefficient only deviates slightly from unity during the time of the pulse, so multiplying each of the terms in the brackets by the coefficient will have minimal effect on the calculated reactivity. For this reason, the substitution of Eq. (2.26) is often neglected. However, the coefficient is accounted for in the inverse kinetics calculations used in this thesis.

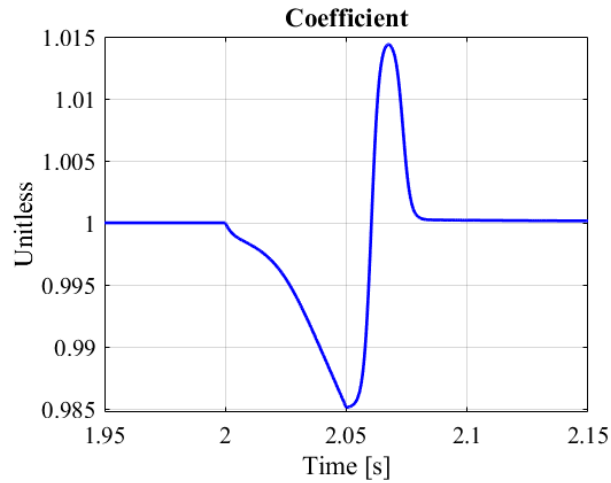


Figure 3.2: The coefficient of the inverse kinetics equation at the time of the pulse.

The prompt term and the product of the prompt term and coefficient are shown in Figure 3.3. The coefficient has only a slight effect on the prompt term as shown by the data point. It is also easy to see that the coefficient has the same shape as the prompt term but it is inverted, shifted up by 1, and scaled differently. The similar shape arises because they are both dictated by the normalized derivative of the power which is shown in Figure 3.4. The coefficient remains close to unity though, because the derivative is multiplied by the prompt neutron lifetime ( $24\mu\text{s}$ ) which is very small, whereas in the prompt term, the derivative is multiplied by  $l/\beta$  (0.0033), which is about 138 times larger. As expected, because of the derivative, the prompt term contributes to the reactivity when the power changes rapidly with time. These rapid changes in power occur when positive or negative reactivity is quickly inserted. When the reactivity is greater than  $\$1$ , these rapid changes cause the power to increase rapidly according to the prompt neutron lifetime. In this example, these rapid changes are the insertion of positive reactivity before the peak, the duration at which the total reactivity is greater than  $\$1$ , and the insertion of negative reactivity due to feedback after the peak of the pulse. The negative reactivity inserted at a constant rate after the feedback, does not occur at a fast-enough rate to be appreciably captured by the prompt term.

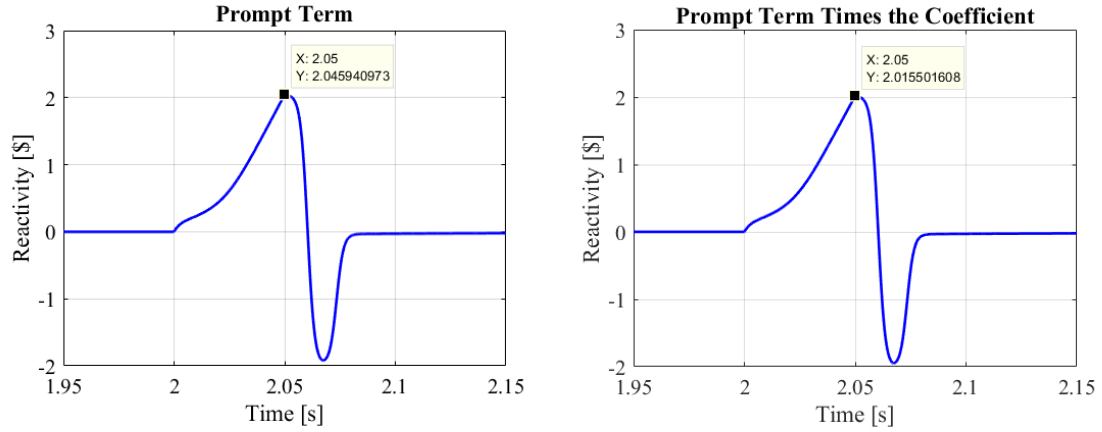


Figure 3.3: Prompt term and the product of the prompt term and the coefficient. The data point shows the small effect that the coefficient has at its point of largest deviation from unity.

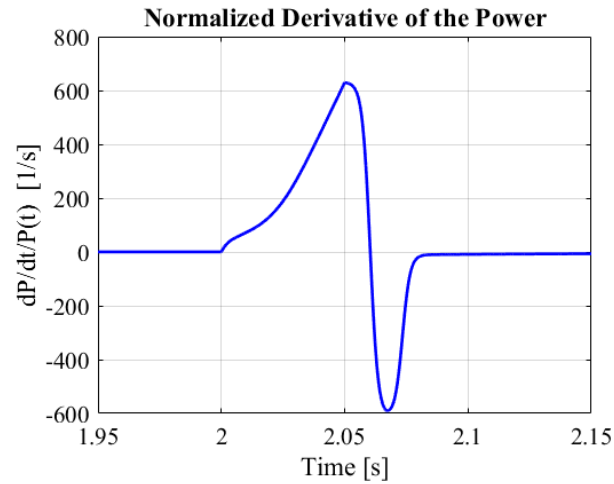


Figure 3.4: The derivative of the power profile, normalized to  $P(t)$ .

The delayed term of the inverse kinetics equation is dependent on the delayed neutron data because of the presence of the delayed neutron kernel within the integral. The delayed term and the delayed neutron kernel are shown below for convenience.

$$\text{Delayed term} \equiv 1 - \frac{1}{P(t)} \int_0^{\infty} D(u) P(t-u) du$$

$$\begin{array}{l} \text{Delayed} \\ \text{neutron} \\ \text{kernel} \end{array} \rightarrow D(u) \equiv \sum_{i=1}^n \frac{\lambda_i \beta_i}{\beta} e^{-\lambda_i u} = \frac{\lambda_1 \beta_1}{\beta} e^{-\lambda_1 u} + \frac{\lambda_2 \beta_2}{\beta} e^{-\lambda_2 u} + \dots + \frac{\lambda_n \beta_n}{\beta} e^{-\lambda_n u} \quad (3.16)$$

Where:

$\lambda_i \rightarrow$  decay constant of the  $i^{\text{th}}$  neutron precursor group [seconds<sup>-1</sup>]

$\beta_i \rightarrow$  delayed neutron fraction of the  $i^{\text{th}}$  delayed group

$\beta = \beta_{\text{eff}} \rightarrow$  effective delayed neutron fraction,  $\beta_{\text{eff}} = \sum_i \beta_i$

$u \rightarrow$  time after a fission event [seconds]

$n \rightarrow$  the number of delayed neutron groups

The delayed neutron kernel for the 17 groups of delayed neutron data for the ACRR is shown in Figure 3.5. It gives the probability of delayed neutron emission within a small time  $du$ , about a time  $u$ , after a fission event. It is defined such that integrating over all time gives a 100% probability of delayed neutron emission, as would be expected.

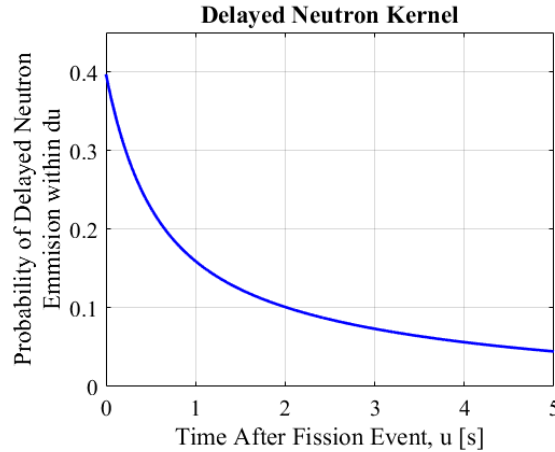


Figure 3.5: Delayed neutron kernel generated using the ACRR's 17 delayed neutron groups.

The integral within the delayed term is the mathematical convolution of the delayed neutron kernel and the power history, which gives the total emission rate of delayed neutron at a time  $t$  by accounting for the production and decay of all precursors created prior to and

including time  $t$ . If the integral is less than  $P(t)$ , the delayed term will give a value between 1 and 0, and if the integral is greater than  $P(t)$ , it will give a negative value. Since the delayed term can only capture reactivity values up to  $\beta$ , the prompt term will capture the reactivity behavior that exceeds  $\beta$ , which is expected because the prompt neutrons will be dictating the reactor power at that point. When the integral exceeds  $P(t)$  it means the delayed neutron population is dominating the total neutron population, which means the reactor is subcritical, and the degree to which the integral is greater than  $P(t)$  quantifies how subcritical the reactor is. Figure 3.6 shows the values of the integral evaluated at each  $t$ . These values are proportional to the delayed neutron emission rate and the total precursor concentration. As can be seen, the precursor concentration is initially at a constant value greater than zero when the reactor is at constant power, and then during the pulse many precursors are created, which then exponentially decay away. Figure 3.7 shows the delayed term and the product of the delayed term and the coefficient, and as was the case with the prompt term, the coefficient only has a minimal effect on the values even at the point of its maximum deviation from unity, as shown by the data point.

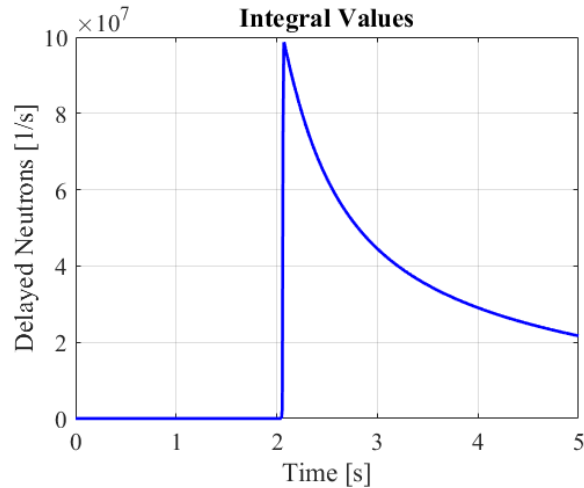


Figure 3.6: Integral values of the delayed term. These values are proportional to the delayed neutron emission rate and the precursor concentration in the reactor.

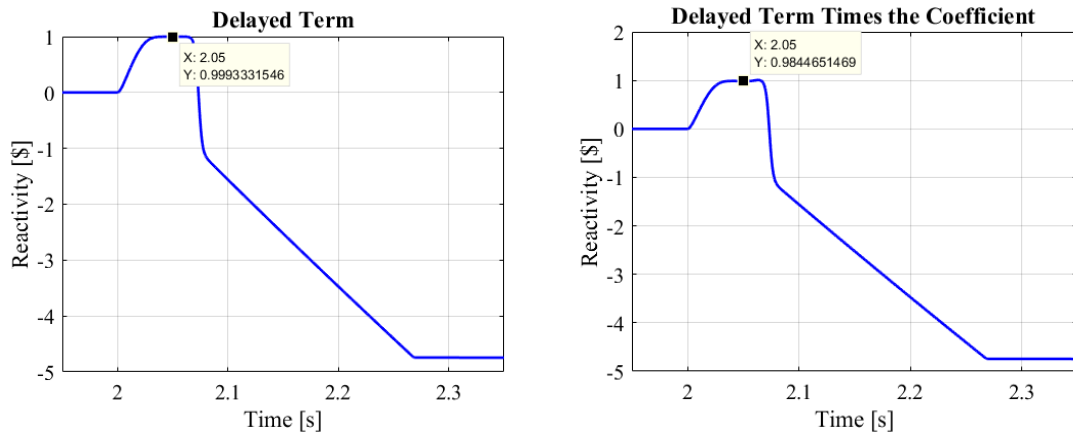


Figure 3.7: The delayed term of the inverse kinetics equation and the product of it with the coefficient. The data point shows the small effect that the coefficient has at its point of largest deviation from unity.

As can be seen, the integral requires knowing the power history of the reactor infinitely far back in time. This accounts for all the precursors created at earlier power levels since there is always a small chance they could decay at a much later time, which is evident by the delayed neutron kernel always giving a probability greater than zero. To accurately solve the integral in real world applications, an initial condition can be assumed or a sufficient amount of power data can be gathered before the event of interest to allow for a good approximation of the

precursor concentration by the time of the event. In this example, the initial condition used to create the power profile in Figure 3.1 was known, so it was used to analytically solve for the contribution to the integral from power levels before  $t = 0$ . The initial condition (IC) was simply that the power was constant for all times prior to  $t = 0$  and that the precursor groups were in equilibrium at  $t = 0$ . The integral contribution due to the constant power values before  $t = 0$  is given by Eq. (3.23).

$$\text{Integral IC} = P_0 \int_t^{\infty} D(u) du \quad (3.23)$$

Where  $P_0$  is the power at  $t = 0$  and where integrating from  $u = t$  to  $u = \infty$  corresponds to the powers  $P(t = 0)$  to  $P(t = -\infty)$ , which is when the power is constant. Substituting the delayed neutron kernel gives Eq. (3.24) where  $\alpha_i = \beta_i/\beta$ .

$$\text{Integral IC}(t) = P_0 \int_t^{\infty} [\alpha_1 \lambda_1 e^{-\lambda_1 u} + \alpha_2 \lambda_2 e^{-\lambda_2 u} + \dots + \alpha_n \lambda_n e^{-\lambda_n u}] du \quad (3.24)$$

Evaluating the definite integral gives the integral IC as a function of  $t$  as shown by Eq. (3.25).

$$\text{Integral IC}(t) = P_0 [\alpha_1 e^{-\lambda_1 t} + \alpha_2 e^{-\lambda_2 t} + \dots + \alpha_n e^{-\lambda_n t}] = P_0 \sum_{i=1}^n \alpha_i e^{-\lambda_i t} \quad (3.25)$$

For every  $t$  at which the reactivity is calculated, Eq. (3.25) evaluated at  $t$ , will be added to the numerical portion of the integral, calculated from  $u = 0$  to  $u = t$  using the power data from  $P(t)$  to  $P(0)$ . The integral values shown in Figure 3.6 account for the initial condition. If the initial condition isn't used, the integral will behave as if the precursor concentration at  $t = 0$  is zero rather than the equilibrium amount. Figure 3.8 shows the calculated reactivity with and without accounting for the initial condition. As can be seen, when the IC isn't specified



the inverse kinetics equation assumes the reactor is initially prompt critical (\$1) since no delayed neutrons are present to help make the reactor critical. As precursors are generated the reactivity slowly moves towards \$0 at a rate dictated by the decay constants of the precursor groups. However, in reality the precursor concentration was initially in equilibrium and the reactivity was \$0 up until the time of the pulse. In this example, not accounting for the IC has little effect on the calculated reactivity after the pulse. This is because the large number of precursors created during the pulse dwarf the effects of the relatively small amount of precursors created before the pulse.

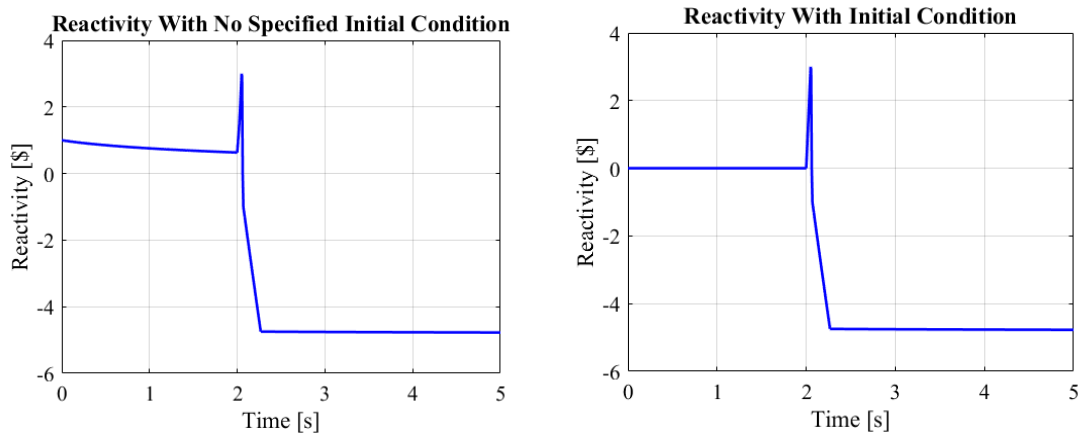


Figure 3.8: The left plot shows the errors that occur if the initial condition isn't accounted for and the right plot shows the correct reactivity obtained by accounting for the initial condition.

The plot of the reactivity accounting for the initial condition in Figure 3.8, was obtained by adding the product of the prompt term and the coefficient, and the product of the delayed term and the coefficient. Figure 3.9 shows the prompt and the delayed contributions overlaid with the calculated reactivity, and Figure 3.10 shows the calculated reactivity compared to the actual reactivity used to create the power profile. As can be seen, by numerically solving the inverse kinetics equation, the actual reactivity is closely obtained. However, the inverse kinetics reactivity begins to deviate from the inputted reactivity as negative reactivity is

linearly inserted and results in the calculated reactivity reaching  $-4.77$  rather than  $-5$ . The cause of this discrepancy is thought to be due to errors in the power profile created by the point kinetics code. As will be seen in Chapter 4, the inverse kinetics code accurately calculates the reactivity corresponding to pulses simulated in Razorback, so the errors are not in the inverse kinetics calculation.

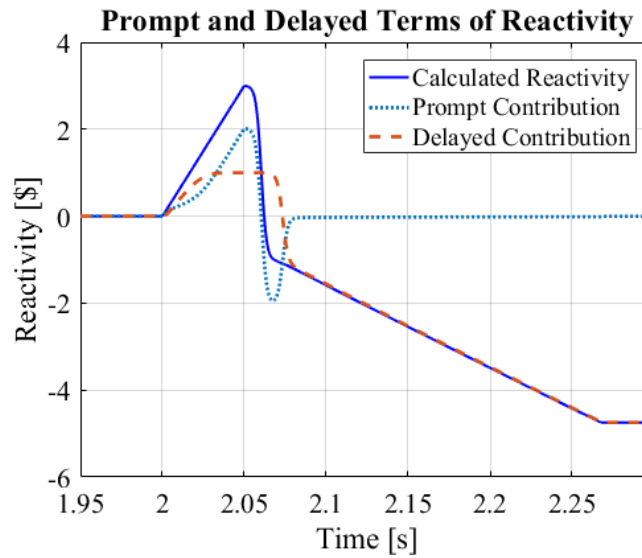


Figure 3.9: Plot showing the product of the prompt term with the coefficient, the product of the delayed term with the coefficient, and the calculated reactivity which is the sum of those two profiles.

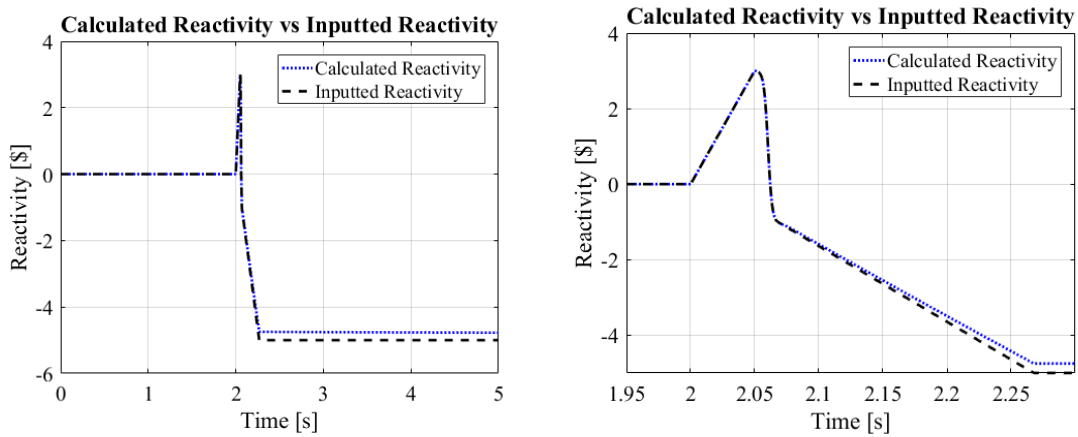


Figure 3.10: Plots showing the reactivity calculated using the inverse kinetics equation, compared to the reactivity inputted into the point kinetics equations. The plot on the right is zoomed in, in time.

### 3.3 External Source Considerations

External neutron sources used in nuclear reactors are usually very small relative to the typical operating powers of the reactor. For this reason, the source term of the inverse kinetics equation will only have an appreciable effect on the calculated reactivity when the power of the reactor is low and similar to that of the source. When at these low powers, if the source isn't accounted for, the calculated reactivity will be close to zero even if in reality the reactor is many dollars subcritical, which is described by Hoogenboom and Van Der Sluijs [1988].

As mentioned earlier, the ACRR does not utilize a dedicated external neutron source for reactor start up. Instead, it relies on neutrons from  $(\alpha,n)$  and  $(\gamma,n)$  reactions with the beryllium in the fuel. This results in a small and relatively constant neutron source that is always present in the core; however, the magnitude of the source can vary slightly depending on operation history due to buildup of the longer lived photoneutron precursors. It was thought that this source was small enough that the source term could be neglected when calculating the reactivity corresponding to ACRR pulses. However, when using experimental data, the reactivity was found to approach \$0 following a pulse, rather than the expected value of about -\$10. This type of behavior, as shown in Figure 3.11, was similar to what would be expected when the presence of a source is not accounted for. However, it was found that a very large source would be needed to cause behavior like this. It was known that a source of this magnitude did not exist in the reactor so this behavior was attributed to the unwanted detection of activation and fission product gamma rays. The detection of these gamma rays distorts the proportionality of the detector signal away from the shape of the true power profile. This makes it appear after the pulse, that the power is not dropping as fast as it actually is, which causes

the calculated reactivity to be less negative than it really is. Attempts to subtract the contribution of these gammas from the detector signal will be discussed in Chapter 5.

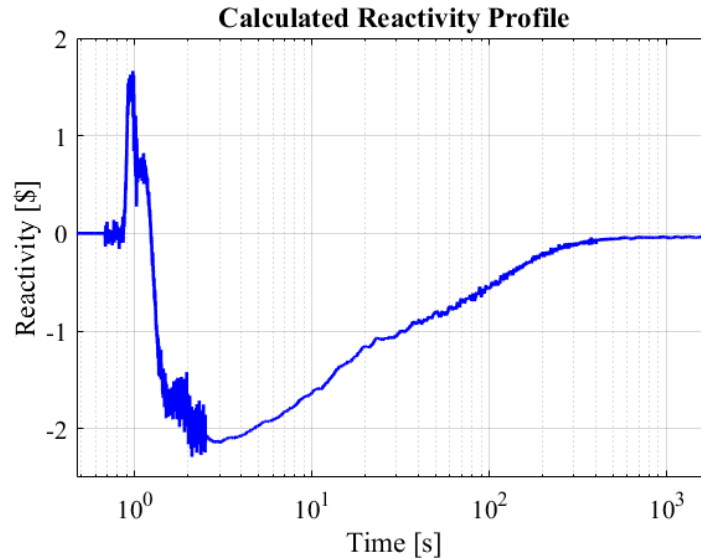


Figure 3.11: ACRR reactivity profile calculated using experimental data and not accounting for a source. Following the pulse, the reactivity should drop to about -\$10 and remain there; however, it was found to only drop to a few dollars negative and then approached zero because of detection of fission product and activation gamma rays.

The presence of these gamma rays make it difficult to determine if the small ( $\alpha, n$ ) and ( $\gamma, n$ ) source that is always present in the ACRR core has a measurable effect on the calculated reactivity. Due to the very small size of this source it is thought that if it was to have an effect it would not be until hours after a pulse when the power had dropped to a sufficiently low level. The large amount of activation and fission products and their associated gamma rays present a much greater concern than the possible source effects. For this reason, focus was placed on subtracting away the unwanted gamma contribution, and it was chosen to neglect the source term during calculations because its exact source strength was unknown and assumed to be very small.

## 4. Numerical Solutions to the Inverse Kinetics Equation

A computer code was written in Fortran 95 to numerically solve the inverse kinetics equation. Fortran 95 was used because it provided the author an opportunity to learn a compiled language, and it is used in other codes of interest at Sandia National Laboratories. The code was written to read in time and power data from a text file and then output the corresponding time and reactivity data to another text file. In this chapter, the numerical techniques used and the validation of the computer code will be discussed. The processing of experimental data before inputting it into the inverse kinetics code was performed using MATLAB, which will be discussed in Chapter 5. Appendix A, shows a flow chart of the calculations performed in the inverse kinetics code.

### 4.1 Numerical Solution

The inverse kinetics equation is written below for reference. As previously described,  $l$ ,  $\beta$ , the  $\beta_i$ 's, and the  $\lambda_i$ 's are all known constants for the ACRR.  $P(t)$  data is read in to the code and placed in to a time and power array that provides  $P(t)$  for discrete times. In the code,  $S(t)$  can easily be set equal to a constant value, but for ACRR calculations it was set equal to zero.

$$\frac{\rho(t)}{\beta} [\$] = \frac{1}{1 + l \frac{dP}{dt} \left( \frac{1}{P(t)} \right) - l \frac{S(t)}{P(t)}} \left[ \frac{l}{\beta} \frac{dP}{dt} \left( \frac{1}{P(t)} \right) + 1 - \frac{1}{P(t)} \int_0^{\infty} D(u) P(t-u) du - \frac{l}{\beta} \frac{S(t)}{P(t)} \right] \quad (4.1)$$

Where,  $D(u) = \sum_{i=1}^n \frac{\lambda_i \beta_i}{\beta} e^{-\lambda_i u} \quad i = 1, 2, \dots, n$

To calculate the derivative of the power, a forward finite difference method was used as shown in Eq. (4.2). As long as the data had a small enough time step, the forward method

was found to do a good job approximating the derivative during the rapid increase in power during a pulse and also elsewhere when the changes weren't as rapid.

$$\frac{dP(t_i)}{dt} = \frac{P(t_{i+1}) - P(t_i)}{t_{i+1} - t_i} \quad (4.2)$$

Numerically solving the integral isn't as straight forward as the derivative. As mentioned in Section 3.2, the integral is the mathematical convolution of the delayed neutron kernel and the power profile. The convolution essentially takes the delayed neutron kernel from Figure 3.5 and reflects it about the y-axis and shifts it over the power profile as  $t$  increases. For each  $t$  the product of the overlapping delayed neutron kernel and the power profile values is obtained and integrated. Figure 4.1 gives a graphical representation of the overlapping of the delayed neutron kernel and the power profile corresponding to calculating the integral at  $t = 1$ .

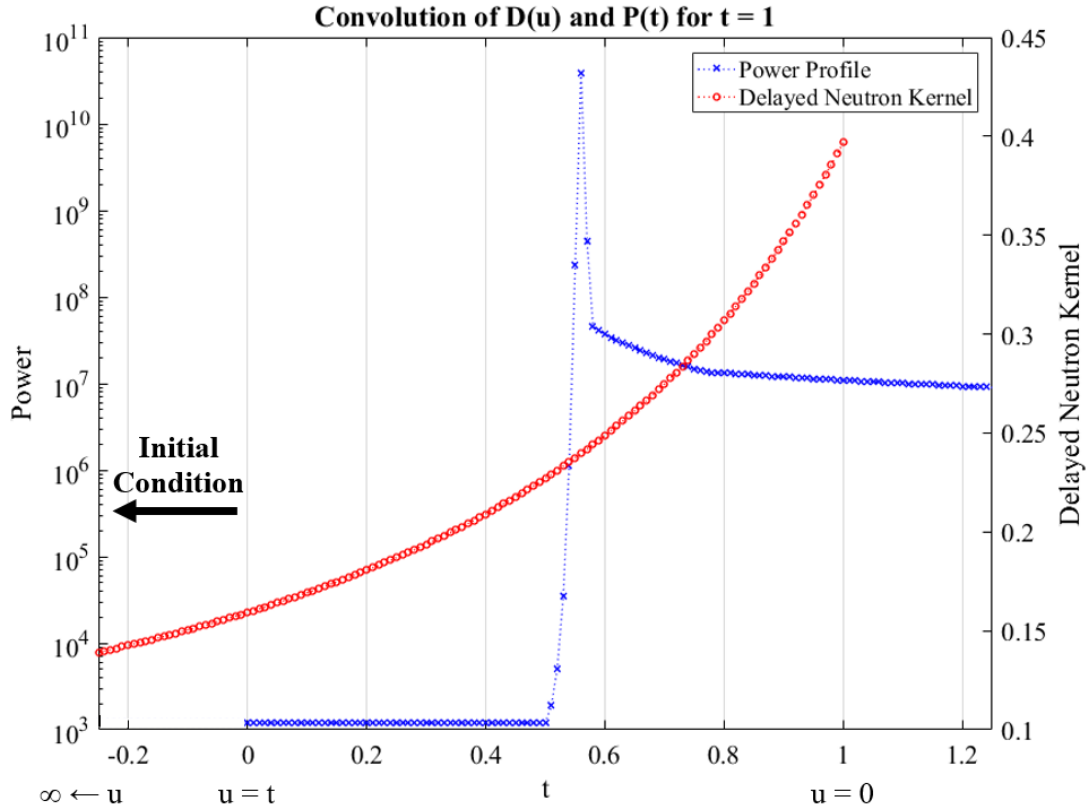


Figure 4.1: Example showing how the delayed neutron kernel and the power profile would overlap when evaluating the convolution integral for  $t = 1$ . A coarse time step is shown so that it can be seen that the delayed neutron kernel must be evaluated at times corresponding to the power data points previous to  $t$ .

When taking the product of the delayed neutron kernel and the power profile, the time at which the reactivity is being calculated ( $t = 1$  in this example), is weighted most heavily by the delayed neutron kernel while older power values will be weighted less and less. When the curve of the weighted power values is integrated from  $u = 0$  to  $u = \infty$ , a value proportional to the total emission rate of delayed neutron at time  $t$  is obtained. In reality only a finite amount of power data is available, so an initial condition is required to determine the contribution of the integral from times prior to the known data. When applying the inverse kinetics equation to experimental data from ACRR pulses, it was assumed that the reactor had been operating at

constant power for infinite time before the pulse and that all the precursor groups were in equilibrium. This initial condition was chosen because the ACRR is typically operated at a low constant power for several minutes before a pulse, which is long enough for the majority of the precursor groups to reach an equilibrium concentration. Accounting for the constant power initial condition allowed the reactivity to accurately be calculated during the constant power region before a pulse. If the initial condition isn't accounted for, behavior similar to that shown in Figure 3.8 occurs. As described in Section 3.2, the constant power initial condition can be analytically solved as a function of  $t$ , and is given by Eq. (4.3) [Eq. 3.25 in Ch. 3]. Where  $P_0$  is usually the first data point, assuming that the data begins during the period of constant power before a pulse.

$$\text{Integral IC (t)} = P_0[\alpha_1 e^{-\lambda_1 t} + \alpha_2 e^{-\lambda_2 t} + \dots + \alpha_n e^{-\lambda_n t}] = P_0 \sum_{i=1}^n \alpha_i e^{-\lambda_i t} \quad (4.3)$$

Eq. (4.3) gives the value of the integral for  $t < u < \infty$ . This means that the integral of the inverse kinetics equation can be rewritten with different limits of integration as shown in Eq. (4.4).

$$\int_0^{\infty} D(u) P(t-u) du = P_0 \sum_{i=1}^n \alpha_i e^{-\lambda_i t} + \int_0^t D(u) P(t-u) du \quad (4.4)$$

By using the analytical initial condition solution, the integral can now be solved numerically since it only requires integration over the known data. It is more intuitive to write the numerical solution to the integral if we substitute  $u = t - t'$  and  $du = -dt'$ , which were replaced when the  $u$ -substitution was performed during the derivation in Section 3.1. If  $t_N$  is the  $N^{\text{th}}$  data point in the array and the time at which the reactivity is wanted, the numerical solution to the integral using the trapezoidal rule can be written as shown in Eq. (4.5).



$$\int_t^0 D(t - t') P(t') dt' \approx \sum_{j=0}^{N-2} \left[ \left( \frac{D(t_N - t_{N-j})P_{N-j} + D(t_N - t_{N-j-1})P_{N-j-1}}{2} \right) (t_{N-j} - t_{N-j-1}) \right] \quad (4.5)$$

As can be seen, the neutron kernel will need to be evaluated at every time given by  $t_N - t_{N-j}$ ; whereas, the time and power values need to just be pulled from the proper location within their arrays. If the time and power data have a constant time step the delayed neutron kernel values can easily be pre-calculated and stored in an array that will be the same size as the time and power arrays. Doing this eliminates unnecessarily evaluating the neutron kernel at repeated values when calculating the entire reactivity profile. However, if the time step of the data is not constant, the number of repeated neutron kernel values is greatly reduced, if any at all. This occurs because with non-constant time step data, the delayed neutron kernel values will rarely line up exactly with the power data as the neutron kernel is shifted to the next time.

The experimental power data collected during a pulse at the ACRR typically has a 20  $\mu$ s “short” time step within a 2 s window around the pulse and a 20 ms “long” time step elsewhere. It was found that parsing the data to a 1 ms time step still gave sufficient resolution to accurately calculate the reactivity during the pulse, and it greatly reduced the computational time. When looking at data up to 1000 s seconds after the pulse, the short data was typically parsed to 1 ms and the long data would be linearly interpolated to also have a 1 ms time step. This allowed us to take advantage of pre-calculating the delayed neutron kernel values to reduce computational time. However, beyond a 1000 s or so, it became more beneficial to sacrifice the ability to pre-calculate the neutron kernel values and to use a variable time step instead. When using a variable time step, the data would typically still be parsed to 1 ms during

the pulse but after the pulse the time step would be linearly increased up to about 0.1 s since less resolution was needed as the rate of change of the power decreased. The steps used to prepare the experimental data will be further discussed in Chapter 5.

Computational time could be saved by approximating the integral by only integrating backwards over a finite amount of time rather than always integrating back to the first data point. In the case of this thesis, this was not a good option because the contribution of the relatively long-lived beryllium photoneutron precursors was to be studied. However, in cases where only the typical U-235 precursors are relevant, a good approximation could be made by only integrating over the last 600 s or so of data. As the half-life of the longest-lived U-235 precursor is only 55.6 s, precursors from data prior to 600 s of the current time, will have all gone through at least 10 half-lives, and will contribute very few delayed neutrons at the current time in most situations. If the inverse kinetic equation was used to calculate the reactivity of a reactor in real time, it would be necessary to only integrate back over a limited amount of time, because integrating over all the gathered data would not be practical.

## **4.2 Code Validation**

Two different codes were used to generate power profiles to validate the ability of the inverse kinetics code to calculate the corresponding reactivity. The reactivity profiles corresponding to the computer-generated power profiles were known, which allowed them to be compared to the results of the inverse kinetics code. In addition, the computer-generated power profiles used the same initial condition, delayed neutron data, and prompt neutron lifetime as used in the inverse kinetics code. This eliminated the possibility of differences between the true and calculated reactivity profiles due to discrepancies in these values.

#### 4.2.1 Point Kinetics Code

To test and explore the behavior of the inverse kinetics code, a code was written in Fortran 95 to solve the point kinetics equations given by Eq. (2.31) and Eq. (2.32) without a source. The code used the Euler Method, as shown in equations (4.6) and (4.7), to solve for the power profile corresponding to a specified reactivity profile,  $\rho_j$ .

$$P_{j+1} = \left[ \frac{\rho_j - \beta}{l(1 - \rho_j)} P_j + \sum_{i=1} \lambda_i C_{i,j} \right] (t_{j+1} - t_j) + P_j \quad (4.6)$$

$$C_{i,j+1} = \frac{\beta_i}{l(1 - \rho_j)} P_j - \lambda_i C_{i,j} \quad (4.7)$$

Where  $j$  is the index location within the array,  $i$  is the precursor group number, and reactivity is expressed as a decimal rather than in units of dollars.

The purpose of this code was not to exactly simulate a pulse from the ACRR, but rather to produce a general pulse power profile for which the reactivity was known. The reactivity was specified such that it changed according to the following sequence:

1. \$0 for a period of time to give constant power before the pulse.
2. Linearly increased up to a specified value.
3. Decreased at a rate proportional to the change in energy released to simulate negative temperature feedback.
4. Decreased linearly to represent all the rods being dropped in to the reactor to shut it down.
5. Held constant at a negative value.

The negative temperature feedback was specified so that the reactivity dropped at a rate proportional to the change in energy such that the reactivity would equal \$1 when the pulse had released half of its specified energy. The point at which the reactivity reaches \$1 on its way down after a pulse, always corresponds to the point at which the power reaches its peak value [Hetrick, 1971]. By requiring that half of the energy be released by this point, a uniform pulse shape could be achieved. A pulse power profile generated using the kinetics code and the corresponding true reactivity and the reactivity calculated using the inverse kinetics code are shown in Figure 4.2.

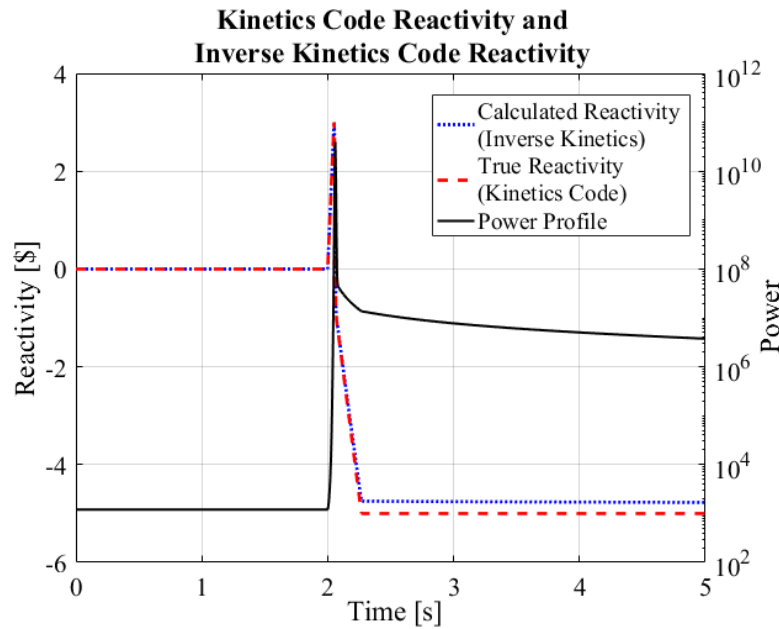


Figure 4.2: Plot showing the reactivity calculated using the inverse kinetics equation compared to the true reactivity. As can be seen, the actual reactivity is closely obtained; however, the inverse kinetics reactivity begins to deviate from the true reactivity as the negative reactivity is linearly inserted. A time step of 10  $\mu$ s was used.

The profiles shown in Figure 4.2 are the same ones used in Section 3.2 to study the inverse kinetics equation. As pointed out in Section 3.2, the calculated and true reactivity values agree very closely up until the point at which the negative reactivity is inserted at a

linear rate. At this point the reactivity profiles begin to diverge. The discrepancy is thought to be due to numerical errors from the point kinetics code. As will be seen in the next section, this type of discrepancy does not occur when applying the inverse kinetics code to a power profile generated using Razorback. This gives reason to believe that the cause of the discrepancy is due to the power profile outputted by the point kinetics code not being representative of the inputted reactivity. Future work could be done to pinpoint the cause of this behavior; however, it is of little concern as the code was successfully validated using Razorback.

#### **4.2.2 Razorback Comparison**

Razorback is a computer code developed by Darren Talley of Sandia National Laboratories to simulate the operation of the ACRR, and it has been shown to agree well with actual ACRR operations [Talley, 2017]. To test the functionality of the inverse kinetics code, an ACRR pulse was simulated using Razorback and the power profile data from the pulse was inputted into the inverse kinetics code. The resulting calculated reactivity was then compared to the true reactivity provided by Razorback. Figure 4.3 shows the power profile used, along with the calculated and true reactivity. As can be seen, the inverse kinetics reactivity agrees very well with the Razorback reactivity, and the error between the two was found to decrease when using finer time steps, as is expected.

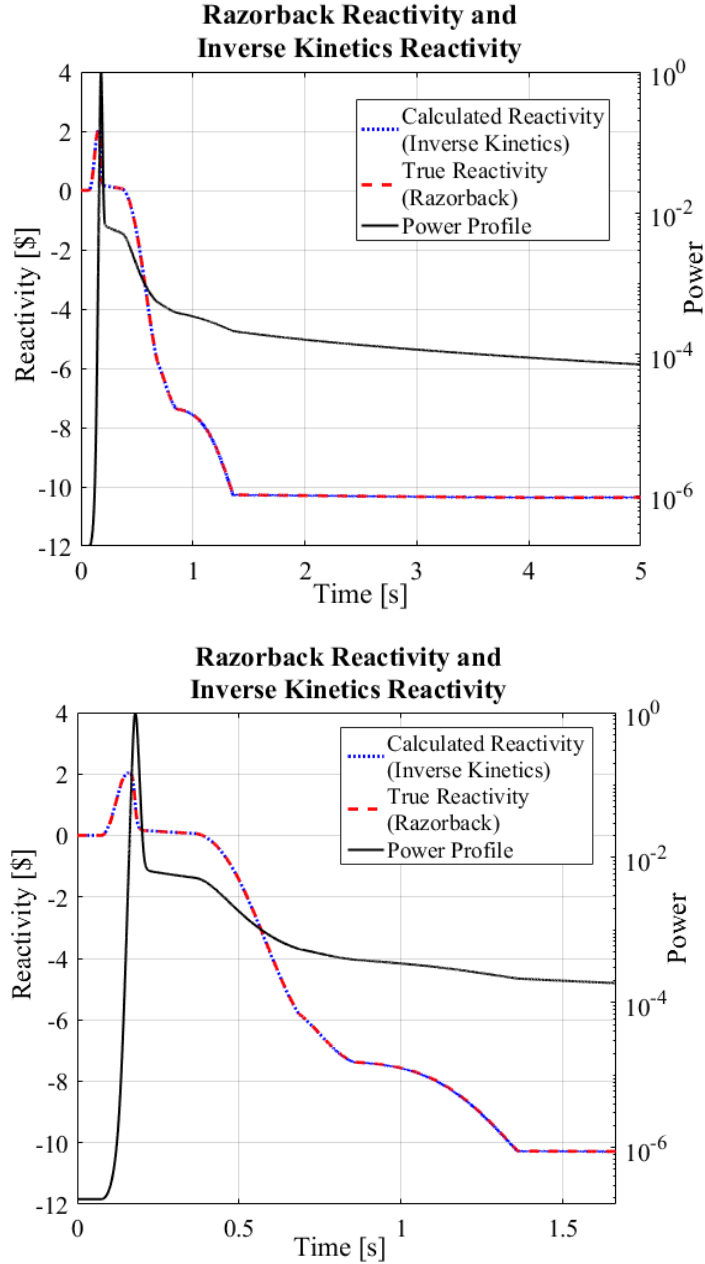


Figure 4.3: Using a power profile from Razorback, good agreement was found between the calculated reactivity and the Razorback reactivity.

In this section, it has been shown that the inverse kinetics code can accurately calculate the reactivity corresponding to a computer-generated power profile, assuming a small enough time step and proper constants and initial condition are used. It is important to remember that the power data inputted to the inverse kinetics code must be proportional to the power. This is

easy to achieve using computer calculated power profiles; however, capturing experimental data that is truly proportional to the power is difficult, especially when the reactor power level is low. In Chapter 5, the gathering and processing of experimental power profiles from the ACRR will be discussed, and in Chapter 6 the inverse kinetics code will be applied to the experimental data.

## **5. Experimental Data Collection and Preparation**

To experimentally measure the power profiles, a photoconductive detector (PCD) was used. The PCD has a fast response time that allows it to capture the shape of the pulse, and it is also sensitive enough to produce a measurable signal many hours after a pulse. For comparison purposes, a self-powered neutron detector (SPND) was also used to capture the shape of the pulse; however, due to its low sensitivity, it could not be used for analysis long after the pulse. To record the pulse data from the detectors, a Yokogawa high speed data acquisition oscilloscope was used. The PCD signal was passed through a logarithmic amplifier before going in to the oscilloscope, which allowed the large range of signal strengths experienced between the peak of the pulse to many hours after the pulse, to be captured within the resolution of the oscilloscope. In addition, the PCD signal was recorded using two different sampling intervals that used a fine time step for a few seconds around the time of the pulse and a coarser time step before and after the pulse. By using the two sampling intervals, the details of the pulse shape could be captured, and the slower changing behavior following the pulse could be recorded for hours without generating prohibitively large amounts of data. Because the SPND was just used to capture the pulse, only a fine sampling interval was used for it, and it was passed through a linear amplifier. To process the PCD data into a suitable power profile for input to the inverse kinetics code required smoothing the data, linearizing it, and merging the long and short sampling interval signals. It was found that the PCD signal following the pulse became dominated by gammas from activation and fission product decay, which distorted its proportionality away from that of the true reactor power. This prevented the correct reactivity from being calculated following the pulse, so attempts were made to identify and



subtract off the unwanted contribution to the signal. The detectors used to measure the pulse, and the process of preparing the data will be discussed in this chapter.

## **5.1 Detectors Used**

### **5.1.1 Photoconductive Detector (PCD)**

A photoconductive detector consists of a sample of semiconducting material fitted with two ohmic contacts at opposite surfaces [Knoll, 2010]. The PCDs used at the ACRR, as shown in Figure 5.1, have a diamond semiconductor that is usually about 1 x 1 x 1 mm in size, with ohmic contacts made primarily of gold. A 750 V bias is applied across the semiconductor that establishes an equilibrium current, and when exposed to ionizing radiation, excess charge carriers are created in the diamond, resulting in a current in excess of the equilibrium current. This current is then passed through a logarithmic amplifier to convert it in to a logarithmic voltage signal, which allows many orders of magnitude of variations in the current to be captured within the resolution of the oscilloscope.

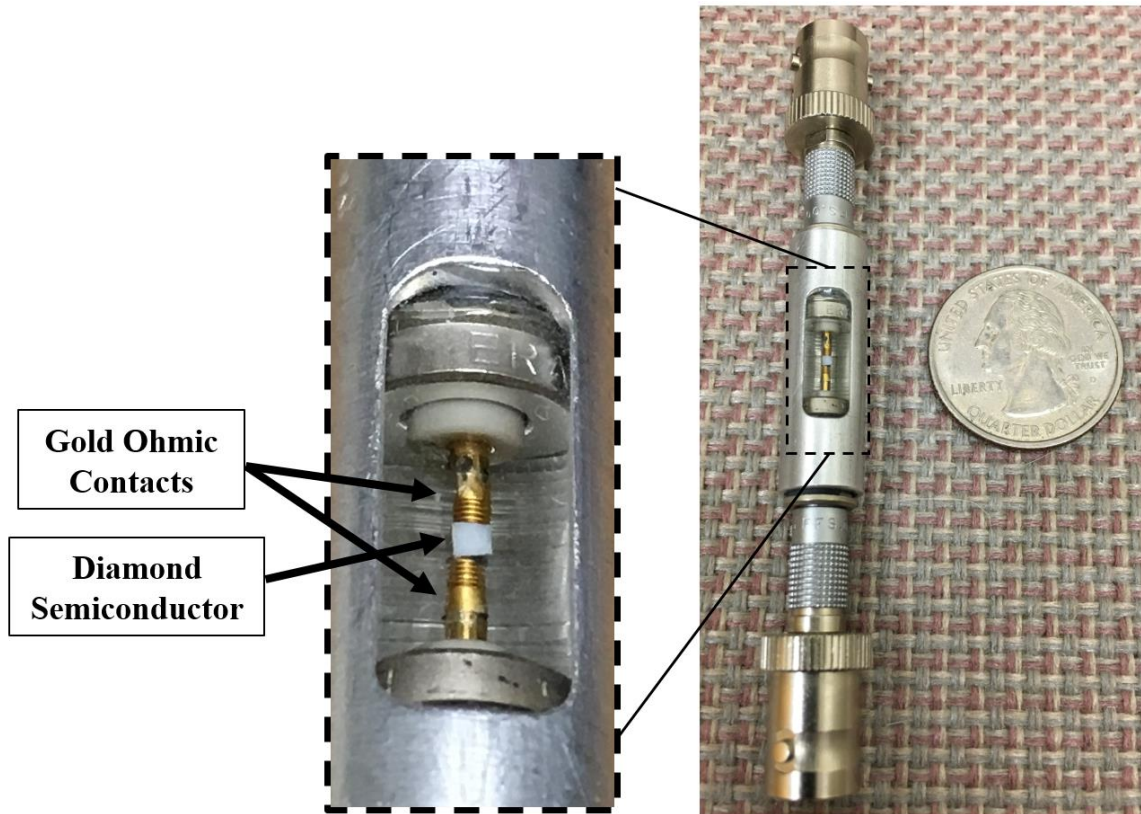


Figure 5.1: Cutaway of a PCD showing the 1 x 1 x 1 mm diamond semiconductor between the two gold ohmic contacts.

The PCD is sensitive to both neutrons and gamma rays. Table 5.1 shows the average ionizing radiation dose in carbon per fission in the central cavity of the ACRR. As can be seen, both the neutron and gamma dose are reduced when the lead-boron (LB44) bucket is in the central cavity; however, the ratio of neutron dose to gamma dose increases compared to free-field (FF), which is what the bucket is designed to do. For the PCD signal to be proportional to the power of the reactor, the ionizing dose seen by the diamond semiconductor must be proportional to the neutron ionizing dose, which is proportional to the reactor power. Because the PCD is also sensitive to gammas, this would require that the ratio of neutron to gamma dose remain constant with time for the signal to be proportional to the power. During the constant power period before the pulse and during a pulse, prompt gammas and neutrons

dominate (which have a constant ratio), and the neutron to gamma dose ratio remains pretty much constant. However, following the pulse, delayed fission product gammas and activation gammas begin to dominate the ionizing dose deposited in the diamond. Because the activation and delayed gammas decay at different rates than the neutron population, the ratio between neutron dose and gamma ionizing dose does not remain constant, and the PCD signal diverges from its proportionality to the power. For this reason, when using an unaltered PCD signal, the reactivity cannot accurately be calculated following the pulse. However, if the contribution from delayed fission product and activation gammas can be subtracted from the PCD signal, the reactivity following the pulse can be calculated. Attempts to do this will be discussed later in this chapter.

Table 5.1: Average ionizing dose deposited in carbon (diamond) per fission, in the central cavity of the ACRR. [Parma et al., 2015] and [Parma et al., 2013]

	FF rad[c]/fission	LB44 rad[c]/fission
Neutron Ionizing Dose in Carbon	7.41E-14	5.49E-14
Prompt Gamma Ionizing Dose in Carbon	2.32E-13	2.89E-14
Delayed Gamma Ionizing Dose in Carbon	1.01E-13	1.20E-14

The PCD's gamma response "deviates from the free-field carbon kerma at low energy due to photon attenuation by the PCD packing materials and at high energy due to the lack of sufficient equilibration for very energetic photons" [Griffin et al., 2004]. The PCD's neutron energy-dependent response is not known "due to a lack of good monoenergetic neutron reference fields" [Griffin et al., 2004]. Changes in the PCD response were modeled as being due only to the changes in the amounts of neutrons and gammas, rather than also including the

spectral dependence. Changes in the PCD's response due to other factors, such as temperature and rate dependence, were also assumed to be negligible. These effects are believed to be dominated by the loss of proportionality during the tail of the pulse.

Despite difficulties in using the PCD to measure the reactor power following a pulse, it does a good job of capturing the power profile during the pulse, and it does provide other beneficial qualities. The diamond semiconductor has a short charge carrier lifetime that gives the PCD a response time of less than one nanosecond. In addition, by exposing the diamonds in the PCDs to  $10^{16}$ - $10^{17}$  n/cm<sup>2</sup> they can be pre-damaged so that the PCD's response will not degrade with multiple reactor exposures [Griffin et al., 2004]. Also, the relatively small size of the PCD is beneficial, because it allows it to be collocated with experiments in the central cavity of the ACRR, as it will only minimally perturb the radiation field. This allows the time dependent dose received by the experiment to be more accurately captured.

### **5.1.2 Self-Powered Neutron Detector (SPND)**

A self-powered neutron detector consists of a wire surrounded by a sheath with an insulating material between them. The wire is made of a material with a high neutron capture cross section that leads to subsequent beta or gamma decay. The beta or gamma decay of the wire material results in the emission of electrons, which leave the wire and ideally are collected by the sheath. The resulting current that flows between the wire and the sheath is proportional to the neutron flux incident on the wire, and hence is proportional to the reactor power.

In the case of the ACRR, the wire is made of cadmium, which has a large cross section for thermal neutrons. When cadmium captures a neutron it promptly emits a gamma ray. The prompt emission of the gamma gives the detector a fast response; however, by relying on the gamma to create a secondary electron, the detector has less sensitivity as opposed to using a

wire material that uses direct beta decay to create the signal. Because of the low sensitivity of the SPNDs used at the ACRR, they are tens of centimeters long, which makes them too large to be placed in the central cavity, so instead they are placed around the outside of the core. Even with the large size of the SPNDs, their sensitivity is low and they are only able to capture a signal above noise during the time of the pulse.

Figure 5.2 shows the normalized signals from a SPND and a PCD obtained during an ACRR pulse. The main takeaway from the comparison of the signals is that the SPNDs sensitivity is too low to resolve the power of the reactor following the pulse. This is evident by the plateauing of the signal about 0.5 s after the pulse; whereas, the PCD signal continues to decrease. Despite the PCD signal not being proportional to the power following the pulse, it still provides a time dependent response that can be used to try to extract the true power profile. For this reason, the PCD was chosen to be used to attempt to experimentally calculate the late time reactivity behavior of the ACRR.

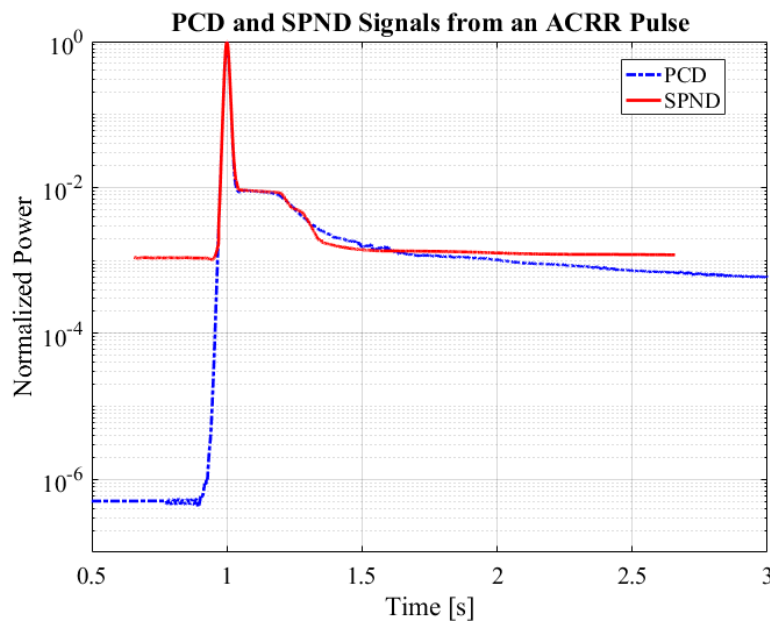


Figure 5.2: Comparison of a PCD and SPND signal from an ACRR pulse. The SPND signal quickly goes flat following the pulse because of its low sensitivity.

## 5.2 Experimental Data Preparation

Before the raw detector data from the Yokogawa oscilloscopes could be inputted to the inverse kinetics code, some preparation was required, which was performed in MATLAB. To reduce the noise of the signals, the PCD and SPND data was smoothed using Savitzky-Golay filtering. After smoothing, no further preparation was needed for the SPND because it was linearly amplified and only used around the time of the pulse. However, as the PCD data was logarithmically amplified and gathered using a “short” and a “long” sampling interval, it required linearizing and merging of the two sampling intervals. In addition, attempts were made to subtract activation and fission product gammas from the PCD signal. To explain the process used to prepare the data, experimental PCD data from a 56 MJ free-field pulse will be used as an example.

### 5.2.1 Smoothing

The ACRR is an electrically noisy environment as can be seen by the unsmoothed PCD signals in Figure 5.3. To smooth the raw data, Savitzky-Golay filtering was used by using the MATLAB built in function *sgolayfilt*. This type of filtering works by performing a least-squares fit of a polynomial to a window of a specified number of points. The fitted polynomial is then used to calculate the smoothed data point at the center of the window, and the process is repeated for all data points. To smooth the PCD and SPND data, different window sizes and polynomial orders were used depending on what region of the pulse was being smoothed. In general, first-order polynomials with larger time windows were used for smoothing before and after the pulse, and third-order polynomials with smaller time windows were used for smoothing during the pulse.

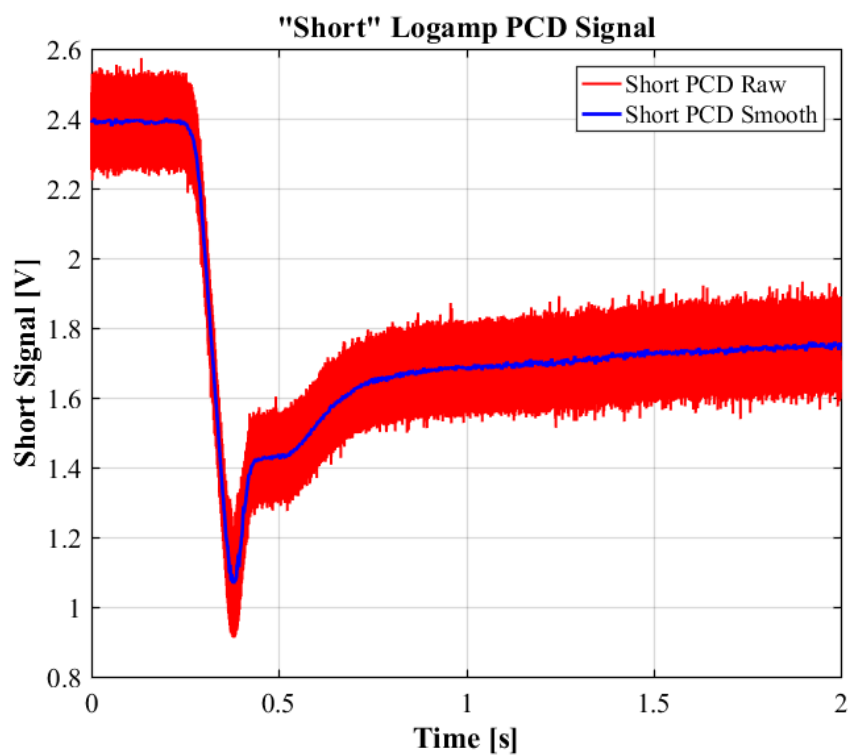
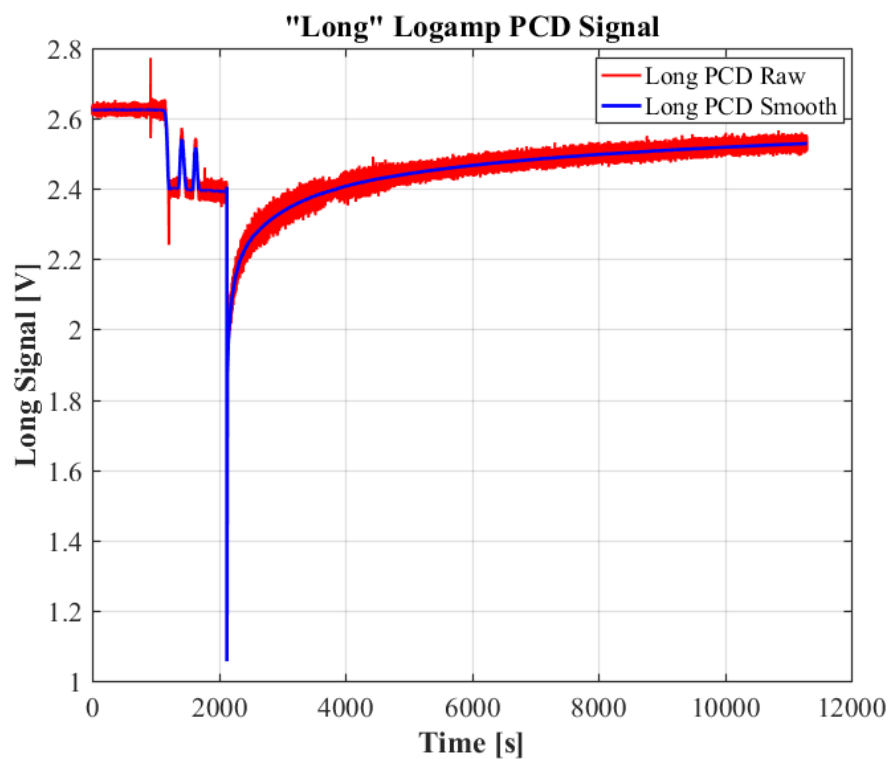


Figure 5.3: Plots showing the raw log-amp PCD signals, before and after smoothing. The signals are inverted as a byproduct of the log-amp.

The long and the short signals were gathered from the same PCD; however, the signal was split and recorded on separate oscilloscopes with different sampling intervals. In this example, a sampling time of 0.02 s was used for the long data and 10  $\mu$ s was used for the short data. The short signals are typically only gathered for 2 s around the time of the pulse so that the rapid changes in power during this time can be resolved.

### **5.2.2 Linearizing**

As can be seen in Figure 5.3, by passing the PCD signal through the logarithmic amplifier, the variation in power from 0 W to about  $1.5 \times 10^9$  W in this case, was able to be captured within a range of a couple volts on the oscilloscope. As a byproduct of the log-amp, the signals are also inverted. To linearize and properly invert the signal, predetermined conversion data is used. The conversion data provides the linear current corresponding to discrete logarithmic voltage values. By interpolating the conversion data, the linear equivalence of each of the logarithmic data points can be found, and the linear signals as shown in Figure 5.4 are obtained. The linear signals are shown with a linear y-axis scale so that the size of the pulse relative to the power before and after the pulse can be visualized. After linearizing the data, the long signal was shifted so that the portion of the signal before the reactor was turned on would correspond to zero power. The short signal was also shifted by the same amount. Properly zeroing the signal is not necessary for calculating the reactivity as the inverse kinetics equation is only concerned with the relative changes in power; however, it is important when attempting to subtract off the activation and fission product gammas.



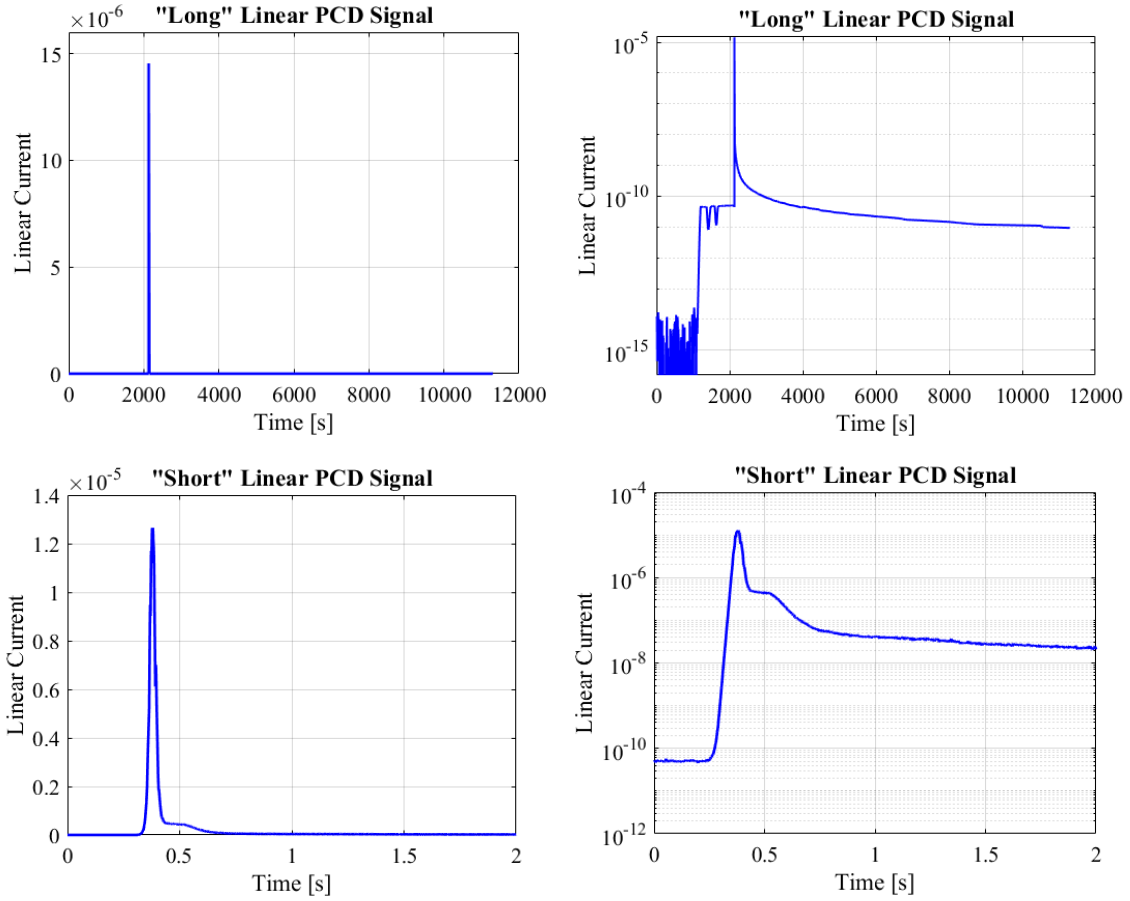


Figure 5.4: The short and long linear PCD signals, shown with linear and logarithmic y-axis scales.

### 5.2.3 Merging

The final step of preparing the PCD power profile is to merge the short and the long signals. This was done by overlaying the two signals and replacing the long data with the short data within a specified window. Before overlaying the signals, they were both normalized to their value 0.3s before the peak of the pulse. This point was chosen because both signals were flat at that time, and points during or immediately after the pulse could not reliably be used because they were often not accurately captured due to large time step of the long signal and the rapidly changing power. Figure 5.5 shows the overlaid normalized profiles.

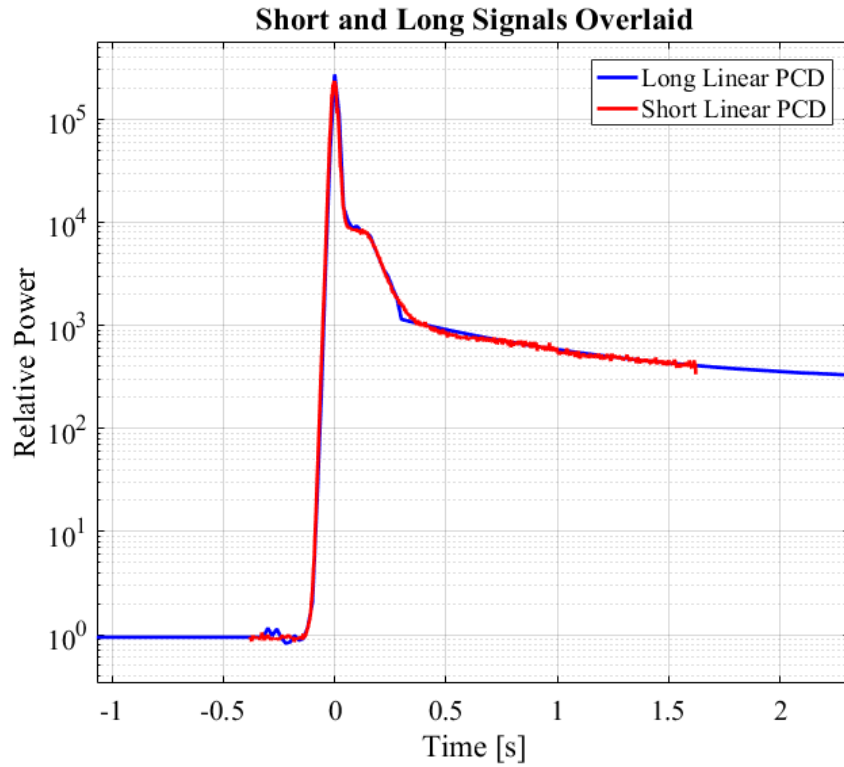


Figure 5.5: Plot showing the overlap of the short and the long PCD signals. The smaller sampling interval of the short signal provides greater resolution of the pulse.

After merging the short and the long data, the PCD profile was clipped 1 s before the peak of the pulse. This was done because the reactor was at constant power at that point, and the constant power initial condition assumed in the inverse kinetics code was applicable. Figure 5.6 shows the processed PCD signal, normalized to the peak value, before attempting to subtract the delayed fission and activation gammas from it. The flat region before the pulse shows the reactor at constant power (about 1500 W), the transient rods are then quickly ejected from the core making the reactor prompt supercritical, causing the power to quickly rise to about 1.5 billion watts in this case, and then negative reactivity feedback turns the pulse around causing the power to decrease. The safety, control, and transient rods are then dropped into the

core further decreasing the power and creating the knee in the power profile, and finally the power decreases away according to the delayed neutrons.

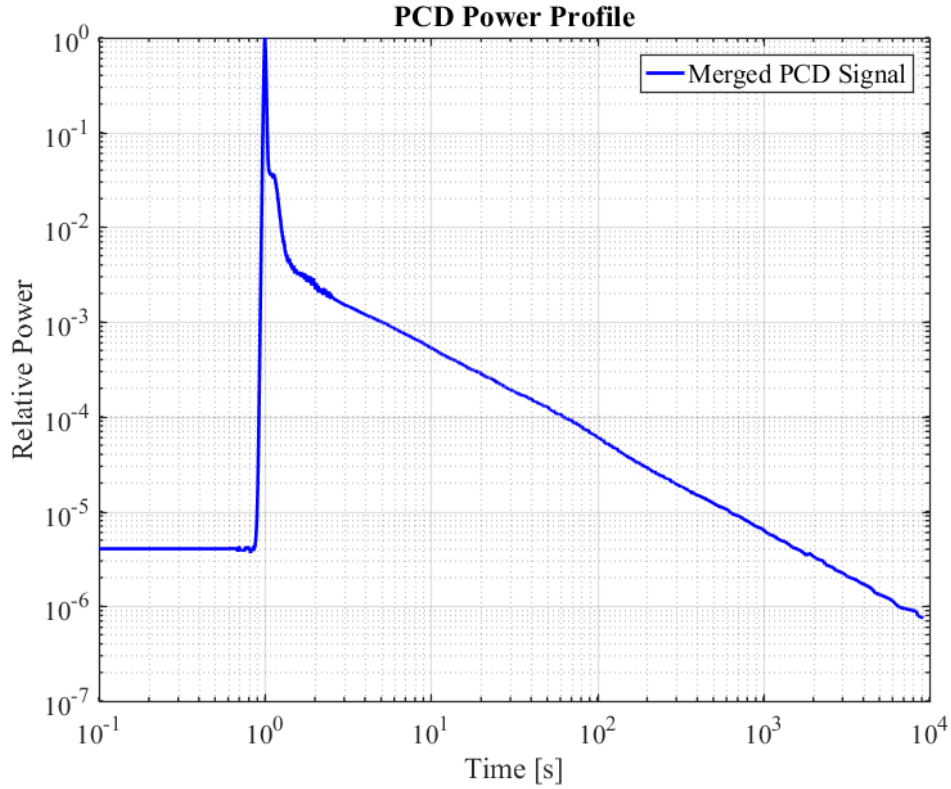


Figure 5.6: Processed PCD profile from a 56 MJ FF pulse, ready for input into the inverse kinetics code.

### 5.3 Activation and Fission Product Gamma Ray Subtraction

When applying the inverse kinetics code to the power profile from Figure 5.6, the reactivity profile shown in Figure 5.7 is obtained. It was known from MCNP and Razorback calculations that the reactivity following the pulse should drop to and remain at about  $-\$10$  for free-field pulses. However, as can be seen, the reactivity only drops to about  $-\$2$  and then approaches  $\$0$ . After seeing similar behavior with PCD profiles from multiple different pulses, and after ruling out that the behavior could be caused by not accounting for a source term, the

behavior was attributed to activation and fission product gammas dominating the signal following the pulse.

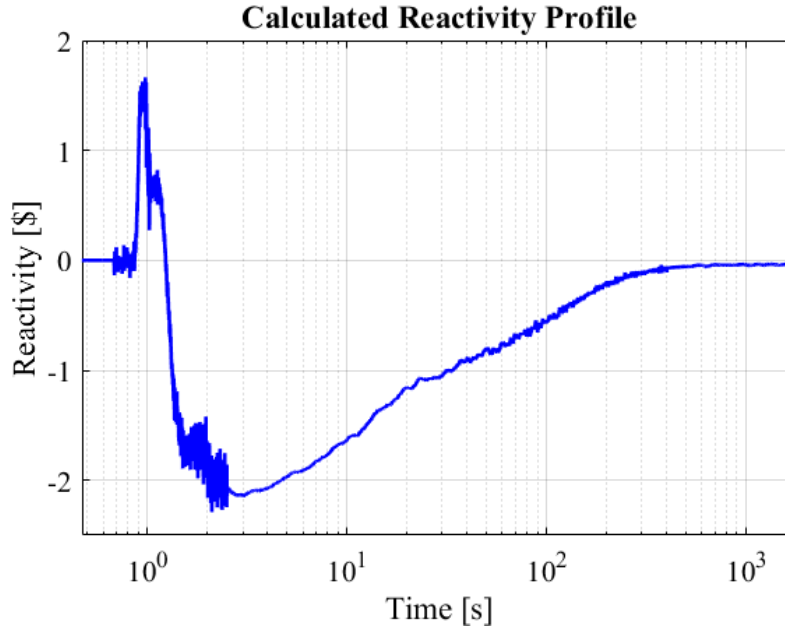


Figure 5.7: Reactivity profile corresponding to the PCD power profile in Figure 5.6, calculated using the inverse kinetics code. The reactivity is correct before and during the pulse, but following the pulse it does not drop to and remain at the expected value of about  $-\$10$ .

As mentioned earlier, the PCD signal will be proportional to the power of the reactor when the ratio of neutron to gamma ionizing dose in the diamond is constant. This condition is met when the reactor's power is sufficiently high, such that activation and delayed fission product gammas do not dominate. During the constant power region before the pulse, prompt neutrons and gammas dominate the PCD signal, and their ratio is constant, and as a result the correct reactivity of  $\$0$  is calculated. During the pulse, prompt neutrons and gammas still dominate, and even though their concentration is changing their ratio still remains constant, and as a result, the calculated peak reactivity agrees with the reactor diagnostics, both of which are about  $\$1.5$  for this example. However, after the pulse as the power drops, the prompt

neutron and gamma dose will be overcome by the dose from delayed neutrons, delayed fission product gammas, and activation gammas. Because these three sources of ionizing radiation decay at different rates, the signal does not remain proportional to the delayed neutron dose, which is proportional to the power. In addition, it was uncertain what fraction of the signal following the pulse was due to delayed neutrons, but it was obvious that they did not dominate due to the incorrect behavior seen in the calculated reactivity profile.

Two different techniques were used to try to better understand the activation and delayed fission product gamma contribution to the PCD signal. These techniques were then used to try to subtract off the unwanted contribution to improve the signal's proportionality to the true reactor power profile, and hence improving the accuracy of the calculated reactivity profile. One of the methods used a U-235 fission product decay curve and an aluminum activation decay curve, which were iteratively convoluted with the PCD profile in an attempt to identify the contribution to the signal due to those sources. The contribution curve that was obtained was then subtracted from the PCD signal, and the resulting power profile and calculated reactivity profile were compared to Razorback. The other technique, used the difference between the PCD signal and a Razorback power profile to identify the half-lives and relative abundances of potential contributors to the deviation of the PCD profile from the Razorback profile. These identified sources were then compared with those identified from other pulses to see if there was consistency. Using the identified half-lives and abundances, decay curves were created, which were iteratively convoluted with PCD signals and subtracted, and the resulting power profile and calculated reactivity profile were compared to Razorback.

### **5.3.1 U-235 Fission Product and Activated Aluminum Subtraction**

This technique assumed that the gammas from U-235 fission products and activated aluminum and its impurities, were the primary cause of the PCD's deviation from the true power following the pulse. As mentioned in Chapter 2, the majority of the fissions that occur in the ACRR, are thermal fissions of U-235. For this reason, U-235 thermal fission product decay data, generated by Lane and Parma [2015] using CINDER2008, was used to give the shape of the ACRR fission gamma ray decay curve. CINDER2008 is a “transmutation code developed at Los Alamos National Laboratory, to model time and energy dependent photon characteristics due to fission” [Lane & Parma, 2015]. To attempt to account for the contributions from activation gammas, it was assumed that 6061-T6 aluminum was a major contributor, because the PCD body and fixture, along with some reactor structural materials, were all made of this type of aluminum. In addition, many other sources of activation gammas, such as those from steel, exist in the core following a pulse; however for simplicity, only aluminum was accounted for. Unlike the fission product gammas, a gamma decay curve was not available for 6061-T6 aluminum. For this reason, one was approximated. This was done by summing the decay curves of each of the isotopes that would activate within 6061-T6 aluminum, and weighting each one by the isotopic abundance, thermal neutron cross section, and gamma decay fraction. Table 5.2, shows the data used to create the activated 6061-T6 aluminum decay curve, and Figure 5.8, shows the normalized fission product and activated aluminum decay curves.

Table 5.2: The data used to generate the 6061-T6 Al activation decay curve. The element weight percents were obtained from the ACRR MCNP model [Parma et al., 2015]. The decay and cross-section data was obtained from the National Nuclear Data Center (NNDC) [2017].

6061-T6 Al Isotopes of Interest	Al-27	Si-30	Mg- 26	Cu-63	Cu-65	Mn- 55	Fe-58	Ti-50	Cr-50	Cr-54	Zn-64	Zn-68	Zn-70	Ni-58	Ni-64
Element Weight %	96.7	0.8	1.1	0.3	0.3	0.13	0.56	0.07	0.2	0.2	0.1	0.1	0.1	0.04	0.04
Isotope Atom Fractions	9.83E -01	2.62E -04	1.11E -03	4.97E -03	2.22E -03	2.69E -03	3.32E -03	6.54E -05	1.70E -04	9.26E -05	1.19E -03	4.69E -04	1.55E -05	6.02E -04	8.19E -06
Thermal Cross Sections [barns]	2.34E -01	1.07E -01	3.83E -02	4.47E +00	2.15E +00	1.33E +01	1.30E +00	1.77E -01	1.55E +01	3.60E -01	7.60E -01	7.20E -02	8.10E -03	4.60E +00	1.60E +00
Gamma Decay Fraction of Activated Isotope*	1.00E +00	5.54E -04	1.00E +00	3.57E -01	9.50E -02	1.41E +00	1.00E +00	1.00E +00	9.91E -02	0.00E +00	5.57E -01	0.00E +00	3.88E -01	0.00E +00	4.38E -01
Final Weighted Values	7.82E -01	5.29E -08	1.45E -04	2.70E -02	1.54E -03	1.72E -01	1.47E -02	3.94E -05	8.91E -04	0.00E +00	1.72E -03	0.00E +00	1.67E -07	0.00E +00	1.96E -05
Half Life of Activation Product [s]	1.35E +02	9.44E +03	5.67E +02	4.57E +04	3.07E +02	9.28E +03	3.84E +06	3.46E +02	2.39E +06	2.10E +02	2.11E +07	3.38E +03	1.47E +02	2.40E +12	9.06E +03
Decay Constant [1/s]	5.15E -03	7.34E -05	1.22E -03	1.52E -05	2.26E -03	7.47E -05	1.80E -07	2.01E -03	2.90E -07	3.30E -03	3.29E -08	2.05E -04	4.72E -03	2.89E -13	7.65E -05

\* Only the dominant gamma rays were considered.

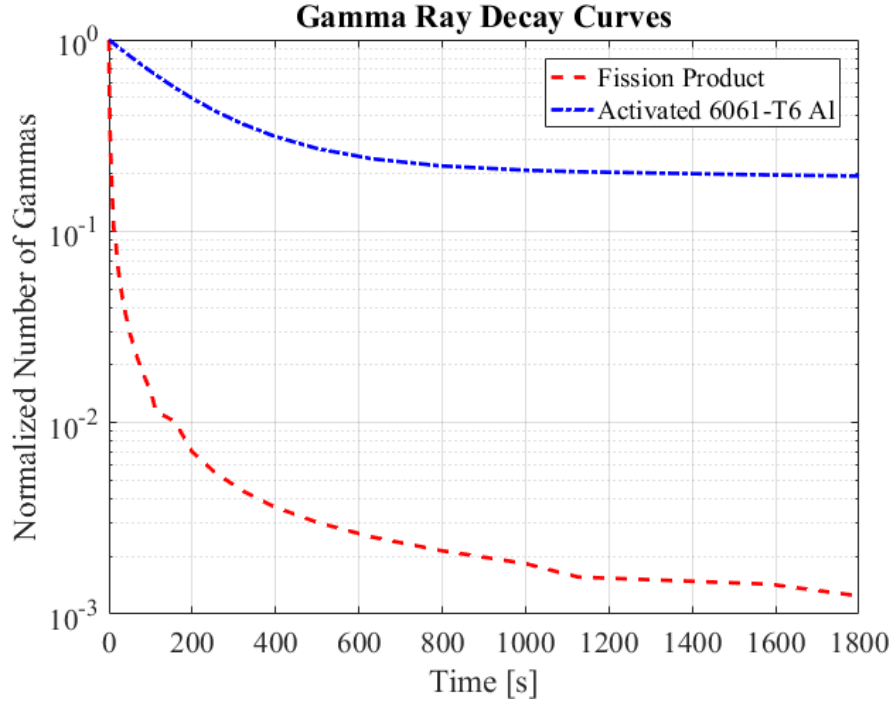


Figure 5.8: Delayed fission product and 6061-T6 aluminum activation, gamma decay curves. The aluminum decay is slower because of the longer-lived impurities, such as Mn-56. The relative contribution from these two sources to the PCD signal, is not known.

By appropriately scaling the decay curves in Figure 5.8, and iteratively convoluting them with the PCD signal, the contribution to the signal from fission products and activated aluminum, can theoretically be determined. However, the relative amount that each of these sources contribute to the PCD signal is not known as it depends on many factors, such as their abundances, location relative to the PCD, gamma-ray energies, and more. For this reason, the fractional contributions were parametrically varied from 100% fission product with 0% aluminum activation, to 0% fission product with 100% aluminum activation. The resulting PCD profile, with the convoluted contribution subtracted off, was then compared to a corresponding Razorback power profile, which allowed the fractions that gave the best agreement to the Razorback profile to be identified. It is important to note that because the PCD profile is not proportional to the power at all times, the decay curves could not be directly



convoluted with it as their production is proportional to the power. To account for this, the decay curves were iteratively convolved, first with the original PCD profile, and then with the subsequent updated PCD profiles, until convergence of the convolution profile was observed. The resulting convolution profile represents the contribution to PCD signal from the specified fission product and activated aluminum combination.

Before subtracting the convolution profile from the PCD, it had to be appropriately scaled. To do this, the percent difference between the PCD and Razorback profile at the end of the data was used. This difference between the two profiles was representative of the unwanted contribution to the PCD signal. By normalizing and overlaying the PCD and Razorback profiles, as shown in Figure 5.9, the difference between the two signals at 1800 s was found to be 99.78% of the PCD signal. It was assumed that all of this was due to fission product and activation gammas, so the convolution profile was scaled such that its value at 1800 s was equal to 99.78% of the PCD's value. This convolution profile was scaled such that when it is subtracted from the original PCD profile, the "corrected" PCD profile will have the same value as Razorback at 1800 s.

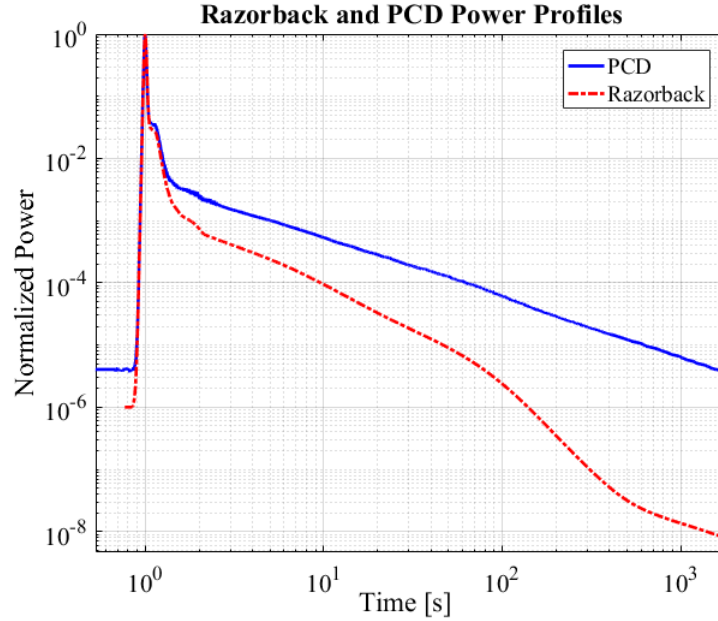


Figure 5.9: Experimentally measured PCD power profile compared to a corresponding computer-generated Razorback power profile. As expected the signals closely match during the pulse but the PCD diverges following the pulse.

Figure 5.10, shows the results of assuming three different ratios of the fission product and activated aluminum decay curves. “Total DG” is the percentage of the PCD signal at 1800 seconds that was assumed to be due to delayed gammas (fission product + activation), and in this case, it was determined by the percent difference between the PCD and Razorback profiles. “Fit” is the  $L^2$  norm of the difference between the “corrected” PCD and the Razorback profile, and it was used to quantify the agreement between the profiles, where a smaller number indicates better agreement. As can be seen, the scenario that gave the best agreement to Razorback, was when it was assumed that 100% of the delayed gammas, at 1800 s, were due to fission products. The other scenarios, in which aluminum activation gammas were assumed to contribute some percentage of the delayed gammas, gave poorer agreement. This suggests that the gammas from fission products are more prevalent than those from activated aluminum over this time range.

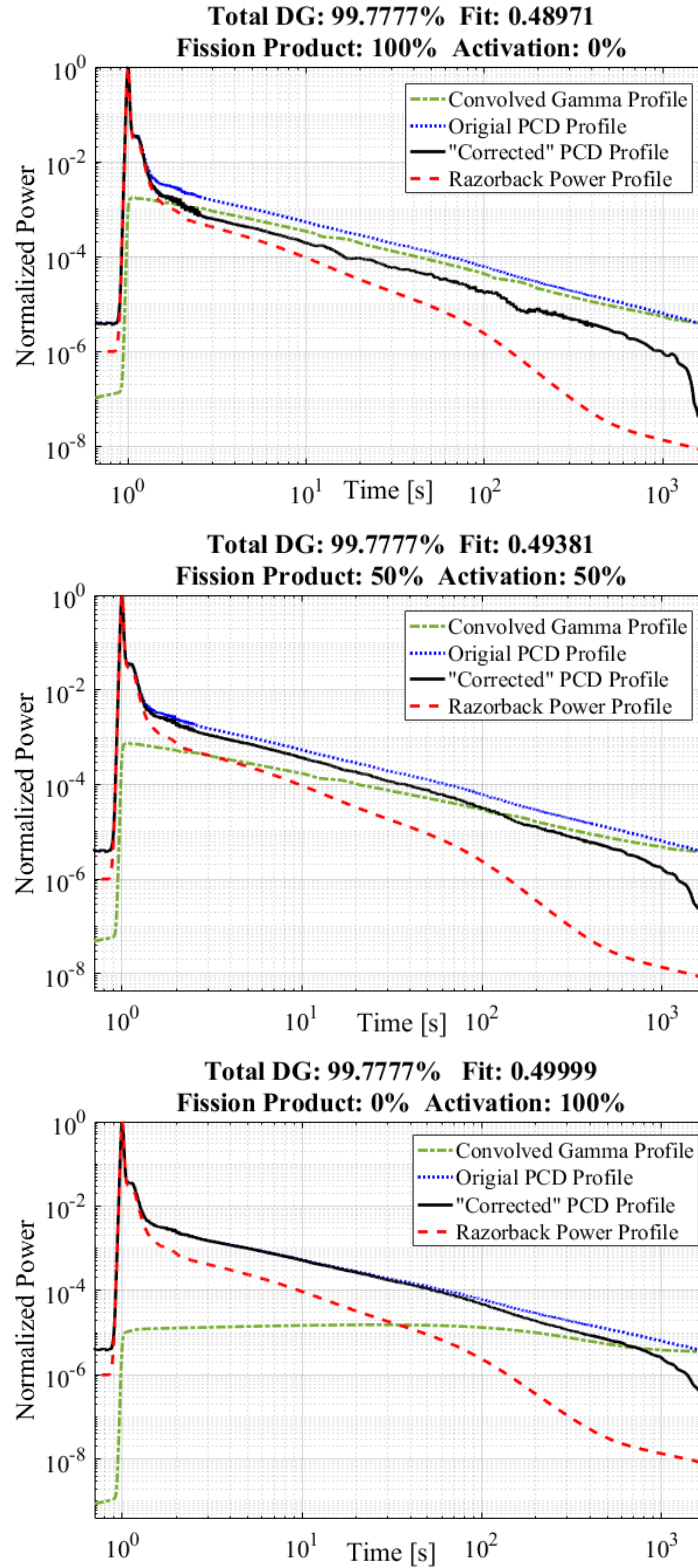


Figure 5.10: Three different combinations of the fission product and activated aluminum decay curves. Assuming the delayed gammas were due 100% to the fission products gave the best “corrected” PCD profile.

Using the best “corrected” PCD profile, the “corrected” reactivity profile in Figure 5.11 was obtained. Following the pulse, the “corrected” reactivity gives an improvement over the original reactivity. However, even though the corrected profile agrees better, it is still far from the expected reactivity, given by Razorback. This is thought to be due to the presence of other dominant gamma ray sources that were not accounted for in the decay curves from Figure 5.8. To try to better identify and account for these sources, a different approach was taken, as will be discussed in the next section.

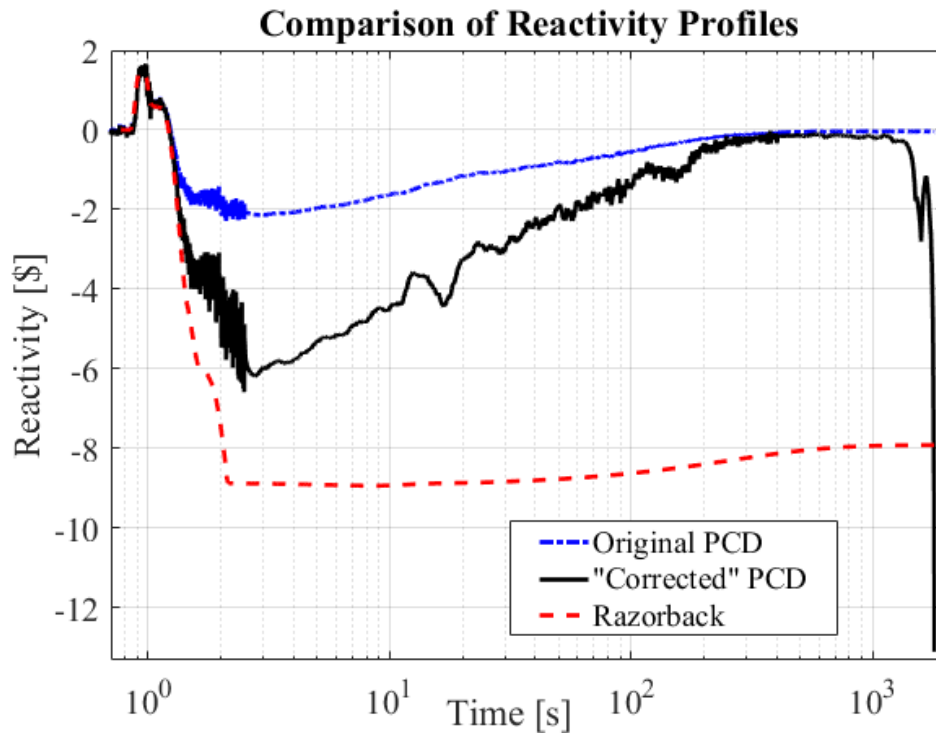


Figure 5.11: By subtracting off fission product gammas the calculated reactivity agreed better with Razorback; however, other sources still need to be accounted for.

### 5.3.2 Razorback and PCD Difference

In the previous section, the process of accounting for the unwanted contribution to the PCD signal using the U-235 fission product and activated 6061-T6 aluminum gamma decay

curves, was described. The plots in Figure 5.10 show how only limited agreement with Razorback can be achieved by only accounting for these two sources. The process described in this section utilizes the difference between the PCD signal and the Razorback power profile. By definition, the difference between the profiles following the pulse, is the unwanted contribution to the PCD signal. This difference could be directly subtracted from the PCD signal to exactly give the expected power profile, and hence the expected reactivity profile; however, doing this does not tell us anything about the unwanted contribution, and it assumes Razorback exactly represents the behavior of the reactor during the experiment. To better understand the unwanted contribution to the PCD signal, attempts were made to identify the relative abundances and half-lives of the sources that make up the difference profile. These sources were expected to be either individual fission products and activated isotopes, or groups of fission products and activated isotopes with similar half-lives. Using the determined half-lives and abundances, a decay curve was constructed which could be iteratively convoluted with the PCD signal and subtracted, as done in the previous section. By subtracting the convoluted profile, it was hoped that only the unwanted contribution could be subtracted, leaving behind the portion that is proportional to the reactor power. In the next chapter, the half-lives and relative abundance from different pulses will be compared.

The difference profiles used, were clipped so that they would begin at the tail of the pulse, which was when the PCD and Razorback profiles began to noticeably diverge, and at this point the production of activation and fission products were very low. Figure 5.12, shows the difference profile corresponding to the PCD and Razorback profiles that have been used throughout this chapter. As can be seen, the difference profile is responsible for the majority of the PCD's signal (99.78% at 1800 s).

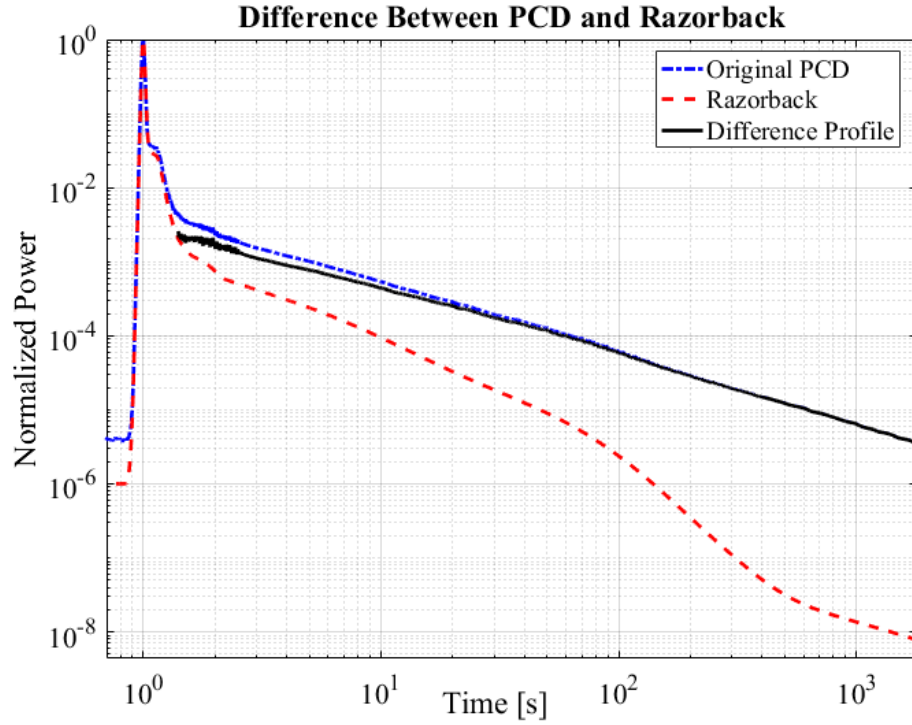


Figure 5.12: Plot showing the difference between the PCD and Razorback profiles during the tail of the 56 MJ FF pulse.

To identify the sources, the difference profile is plotted with a logarithmic y-axis, which allows the exponential decay of the longest-lived source to be identified as the linear portion at the end of the profile. This works because by taking the natural log of the radioactive decay equation, it can be expressed in the form of a linear polynomial as shown in Eq. (5.1).

$$N(t) = N_0 e^{-\lambda t} \xrightarrow{\text{natural log}} \ln(N(t)) = -\lambda t + \ln(N_0) \quad (5.1)$$

Where,  $\lambda$  is the decay constant, and  $N(t)$  is the relative amount of the source at time  $t$  (given by the difference profile), and  $N_0$  is the initial amount. By finding the slope of the linear region of the difference profile,  $\lambda$  can be obtained, from which the half-life can be calculated using Eq. (5.2).

$$t_{\frac{1}{2}} = \frac{\ln(2)}{\lambda} \quad (5.2)$$

To find the slope, two points within the linear region are visually chosen. A line is then fitted to these points, which gives the contribution from the source over the length of the difference profile. This contribution is then subtracted, revealing the linear region corresponding to the next longest-lived source, and the process is repeated until all distinct sources are subtracted. The y-intercepts of the sources are used to determine their relative abundances. Using this process, seven sources were identified using the difference profile in Figure 5.12. Figure 5.13 shows each of the seven linear regions that were identified, and Table 5.3 shows the corresponding relative abundances and half-lives.

Table 5.3: The seven identified sources from the 1800 s long difference profile from the 56 MJ free-field pulse.

	Decay Constant [s <sup>-1</sup> ]	Half-life [s]	Relative Abundance
Source A	6.43E-4	1078	0.005
Source B	3.99E-3	173.7	0.0138
Source C	1.64E-2	42.2	0.0617
Source D	5.01E-2	13.8	0.0943
Source E	1.67E-1	4.16	0.2956
Source F	7.18E-1	0.966	0.3528
Source G	1.59E+0	0.435	0.1768

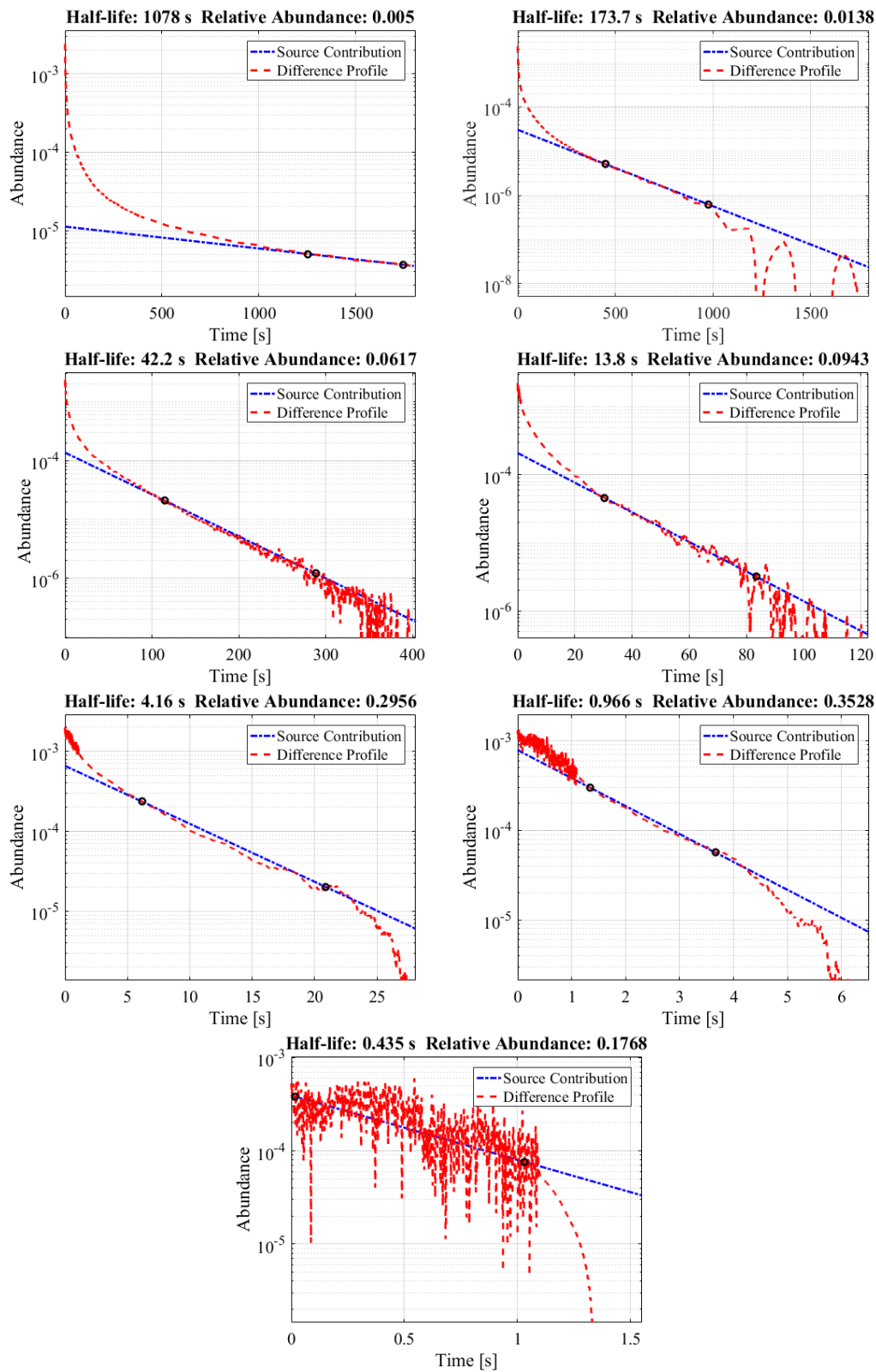


Figure 5.13: The seven linear regions that were identified using the difference profile from Figure 5.12. For each plot, the source contributions from all longer-lived sources were subtracted from the difference profile.



Using the half-life and relative abundance information obtained from the difference profile, the “7 Identified Sources” decay curve, shown in Figure 5.14, was created. This decay curve was then convoluted with the PCD profile, assuming that it was responsible for 99.78% of the PCD’s signal at 1800 s. The convoluted profile was then subtracted from the PCD signal, to obtain a “corrected” PCD profile, as shown in Figure 5.15.

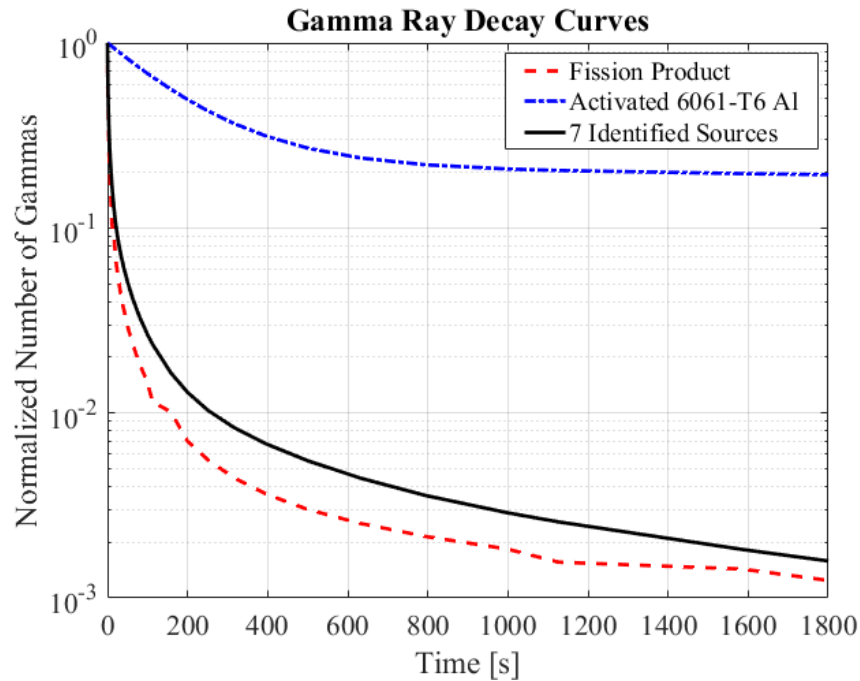


Figure 5.14: The decay curve created from the seven identified sources, compared with the activated aluminum and fission product decay curves.

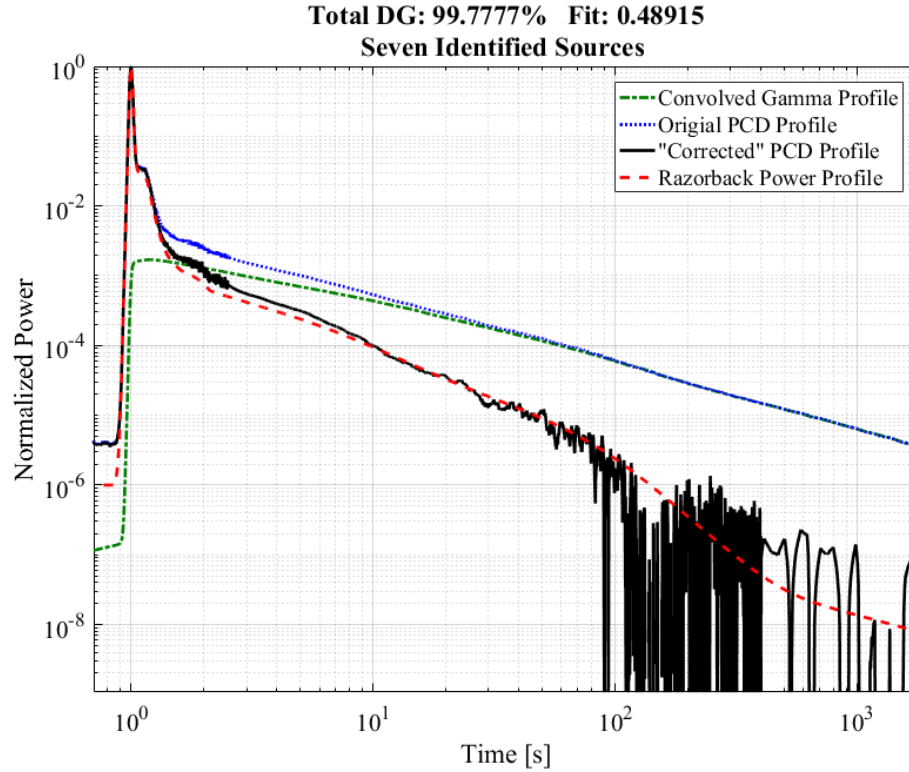


Figure 5.15: The results of convoluting the decay curve, created with the seven identified sources, with the original PCD signal. The corrected profile gives better agreement with Razorback than was achieved with the fission product and activated aluminum decay curves.

Using the decay curve created from the difference profile, it can be seen in Figure 5.15 that the “correct” PCD profile agrees better with Razorback than was achieved with the fission product and aluminum activation decay curves. However, the “corrected” profile begins to get very noisy around 90 s. This occurs because according to the convoluted gamma profile, the contribution due to the seven identified sources, is responsible for such a large fraction of the PCD signal that when it is subtracted only the noise of the PCD signal remains. This indicates that the portion of the PCD signal proportional to the reactor power after 90 s, is so small that it is difficult to resolve. This issue will be further explored in the next chapter to see if this same behavior is observed with data from other pulses. It is also important to note that errors

in calculating the half-lives and relative abundances of the decay curve, could be responsible for some of the discrepancies between the corrected profile and Razorback.

To reduce the noise of the “corrected” profile beyond 90 s, it can be assumed that the unwanted contribution to the PCD signal is smaller than 99.78% at 1800 s. However, by doing this the agreement with Razorback is reduced. For example, Figure 5.16 shows the results of assuming that delayed gammas are responsible for 97.5% of the PCD signal at 1800 s. As can be seen, the “corrected” profile isn’t nearly as noisy as in Figure 5.15; however, the agreement with Razorback is poorer. Figures 5.17 and 5.18 show the reactivity profiles corresponding to the “corrected” PCD profiles from Figures 5.15 and 5.16, respectively.

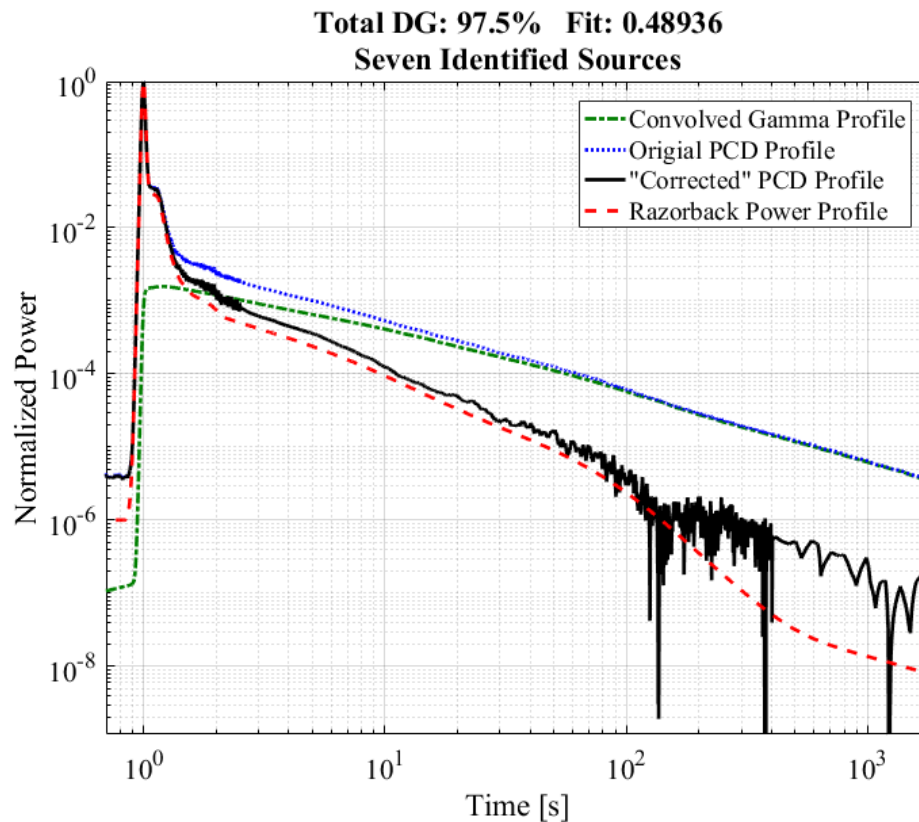


Figure 5.16: Assuming that the delayed gammas are only responsible for 97.5% of the signal at 1800 s rather than 99.78%. This reduces the noise in the “corrected” profile, but also gives it poorer agreement with Razorback.

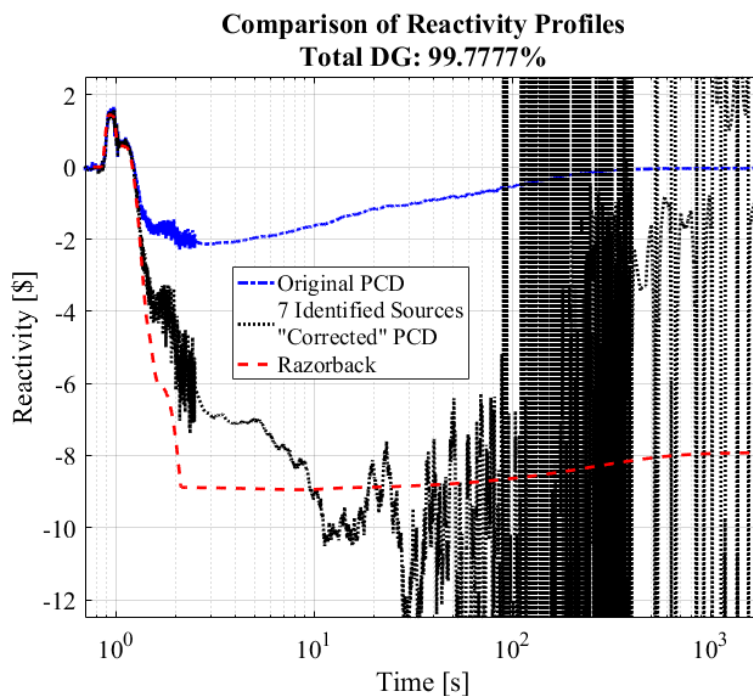


Figure 5.17: The reactivity profile shown here is the best that could be achieved using the methods described in this chapter. It most closely gives the expected shutdown reactivity.

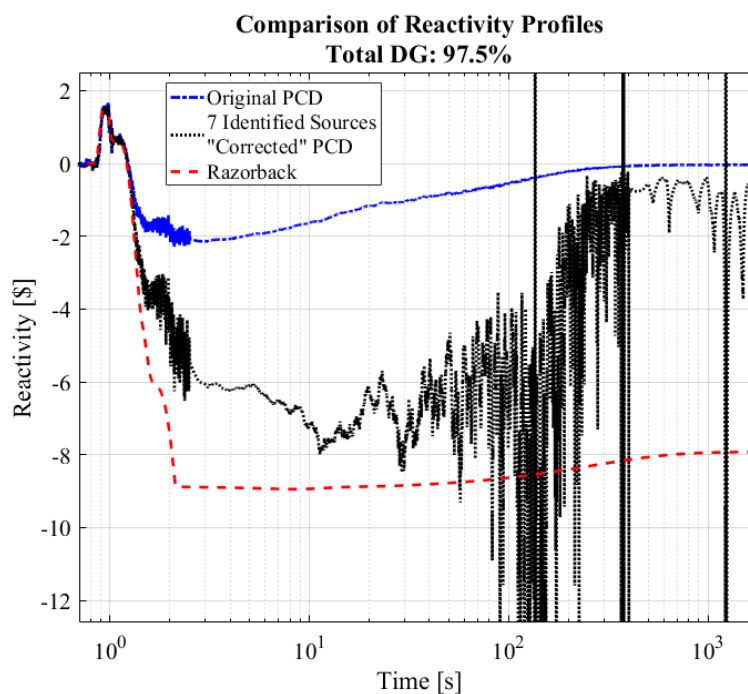


Figure 5.18: By assuming the delayed gammas contribute less than 99.78%, the reactivity doesn't drop quite as low as expected, but the noise is lower and it is still better than what was achieved with the fission product and activated aluminum decay curves.

As can be seen, the corrected reactivity in Figures 5.17 and 5.18, is much closer to what we would expect, than what was found in Figure 5.11. Specifically, in Figure 5.17, the corrected profile approaches the correct shutdown reactivity and doesn't begin returning to \$0; however, the reactivity beyond 90 s becomes undistinguishable. It is worth mentioning that the increase in Razorback reactivity following the pulse from about -\$9 to -\$8 is due to the reactor core cooling; whereas, the reason the original PCD reactivity returns to \$0 is due to the signal not dropping as fast as it should, which is interpreted by the inverse kinetics code as the reactor being just short of critical.

In this chapter, the process of gathering and preparing experimental power profile data was explained. Unfortunately, the PCD's sensitivity to gamma rays makes it difficult to extract the true reactor power from its signal. Because the true reactor power is what is needed for input into the inverse kinetics code, this also makes it difficult to accurately calculate the true reactivity. The PCD signal was found to be proportional to the true power before and during a pulse, but after the pulse this proportionality disappears due to the large number of activation and fission product gammas. Razorback was found to be a valuable tool for estimating the percentage of the signal that was believed to be due to delayed gammas, and it provided a way to help identify potential sources that could be responsible for the unwanted contribution to the PCD. The analysis done in this chapter utilized data from a 56 MJ free-field pulse. In the next chapter, data from pulses of different sizes and with the addition of the lead-boron bucket will be studied.

## **6. Results**

In the previous chapter, by comparing the PCD signal to a Razorback simulation of the pulse, sources were identified that described the difference between the profiles. By iteratively convoluting these sources with the PCD signal, their contribution could be determined and subtracted, ideally leaving behind the portion of the PCD signal that is proportional to the reactor power. This process seemed to be the most promising way, within the scope of this project, to extract the true power profile of the reactor. Future work could seek improved ways of experimentally measuring the power profile of the reactor.

The results of applying this method to PCD signals from four different pulses are described in this chapter. Two of the pulses were done with the free-field environment, and two were done with the lead-boron bucket in the central cavity. It was uncertain what effect the LB44 bucket would have on the proportionality of the PCD signal to the true power. Because of the lead, it was thought the delayed gamma fraction would be lower, but due to the boron, the thermal neutron contribution would also be lower. No improvement was seen with the signal from the LB44 bucket compared to FF; however, the half-lives of its identified sources were distinctly different than those of the FF sources. Using the inverse kinetics code, the corrected PCD profiles were used to calculate the reactivity, and the results were compared to Razorback.

### **6.1 Source Identification and Subtraction**

Razorback simulations were run for each of the four pulses, and the differences between the simulated profiles and the experimental PCD profiles were used to identify the unwanted sources in the same way as described in Section 5.3.2. For each pulse, 30 minutes' worth of data was considered, and the delayed gamma fraction at the end of the data was used

to scale the convolved gamma profile. Depending on the pulse, different numbers of sources were identified. This could be due to variations in how well the PCD signals were smoothed and how well the pulse was replicated using Razorback. Despite this, some similarities in half-lives were noticed, and they appeared to be dependent on whether the pulse was FF or with the LB44 bucket. The identified sources for each pulse will be discussed in Section 6.1.5.

#### **6.1.1 56 MJ Free-Field Pulse**

The 56 MJ FF pulse, was used for the examples throughout Chapter 5. The data from this pulse smoothed particularly well, and seven sources were identified. Figure 6.1 shows a comparison of the power profiles and the reactivity profiles. As can be seen, the corrected profile could not be resolved well beyond 90 s, because the convoluted gamma profile represented such a large percentage of the PCD signal that when it was subtracted only noise was left. Both the original and corrected reactivity profiles agree well with what the reactivity is expected to be during and before the pulse; however, the corrected reactivity does much better at predicting the shutdown reactivity, even though it takes longer to get there and is noisy.

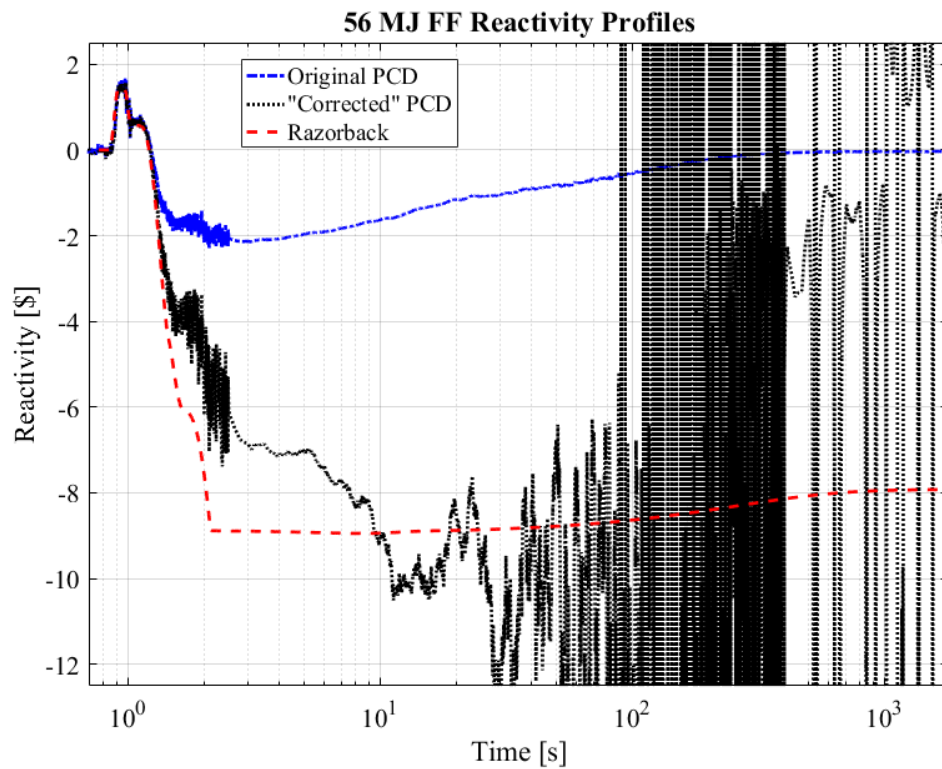
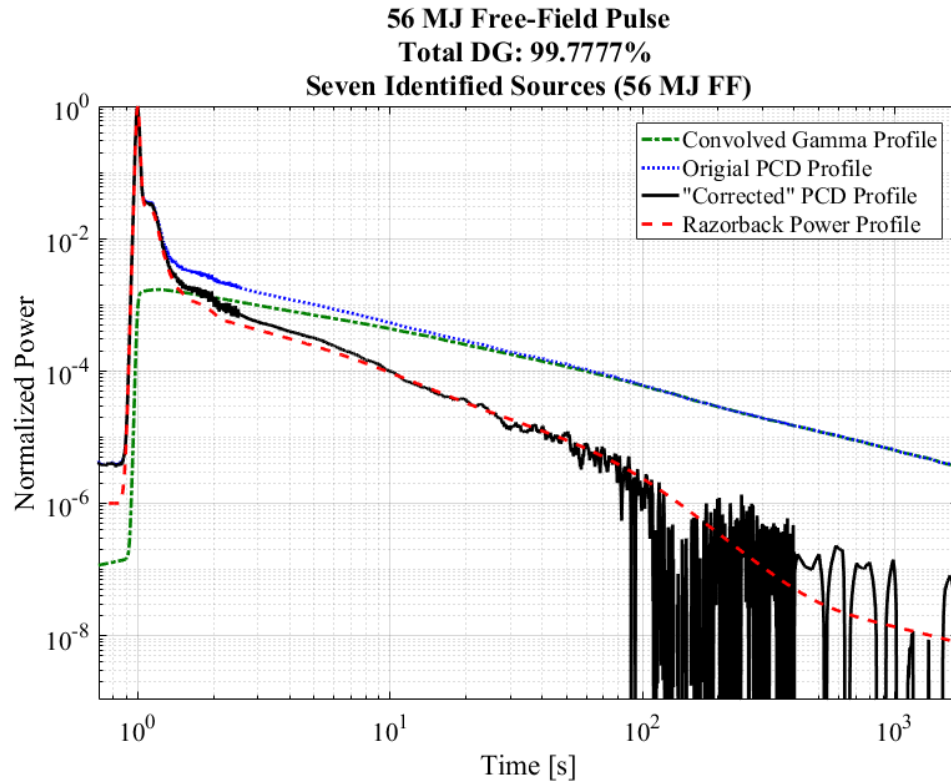


Figure 6.1: The results of correcting the 56 MJ FF PCD signal using the seven identified sources, and the reactivity calculated using the inverse kinetics code.



### **6.1.2 140 MJ Free-Field Pulse**

For this free-field pulse only five sources were identified. In this case, the convoluted gamma profile was found to slightly overlap the original PCD signal, which cause the corrected signal to be negative at late times. For this reason, the corrected profile was only useful for about the first 40 s. This effect could have probably been reduced if a smaller delayed gamma percentage was assumed; however, this would have most likely resulted in poorer agreement with Razorback during earlier times. It can be seen that obtaining the corrected power profiles is very sensitive to noise in the PCD signal, and to how well the identified sources describe the unwanted sources. Figure 6.2 shows a comparison of the power profiles and the reactivity profiles for this pulse. The expected shutdown reactivity immediately following the pulse, for the 140 MJ pulse, is about  $-\$10$  as opposed to about  $-\$9$  for the 56 MJ pulse. This is due to the reactor being hotter in the 140 MJ pulse than in the 56 MJ pulse; however, in both cases, as the reactor cools they both approach about  $-\$8$ .

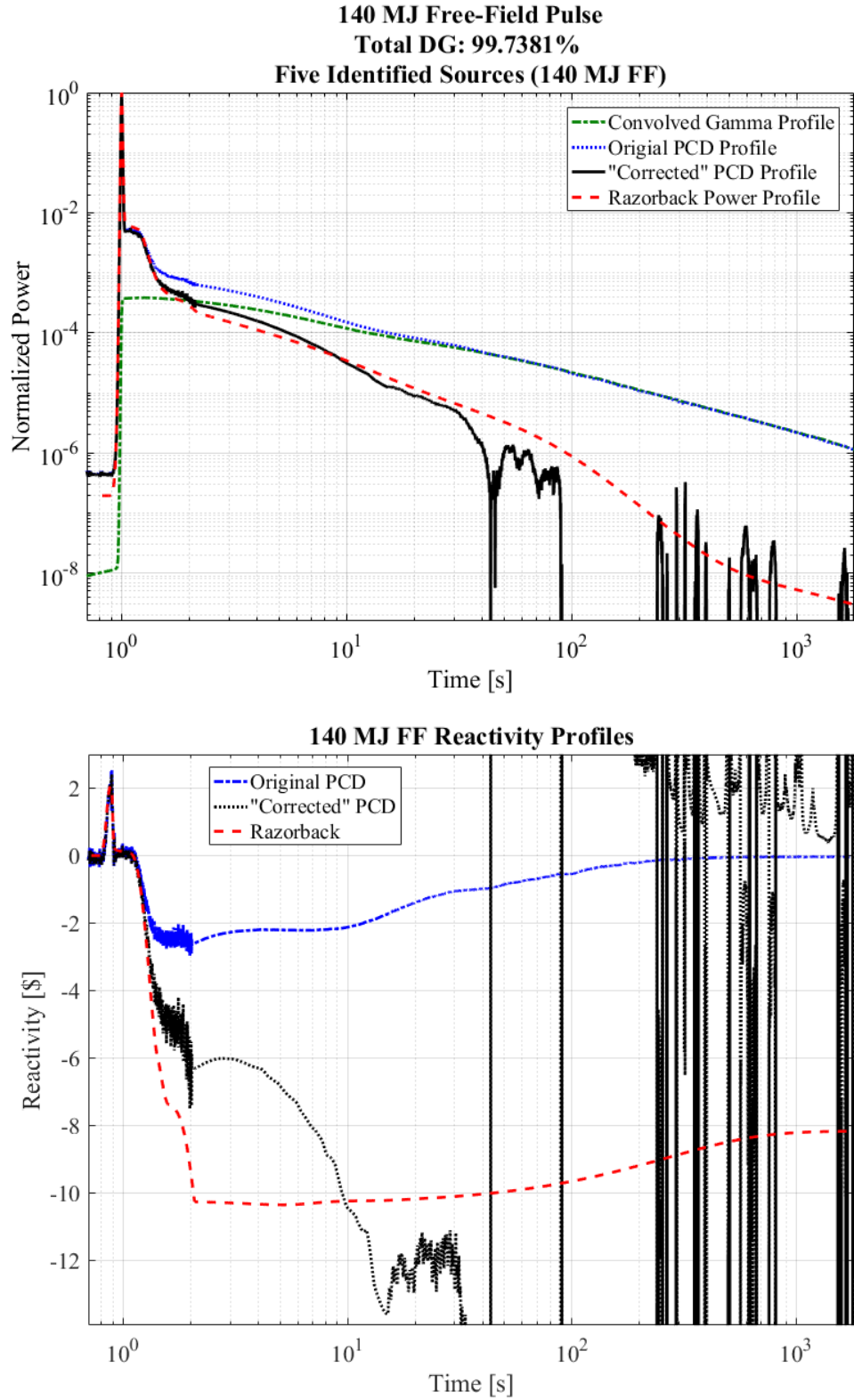


Figure 6.2: The results of correcting the 140 MJ FF PCD signal using the five identified sources, and the reactivity calculated using the inverse kinetics code.

### 6.1.3 127 MJ Lead-Boron Pulse

The expected reactivity profiles for pulses with the LB44 bucket differ slightly from the FF pulses. This is because the LB44 bucket has a reactivity worth of about  $-\$6$  [Parma et al., 2013]. This results in the shutdown reactivity being about  $\$6$  lower than the same sized FF pulse. Figure 6.3 shows the results for a 127 MJ LB44 pulse, for which six sources were identified. It was unclear how the LB44 bucket would affect the PCD response, since it reduces the gamma and thermal neutron dose in the central cavity. It was found that the delayed gamma fraction at 1800 s was about 0.1% greater for the LB44 pulses than the FF pulses. This suggests that PCD's signal following the pulse is no more proportional to the true reactor power than a FF pulse, if anything, it is slightly worse. The convoluted gamma profile for this pulse slightly overlapped the PCD signal and was within its noise during late times, resulting in about 70 s worth of useful corrected data. As expected, the correct reactivity was calculated before and during the pulse; however, it did not go as negative as expected following the pulse, but on average, it was clearly more negative than the FF pulses.

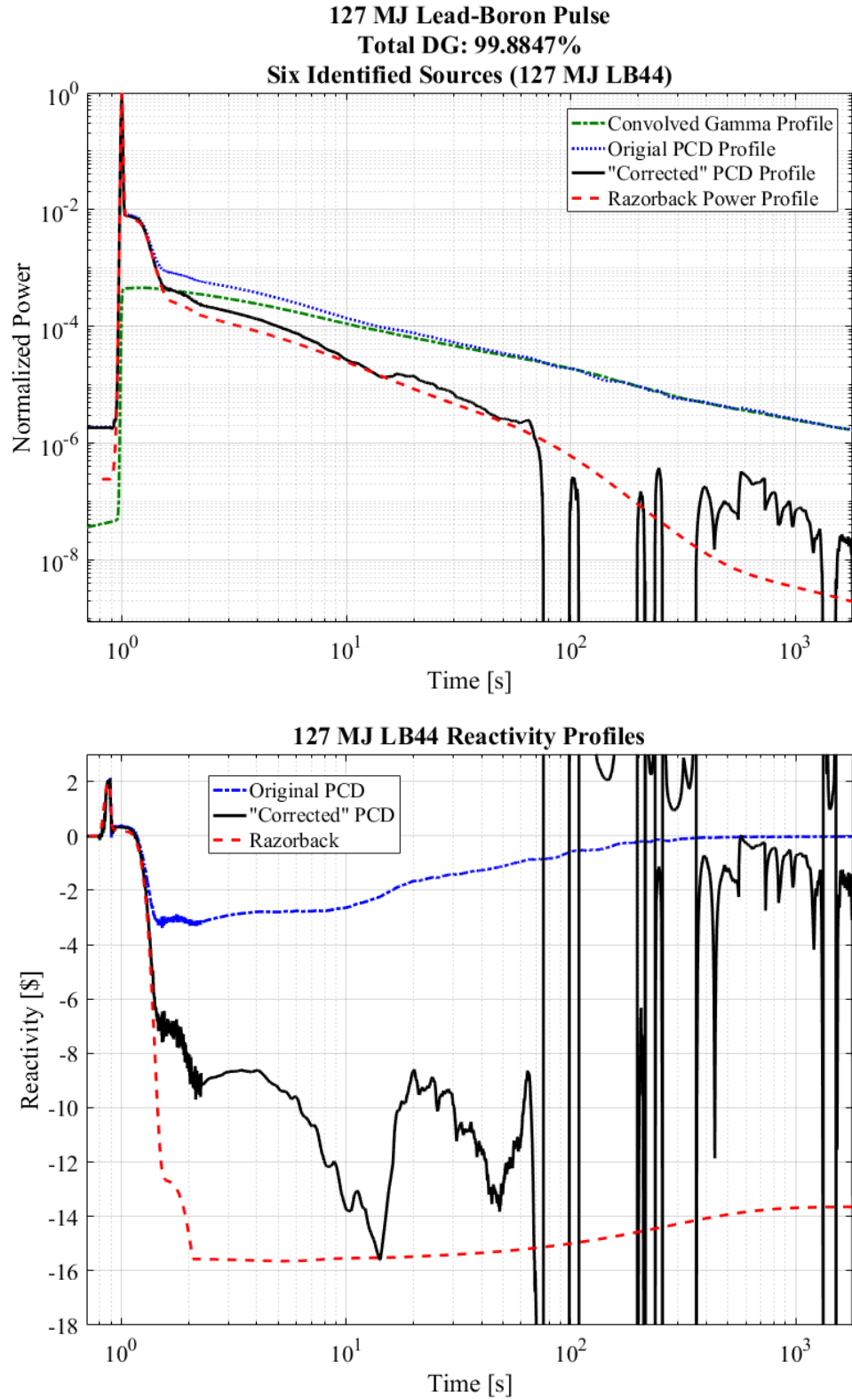


Figure 6.3: The results of correcting the 127 MJ LB44 PCD signal using the six identified sources, and the reactivity calculated using the inverse kinetics code.

#### **6.1.4 270 MJ Lead-Boron Pulse**

For the 270 MJ LB44 pulse, seven sources were identified. As can be seen in Figure 6.4, the “corrected” power profile stays consistently above the Razorback power profile and has less noise at late times than has been seen with the previous three pulses. This is because the convoluted gamma profile in this case isn’t as close to the original PCD profile as in the previous cases. This could be because the delayed gamma fraction at 1800 s is greater than the calculated value of 99.8631%, or it could be due to errors in the half-lives and relative abundances of the identified sources. Because of the overestimation of the power during the tail of the pulse, the corrected reactivity doesn’t drop nearly as negative as expected and it begins to approach \$0 at late times.

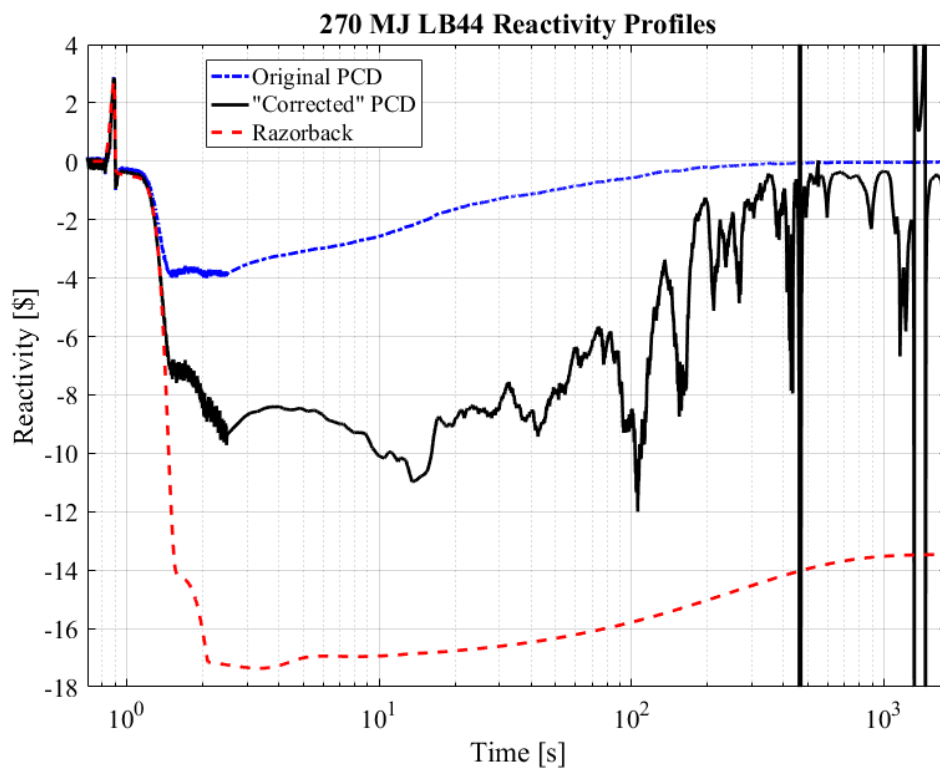
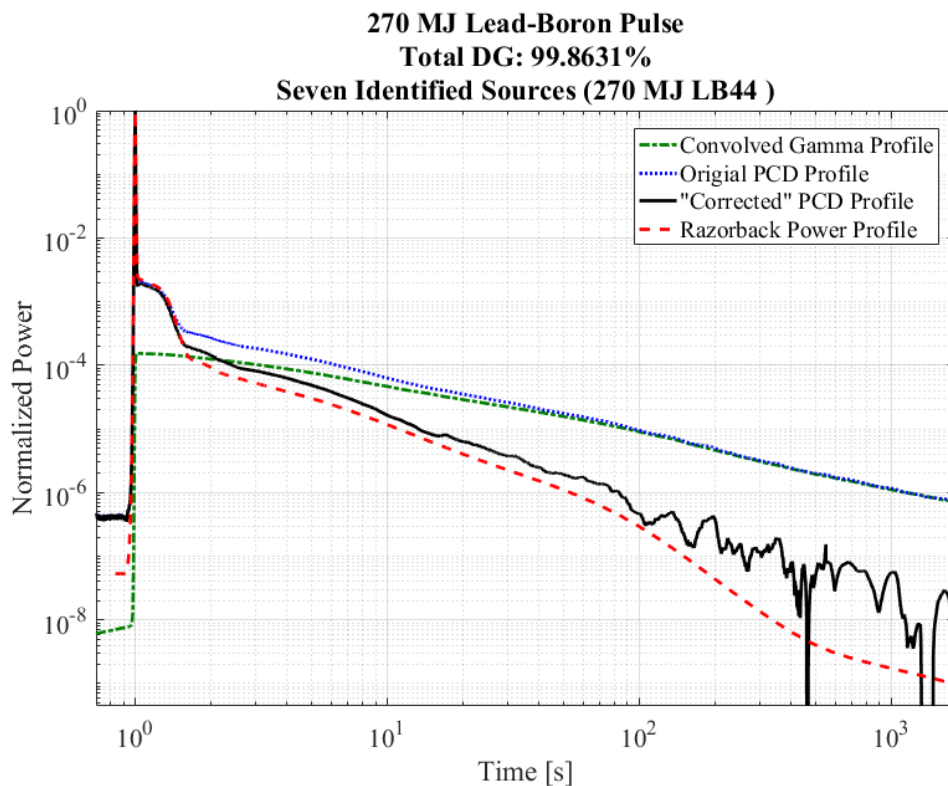


Figure 6.4: The results of correcting the 270 MJ LB44 PCD signal using the seven identified sources, and the reactivity calculated using the inverse kinetics code.

### **6.1.5 Comparison of Identified Half-Lives**

The half-lives and relative abundances of the identified sources are listed in Table 6.1. Similarities in the half-lives are observed between the two FF pulses and between the two LB44 pulses; however, not much similarity is seen between the FF and LB44 half-lives. This implies that following the pulse, the gamma sources that dominate in the FF environment are different than those dominate in the LB44 environment. In the LB44 environment, we would expect that fission product gammas play a smaller role than in the FF environment, since the lead shields the PCD from some of the gammas coming from the fuel. Future work could involve trying to identify the isotopes responsible for the different sources.

The similarities observed in the half-lives for FF and the LB44 bucket, suggest that it might be possible to determine a general decay curve for each environment. If these decay curves were known they could be used to correct the PCD signals, assuming the delayed gamma fraction is known at a time. However, more data would need to be analyzed to see if the same half-lives are consistently observed. Being able to obtain a profile proportional to the reactor power would not only allow the reactivity profile to be calculated, but it would also allow the time dependent neutron dose seen by an experiment to be determined.

As seen in this chapter, the portion of the PCD signal proportional to the reactor power during the tail of the pulse is small. For this reason, it was difficult to resolve the true power profile beyond about 100 s. In addition, correcting the power profiles using the method described, was found to be sensitive to how well the data was smoothed and how well the unwanted sources were identified. Despite this, by attempting to subtract the gamma sources that weren't proportional to the reactor power, the accuracy of the calculated reactivity profiles was greatly improved.

Table 6.1: The identified sources responsible for the excess contribution to the PCD signal during the tail of the pulse. The same number of sources were not identified for each pulse, which needs to be considered when comparing relative abundances.

FF 56 MJ	Half-Life [s]	1078	173.7	42.2	13.8	4.16	0.967	0.513
	Relative Abundance	0.005	0.0138	0.0618	0.0944	0.2957	0.3521	0.1772
FF 140 MJ	Half-Life [s]	905.3	150.0	43.4	13.9	2.37	NA	NA
	Relative Abundance	0.0098	0.0314	0.0854	0.1343	0.7391	NA	NA
LB44 127 MJ	Half-Life [s]	2014	222.8	51.8	NA	7.87	1.97	0.517
	Relative Abundance	0.0054	0.0125	0.0724	NA	0.1978	0.5863	0.1256
LB44 270 MJ	Half-Life [s]	1776	218.6	57.1	20.8	6.75	2.17	0.391
	Relative Abundance	0.0074	0.0197	0.0778	0.0784	0.1725	0.5104	0.1338



## 7. Conclusion

The purpose of this project was to use the inverse kinetics method and experimentally gathered data to calculate the reactivity profile of the ACRR during and following pulses. To measure the reactor's power profile, a diamond photoconductive detector was used, which was the best diagnostic currently available at the ACRR for this application. The PCD provided a fast response that could capture the details of the pulse, and when used with a logarithmic amplifier, its signal could capture the large changes in signal strength experienced between the peak of the pulse and the tail of the pulse. However, as has been shown, the PCD begins to lose its proportionality to the true reactor power, very soon after the knee of the pulse. This behavior was attributed to the detection of delayed fission product and activation gamma rays, which dominated the relatively small contribution from delayed neutrons.

To obtain a profile that better represented the true power of the reactor, attempts were made to subtract the delayed gammas from the PCD signal. Within the scope of this project, the most promising way of doing this utilized Razorback simulations of the pulses. By comparing to the Razorback power profiles, the sources responsible for the unwanted contribution to the PCD profile could be identified. These sources were then iteratively convoluted with the PCD signal and subtracted, ideally leaving behind the portion of the signal proportional to the reactor power. The corrected PCD profiles showed better agreement with Razorback; however, the profiles became very noisy beyond about 100 s. This suggested that the delayed neutron contribution would be hard to resolve beyond this point, but with more exact smoothing and source identification it might be possible to resolve it beyond 100 s. The sources identified from this method were found to have similarities depending on whether they came from a FF or LB44 pulse, regardless of the pulse size. This suggest that it might be

possible to create a general decay curve for FF and LB44 pulses that could be used to correct the profiles without needing to identify the sources each time, but this requires further investigation. Of the sources identified, none of them could definitively be attributed to a specific fission product or activation isotope, but with further investigation it might be possible to identify the isotopes.

To perform the reactivity calculations, a computer code was written that numerically solved the inverse kinetics equation. A constant power analytical initial condition was derived and implemented in the inverse kinetics code. The code utilized both the standard eight-group U-235 precursors and the nine beryllium photoneutron precursors; however, over the time range that could be resolved with the “corrected” PCD profile, the U-235 precursors dominate. The functionality of the code was validated using Razorback. In addition, a point kinetics code was written to assist in exploring the behavior of the inverse kinetics code. Many other codes were also written to prepare the experimental data, and to identify and subtract the unwanted sources.

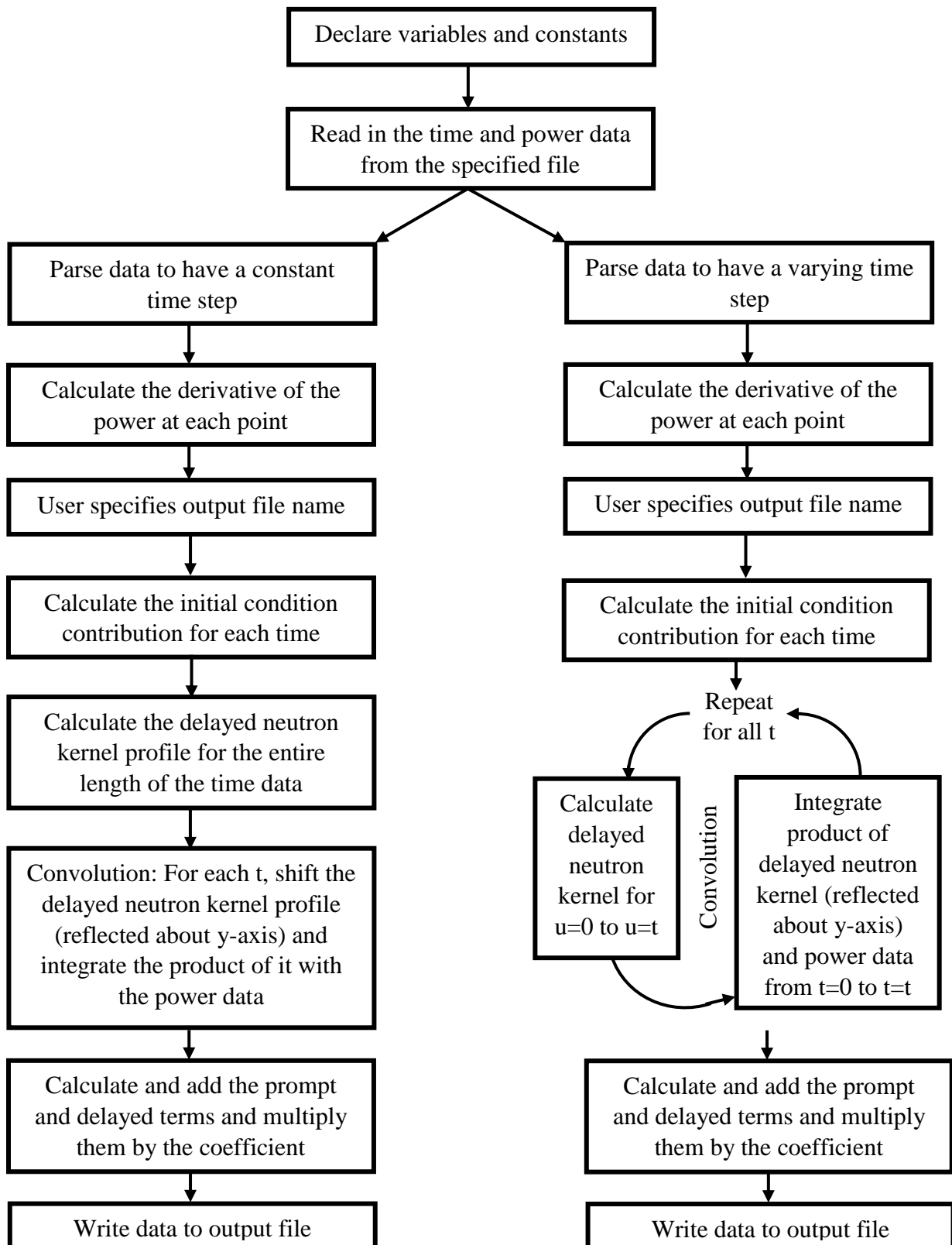
Even though the correct reactivity was not able to be exactly calculated following the pulse, it was accurately calculated during the constant power region before the pulse and during the pulse. This project made it very apparent that the PCD does not accurately capture the power profile, and hence the neutron population, following the pulse.

## **7.1 Future Work**

The primary focus of future work related to this project, would be to explore alternative detector options that could better capture the neutron population behavior during the tail of the pulse. One idea is to operate a fission chamber in a pulse counting mode during the tail of the

pulse, and discriminate the gamma contribution. A  $\text{BF}_3$  or other similar neutron detectors could also be investigated for this application. Rod drop experiments using detectors in a pulse counting mode could be performed to measure the cold shutdown reactivity of the reactor. Modeling could also be done using MCNP to better characterize the radiation response of the PCD, so that better attempts can be made to subtract the gamma contribution. If the late time power of the ACRR is able to accurately be captured, the applicability of the nine beryllium photoneutron groups could be studied.

## Appendix A – Inverse Kinetics Code Flow Chart for Fortran 95



## References

- Bernstein, S., Ergen, W., Talbott, F., Leslie, J., & Stanford, C. (1956). "Yield of Photoneutrons from U-235 Fission Products in Beryllium and Deuterium." *Journal of Applied Physics*, 27(18).
- Campbell, J. M., Spriggs, G. D., & Vladimir, P. M. (2002). "An 8-Group Delayed Neutron Model Based On a Constant Set of Half-Lives." *Progress in Nuclear Energy*, 41(1), 223-251. Retrieved from <http://www.sciencedirect.com/science/article/pii/S0149197002000136>
- Griffin, P. J., Luker, S. M., King, D. B., DePriest, K. R., Hohlfelder, R. J., & Suo-Anittila, A. J. (2004, December). "Diamond PCD for Reactor Active Dosimetry Applications." *IEEE Transactions on Nuclear Science*, 51(6), 3631-3637.
- Hetrick, D. L. (1971). *Dynamics of Nuclear Reactors*. Chicago: The University of Chicago Press.
- Hoogenboom, J. E.; Van Der Sluijs, A. R. (1988). "Neutron Source Strength Determination for On-Line Reactivity Measurements." *Ann. Nucl. Energy*, 15(12), 553-559.
- Keepin, G. R., Wimett, T. F., & Zeigler, R. K. (1957, August 15). "Delayed Neutrons from Fissionable Isotopes of Uranium, Plutonium, and Thorium." *Physical Review*, 107(4), 1044-1049.
- Keepin, G. R. (1965). *Physics of Nuclear Kinetics*. Reading Massachusetts: Addison-Wesley Publishing Company, Inc.
- Knief, R. A. (2015). *Technical Area V - Unique Facilities*. Albuquerque: Sandia National Laboratories SAND2015-20764 PE.
- Knoll, G. F. (2010). *Radiation Detection and Measurement* (4th ed.). Hoboken: John Wiley & Sons, Inc.
- Lane, T. K., & Parma, R. J. (2015). *Delayed Fission Gamma-ray Characteristics of Th-232, U-233, U-235, U-238, and Pu-239*. Albuquerque: Sandia National Laboratories Sand 2015-7024.
- Mobley, R. C., & Laubenstein, R. A. (1950, Nov.). "Photo-Neutron Thresholds of Beryllium and Deuterium." *Phys. Rev.*, 80(3), 309-314.
- National Nuclear Data Center. Brookhaven National Laboratory. Retrieved October 2017, from <https://www.nndc.bnl.gov/chart/>
- Parma, E. J., Quirk, T. J., Lippert, L. L., Griffin, P. J., Naranjo, G. E., & Luker, S. M. (2013). *Radiation Characterization Summary: ACRR 44-Inch Lead-Boron Bucket Located in the Central Cavity on the 32-Inch Pedestal at the Core Centerline (ACRR-LB44-CC-32-cl)*. Albuquerque: Sandia National Laboratories SAND2013-3406.

Parma, E. J., Naranjo, G. E., Vega, R. L., Lippert, L. L., Vehar, D. W., & Griffin, P. J. (2015). *Radiation Characterization Summary: ACRR Central Cavity Free-Field Environment with the 32-Inch Pedestal at the Core Centerline (ACRR-FF-CC-32-cl)*. Albuquerque: Sandia National Laboratories SAND2015-6483.

Pickard, P. S., & Odom, J. P. (1982). *Reactor Physics Design Calculations for the ACPR Upgrade*. Albuquerque: Sandia National Laboratories SAND80-0764.

Talley, D. G. (2017). *RAZORBACK - A Research Reactor Transient Analysis Code, Version 1.0, Volume 3: Verification and Validation Report*. Albuquerque: Sandia National Laboratories SAND2017-3372.